Nanoscale Analysis on the Reaction Mechanism of Reductants for Electroless Deposition Processes using Surface Enhanced Raman Spectroscopy

October, 2013

2013 年 10 月

Bin JIANG

姜　彬

Nanoscale Analysis on the Reaction Mechanism of Reductants for Electroless Deposition Processes using Surface Enhanced Raman Spectroscopy

October 2013

Waseda University
Graduate School of Advanced Science and Engineering
Major in Nanoscience and Nanoengineering
Research on Nano-Functional Surface Chemistry

Bin JIANG

Preface

Electroless deposition process, which takes place with the deposition of metal by electron supplied by oxidation reaction of reductant, is significant for fabricating ultra-thin films and is widely applied for various fields such as microelectronics and nanotechnology. Since the process has advantages such as lower costs with simple processing, uniformity of deposits on complex shapes, independency on the electrical properties of the substrate and easy control of the coating thinness, it is expected as fundamental technology for micro and nano system fabrications.

In order to achieve more precise control of the solid-liquid interface in electroless deposition process to satisfy the strong demand for much advanced devices, it is necessary to clarify the reaction mechanism of electroless deposition process with molecular level resolution. However, the complexity of the reaction mechanism for reductant oxidation and other components such as complexing agent and additives in the process make it difficult to understand their chemistry in details. Such fundamental reaction mechanisms have not been fully elucidated yet. This often prevents researchers from understanding and establishing novel and highly controlled plating processes.

Against this background, Surface Enhanced Raman Scattering (SERS) effect, which is a breakthrough technique that can provide in-situ, ultrasensitive characterization of chemicals on metals down to sub-monolayer level for analysis of solid-liquid interface, has been utilized for many decades. In general, molecular level detection at solid-liquid interface by SERS sensors has been investigated by applying plasmonic metal either with roughened surfaces or nanostructures. An amplification of the Raman signal due to the electromagnetic field depends crucially on the size of the plasmonic metals and the distance from the plasmonic metals in the range of 1-2 nm. Thus, it is difficult to define the place where the detected molecules are existed.

This study attempts to understand the reaction mechanism of the electroless deposition process using experimental and theoretical methodologies focusing on the mechanism of the reductant reactions on metal surfaces. The experimental method is applicable for characterizing reductants adsorption on metal surfaces with high-selectivity component at right angle down to sub-monolayer level using a surface enhanced Raman antenna, which can define the place and structure of adsorbed reductants just only at 1-2 nm from the antenna surface. Meanwhile, the theoretical method Density Functional Theory (DFT) can provide molecular level, basic level information for understanding the mechanism according to the chemical characteristics.

Much insight can be gained from the theoretical calculation, and the mere reproduction of experimental data will never be satisfying unless they come with a great deal of improved understanding.

This thesis is composed of five chapters, as described below.

In chapter 1, general introduction regarding the electroless deposition process such as developments, analyses, and some examples of recent applications is overviewed. Considering some fundamental concepts about the reductants and catalytic activity of metal surfaces is also introduced. Moreover, the motivation for the entire study, the methodologies extremely useful for the analysis of the process and the fundamental strategy of this study are described.

In chapter 2, the measurement of several common reductants on metal plasmon antennas using SERS and DFT is described, which introduces the major premise that the function of the plasmon antenna and the agreement between experimental results and theoretical results are measured for the later chapters.

In chapter 3, the analysis of the interaction between hydrazine and hypophosphite ions on a Cu surface with nano-scale resolution using SERS and DFT is determined, which is very useful for understanding the reaction mechanism of reductants in the electroless deposition.

In chapter 4, the analysis study of acceleration and suppression effect of thiourea on the oxidation reaction of hypophosphite ions on Ni surface using SERS and DFT is described, which is very important for understanding the complicated behaviors of thiourea in the electroless deposition process as an additive.

In chapter 5, the obtain results are comprehensively discussed and the theory established through several analyses of this study is introduced.

Table of Contents

Preface **i**

Chapter 1 – General Introduction

1.1 Electroless deposition process **2**
1.1.1 Outline of the electroless deposition process **2**
1.1.2 Examples of the electroless deposition process **9**
1.1.3 Reductants **18**
1.1.4 Catalytic activity of metal surfaces **24**
1.1.5 Effects of various factors **31**
1.2 Surface enhanced Raman spectroscopy **36**
1.2.1 Outline of surface enhanced Raman spectroscopy **37**
1.2.2 Examples of surface enhanced Raman spectroscopy **40**
1.2.3 Theoretical approaches **46**
1.3 Strategy of this study **50**
References **51**

Chapter 2 –Characterization of reductants at metal surfaces using SERS and DFT

2.1 Introduction **58**
2.2 Methodology **60**
2.3 Results and Discussion **65**
2.3.1 SERS of reductants **65**
2.3.2 SERS of reductants on a Ag surface **68**
2.3.3 SERS and DFT of formaldehyde on a Cu surface **71**
2.4 Conclusions **75**
References **76**

Chapter 3 – Analysis of hydrazine and hypophosphite ions on a Cu surface using SERS and DFT

3.1 Introduction **80**
3.2 Methodology **82**
3.3 Results and Discussion **84**
3.3.1 SERS and DFT of hydrazine and hypophosphite ions **84**
3.3.2 Analysis of hydrazine on a Cu surface with nano-scale resolution by SERS and DFT **87**
3.3.3 Analysis of hypophosphite ions on a Cu surface with nano-scale resolution by SERS and DFT **91**
3.3.4 Analysis of hydrazine and hypophosphite ions on a Cu surface with nano-scale resolution by SERS and DFT **92**
3.4 Conclusions **95**
References **96**

Chapter 4 – Analysis of acceleration and suppression effect of thiourea on the reaction of hypophosphite ions on Ni surface using Raman spectroscopy and DFT

4.1 Introduction **100**
4.2 Methodology **101**
4.3 Results and Discussion **104**
4.3.1 Raman and DFT of thiourea and hypophosphite ions **104**
4.3.2 Analysis of thiourea and hypophosphite ions on a Ni surface with nano-scale resolution by Raman and DFT **106**
4.3.3 Analysis of the pH effect on thiourea and hypophosphite ions on a Ni surface by Raman and DFT **110**
4.4 Conclusions **115**
References **116**

Chapter 5 – General Conclusions **120**

List of Achievements **124**

Acknowledgement **128**

Chapter 1:
General Introduction

1.1 Electroless deposition process

1.1.1 Outline of the electroless deposition process

Electroless deposition process

Electroless deposition is a plating process, in which the oxidation of reductants is applied as electron resources for fabricating functional metal thin films. This process has been recognized as one of the most effective techniques for meeting future demands for more highly controlled metal film fabrication, due to its advantages such as lower costs with simple processing, uniformity of deposits on complex shapes, independency on the electrical properties of the substrate, and easy control of the coating thinness [1].

The term “electroless deposition” was first demonstrated by Brenner and Riddell [2-4], who published a paper that described a process of forming a metal film onto a substrate in aqueous solutions by the reduction of metal ions in the solution by a reductant. In the paper, they added hypophosphite ion as an oxidation inhibitor into Ni-P electrodeposition bath. The hypophosphite ion induced a spontaneous deposition, since it also played the role of a reductant. Brenner et al. called the system an “auto catalytic” deposition; referring to the catalytic activity of the Ni-P surface for hypophosphite ion, where the deposition and oxidation reactions took place continuously.

However, the concept of such electroless deposition system was originally derived from the work by Wurtz [5] in 1844, which only obtained a black powder by observing that nickel cations were reduced by hypophosphite. After this pioneering work, the first bright metallic nickel deposits were obtained in 1911 by Breteau [6]; the first systematic deposition bath for electroless nickel plating was proposed in 1916 by Roux [7]; and the first discovery of the phenomena of nickel deposition by the chemicals was constructed in 1959 by Gutzeit [8], which have become the “pioneers” of the present electroless deposition process. Through the various researches, moreover, the concept of this electroless deposition process has been found to be applied not only to the deposition of nickel but also to the deposition of other several metals. The metals and metal alloys which can be obtained by electroless deposition are shown in Table 1.1.1 [9,10].

Table 1.1.1 Periodic table of the elements, showing depositable metals and alloys without an external electric current shown; circle: autocatalytic deposition, triangle: codeposition with Ni or Co, square: galvanic displacement [9,10].

4A	5A	6A	7A		8		1B	2B	3B	4B	5B
									B	C	N
Ti	V	Cr	Mn	Fe	Co	Ni	Cu	Zn	Ga	Ge	As
Zr	Nb	Mo	Tc	Ru	Rh	Pd	Ag	Cd	In	Sn	Sb
Hf	Ta	W	Re	Os	Ir	Pt	Au	Hg	Tl	Pb	Bi

Overall electroless deposition process can be explained by a combination of anodic oxidation of reductants and cathodic reduction of metal species [11-15]. The schematic illustration of entire process of electroless deposition is shown in Fig. 1.1.1, where M, Re, e^- represent metal atom, reductant, and electron. Figure 1.1.1 displays: (i) The reductants are adsorbed on the substrate; (ii) The OH^- ions can attack the reductants when the reductants are adsorbed on the substrate; (iii) The reductants emit electrons after the OH^- attack; (iv) The metal ions receive electrons emitted toward the substrate through the reductant reactions, which results in the deposition of metal atoms; (v) The atomic metals migrate on the substrate to aggregate, to become bulk metal. In this process, reductant with relatively negative potential supplies electrons as external power supply does in electrodeposition process, as shown in Fig. 1.1.2 [16], where M, Re, e^- represent metal atom, reductant, and electron.

Characteristics of electrodeposition and electroless deposition are summarized in Table 1.1.2. By comparing with electrodeposition, advantages of electroless deposition are exhibited such as flat and homogeneous metal surfaces independent of the current distribution, metal deposition on non conductive substrates, and easy deposition of the functional alloy by adjusting the composition and the condition of the bath.

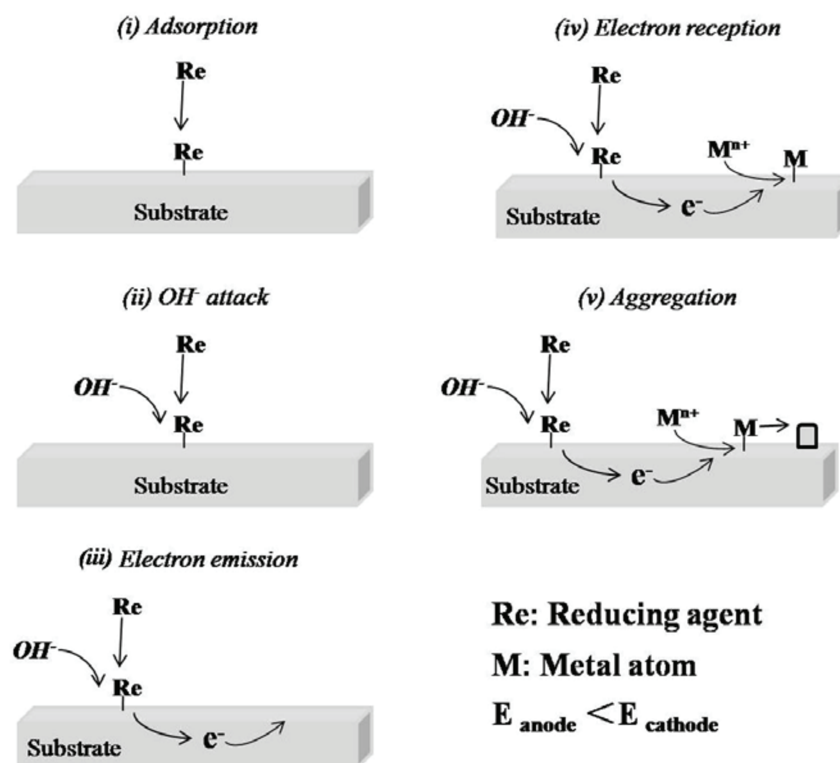

Fig. 1.1.1 Schematic drawing of the electroless deposition process.

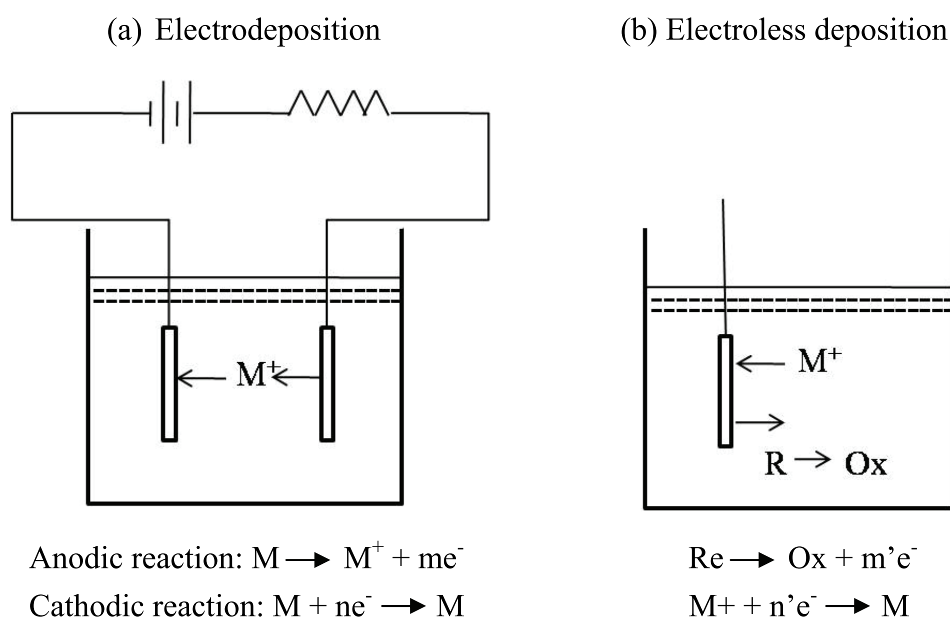

Fig. 1.1.2 Schematic illustration of electrodeposition and electroless deposition [16].

Table 1.1.2 Characteristics of electrodeposition and electroless deposition.

	Electrodeposition	**Electroless deposition**
Driving force	Electrolytic (potential)	Chemical (reductant)
Substrate	Conductor	Conductor and insulator
Deposit	Many elements	Ni, Co, Cu, Pt, Au and their alloys
Characteristics of the deposit	Partially not uniform	Very Uniform
Deposition control	Current	pH, bath temp.
Bath composition	Simple	Complex
Stability of the solution	High	Low
Cost performance	High	Low

The electroless deposition reaction in general have been well explained on the mixed potential theory, first applied by Saito and Paunovic in their works about the analyses of electroless deposition mechanisms [17]. The mixed potential theory is the model claiming that the both anode and cathode reactions must occur at the same potential, called mixed potential, which provides both anodic and cathodic currents suitable for depositions. Furthermore, this theory is quantitatively explained on the basis of the current-potential curves for the overall and partial reactions, as shown in Figure 1.1.3 [18].

Curve 1 in the Fig. 1.1.3 shows the current-potential curve for the overall reaction. The mixed potential E_{pl} is assigned to the potential, where the net current I is zero. Curves 2 and 3 show the partial anodic current I_a for the anodic reactions and the partial cathodic current I_c for the cathodic reactions, respectively. The net current I_n is the result of the superposition of the two partial processes:

$$I_n = I_a + I_c \quad (1)$$

At the mixed potential E_{pl}, I_a is equal to I_c. The electroless deposition current I_{pl}, which corresponds to the deposition rate, is described as:

$$I_{pl} = I_a = I_c \quad (2)$$

The theory introduced here is the simplest model describing the behaviors of the partial anodic and cathodic reaction, which the electroless actual deposition mechanism is actually more complicated than just it. Nevertheless it provides us the suggestive views about the partial anodic and cathodic reactions and the new schematic view to construct some innovative plating systems.

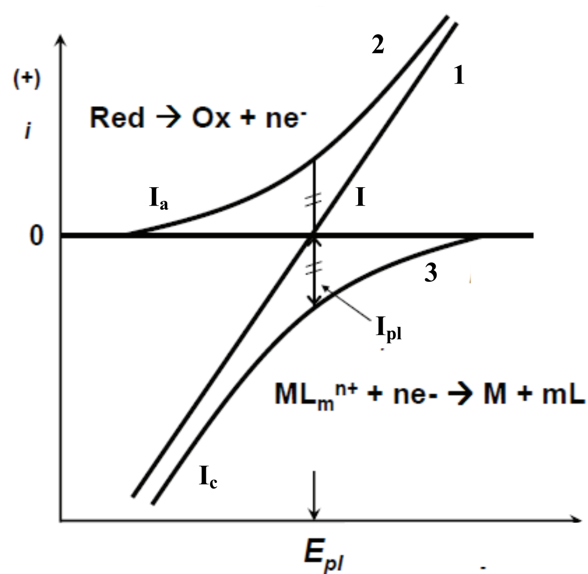

Fig. 1.1.3 Schematic current-potential curves for a mixed potential electrode: curve 1, net current; curve 2, partial anodic current; curve 3, partial cathodic current; Ipl, plating current; Epl, mixed potential [18].

Activation process of electroless deposition

When the metal thin films intend to be deposited on non-catalytic surfaces such as non-catalytic metals, nonconductors, and semiconductor, the surfaces should be activated to induce a partial anodic reaction of reductants. Fig. 1.1.4 shows the potentials where the anodic current originating from oxidation of reductant was a constant value (10^{-4} A cm^{-2}) for various combinations of reductant and substrate metal, which indicates the significance of the catalytic activities of metal surfaces on the anodic oxidation of the reductants [19]. As shown in this figure, the activation of oxidation reaction of each reductant depends on the kind of metal surface. Therefore, the generation of proper metal nuclei on the non-catalytic surface will be useful way to activate the surface for electroless deposition process.

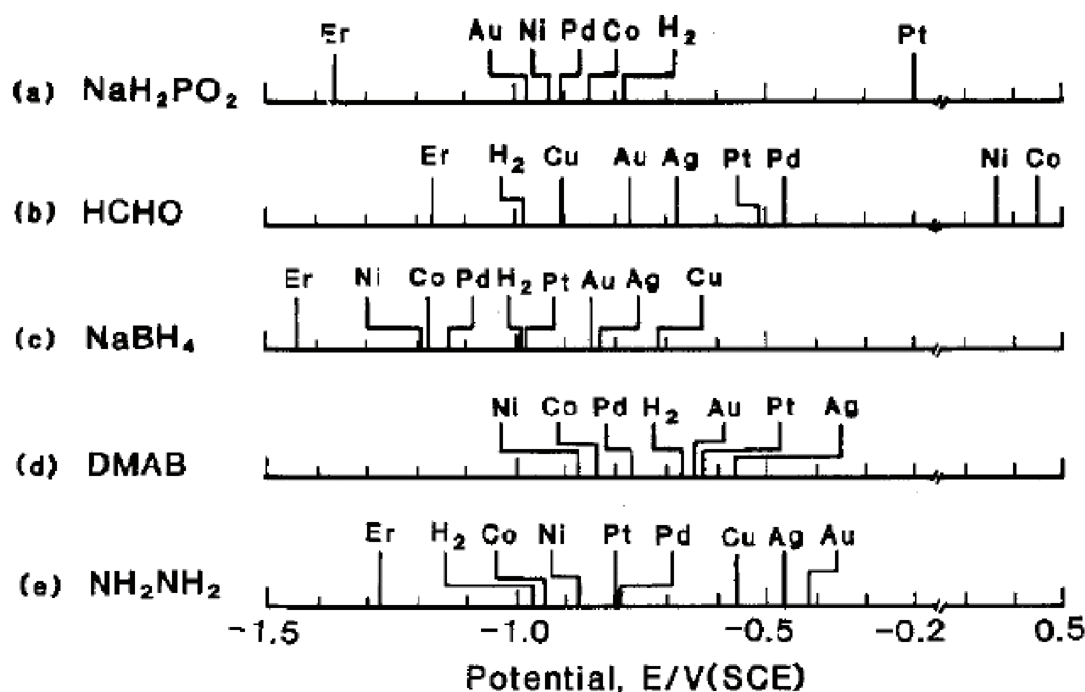

Fig. 1.1.4 Catalytic activities of metals (the potentials at 10^{-4} A cm^{-2}), for anodic oxidation of different reductant; E_r: oxidation-reduction potentials of reductants; H_2: reversible hydrogen potentials [19].

1.1.2 Examples of the electroless deposition process

Electroless deposition process is applicable for fabricating magnetic thin films and is widely applied for various metal plates such as Ni, Cu, and Pd. Typical processes, typical application examples, and a recent topic about those depositions are shown below.

Electroless deposition of magnetic thin film

Magnetic thin films with high magnetic coercivities are required for various advanced applications such as nano-electromechanical systems, magnetic recording devices, and sensing devices [20-24]. Since 1950's, electroless deposition method attracted attention as fabrication process to obtain metallic magnetic thin film, because it has advantages like area selective formation of microstructures or nanostructures with various patterns, uniformity of the film, and mass productivity. Figure 1.1.5 simply shows the history preparation methods of magnetic recording media [25].

By controlling the bath conditions and removing the impurity in the plating bath, the CoNiP longitudinal magnetic recording layer for hard disk device prepared with electroless deposition was practically used [26,27]. In a lot studies on CoNi-alloy recording media, some factors affecting the microstructure and magnetic properties of the media, and our previous works concerning electroless deposition used for developing magnetic recording media are introduced briefly in this section.

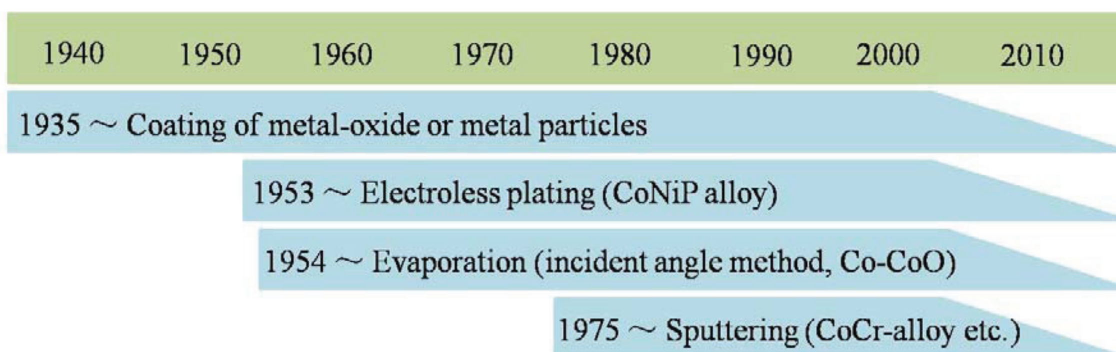

Fig. 1.1.5 History of development of magnetic film for recording media [25].

Effect of impurity in plating bath and pH on microstructure of CoNiP perpendicular recording media

The microstructure and magnetic properties of CoNiP longitudinal media was mainly affected by impurity and pH in the electroless deposition bath. Figure 1.1.6 shows dependence of the coercivity of CoNiP longitudinal media on some metal ion impurities and their concentration in plating bath [28]. In this figure, the coercivity was discovered to be easily varied by impurity with concentration as low as 100 ppm, which caused the fluctuation of media characteristics among the media. Thus, the reproducibility of the characteristics could be improved by removing the impurities carefully from the plating bath.

On the other hand, it was also reported that the CoNiP perpendicular recording media using single-complextant bath operated at room temperature was developed by Homma *et al.* [29-31]. In their studys, the perpendicular coercivity deposited CoNiP film depended on pH of the solution, where pH was adjusted by NH_4OH, as shown in Fig. 1.1.7. In the figure, the dashed line indicated the dependence of Hc value of CoNiP film deposited on substrate without pretreatment on the pH of plating bath. Meanwhile, Fig. 1.1.8 shows the schematic model of the film growth process for the CoNiP specimens treated with the solution with pH=8.0 (solution B) and with pH=9.0 (solution C). This structural analysis suggested that the ammonia prevented the grain growth of CoNiP as pH adjuster adsorbed to the substrate surface. The change in grain growth resulted in the difference in perpendicular coercivity [31].

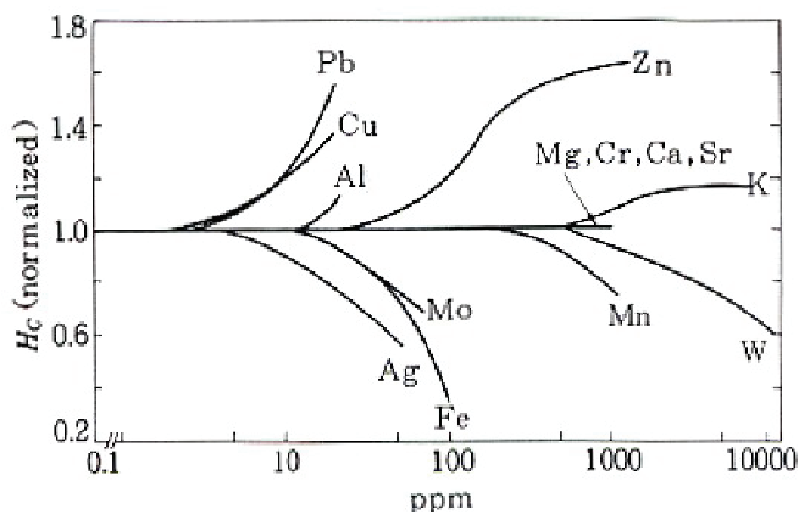

Fig. 1.1.6 Effect of metal impurities in plating bath on coercivity of CoNiP longitudinal media [28].

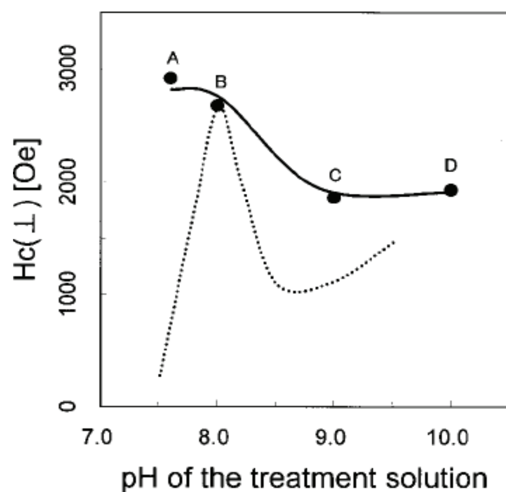

Fig. 1.1.7 The change in Hc (⊥) in accordance with the change in the pH of the treatment solution [31].

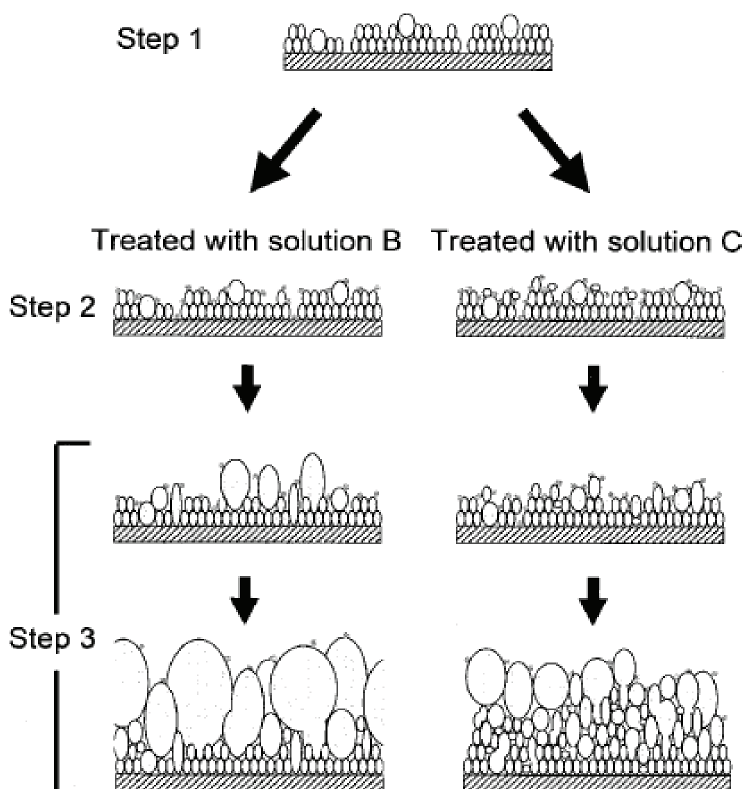

Fig. 1.1.8 Schematic model of the film growth process for the CoNiP specimens; solution B, pH 8.0; solution C, pH 9.0 [31].

<u>Our previous works concerning electroless deposition used for developing magnetic recording media</u>

Electroless deposition process for fabricating thin films with high perpendicular magnetic coercivities has been investigated in our previous studies. For example, Homma *et al.* reported that the electroless deposited CoNiP films had high perpendicular magnetic coercivity when a bath with sodium hypophosphite and low metal ion concentrations was used [32-36]. The perpendicular coercivity of 2600 Oe with a 200 nm thick film was obtained by controlling the bath composition and deposition conditions, such as rotation speed. In these films, co-deposition of phosphorus made phase separation which induced magnetic isolation between magnetic domains. Based on this electroless deposition process, Kawaji *et al.* fabricated CoNiP nanodot arrays on SiO_2/Si substrate, in which the catalytic activities of the substrate were controlled by a Pd activation process. However, the perpendicular magnetic coercivities of the CoNiP nanodot arrays were less than 800 Oe [37].

In order to achieve CoNiP nanodot arrays with high magnetic properties, T. Ouchi *et al.* applied an fcc-Cu (111) underlayer with low lattice mismatch (2.3%) compared to that of hcp-Co (0002) because the deposits should have high crystallinity during the initial deposition stage [38]. The problem with the application of the Cu underlayer in electroless deposition of CoNiP was that $H_2PO_2^-$, which was used as a reductant in the general electroless deposition of CoNiP, was not oxidized to work as a reductant on the Cu surface. Therefore, in their study, CoNiP nanodot arrays with high magnetic properties (higher than 3000 Oe) of the film even with 25 nm thickness, as shown in Figure 1.1.9, were fabricated using an autocatalytic system with dual reductants, $H_2PO_2^-$ and N_2H_4. The mechanism responsible for the enhancement of perpendicular magnetic coercivities has not been clearly established, however. Thus, author is highly motivated in this study to demonstrate the mechanism.

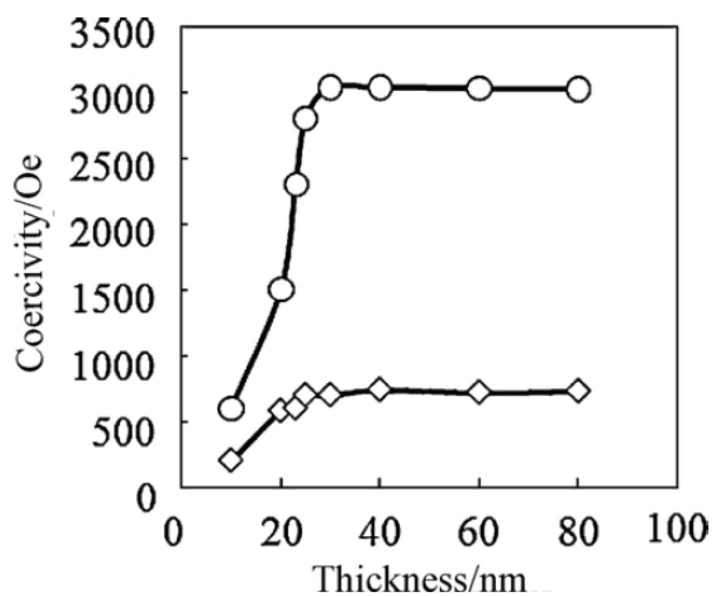

Fig. 1.1.9 Coercivities of CoNiP films with various thicknesses: perpendicular direction (circle plots) and in-plane direction (square plots) [38].

Electroless Ni deposition

Electroless Ni deposition is undoubtedly the most important catalytic plating process applied in various industrial fields, such as electronics devices and vehicles. The history of electroless plating has been accompanying the progress of the electroless Ni plating technique since it was firstly developed in 1946.

The principal reasons for its widespread commercial and industrial use are to be found in the unique chemical and physical properties of the composition of the electroless Ni deposition. In the electroless Ni deposition process, the chemicals which are typically used in the bath are shown in the Table 1.1.3 [39]. Four reductants are mainly used in the chemical reduction of Ni from aqueous solution, and they are summarized in Table 1.1.4. These four reductants are structurally similar in that each contains two or more reactive hydrogens, and Ni reduction is said to result from the catalytic dehydrogenation of the reductant.

Moreover, the main reactions of electroless Ni deposition can be viewed in a very elementary manner as shown below:

Oxidation of reductant

$$\mathrm{Red} \longrightarrow \mathrm{Ox} + ne \quad (3)$$

Reduction of Ni ion

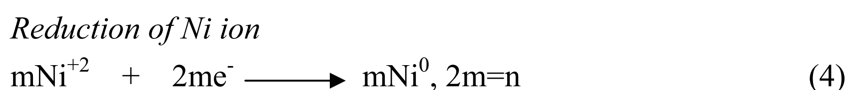

$$m\mathrm{Ni}^{+2} + 2me^{-} \longrightarrow m\mathrm{Ni}^{0},\ 2m=n \quad (4)$$

Overall or sum reaction

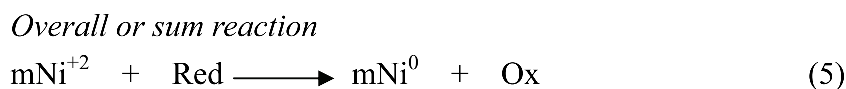

$$m\mathrm{Ni}^{+2} + \mathrm{Red} \longrightarrow m\mathrm{Ni}^{0} + \mathrm{Ox} \quad (5)$$

A chemical oxidation reaction that liberates electrons and a nickel reduction that consumes electrons are shown in equation (3) and (4). Although the sum equation (5) do not account for all of the phenomena that are observed during plating, which because the experimentally observed reaction characteristics are more complex than described by simple stoichiometric equations, is usually written to describe the chemical reduction of nickel by a reductant. In order to ascertain the mechanism of the electroless Ni deposition, hence, it is necessary to understand the reaction mechanisms by various reductants from both theoretical and practical viewpoints.

Table 1.1.3 The chemicals which are typically used in the electroless Ni deposition bath [39].

Reductants	Complexing agents	Buffering agent	Additives
Sodium hypophosphite Hydrazine Sodium borohydride Dimethylamine brane	Latic acid Citric acid Succinic acid Pyrophoric acid Tartaric acid	Sodium acetate	Thiourea Pd

Table 1.1.4 Four reductants which are mainly used in the electroless Ni deposition.

Reductants		Mol.wt.	Equiv.wt	pH range	E,volts
Sodium hypophosphite	$Na^+ [H_2PO_2]^-$	106	53	4-6 7-10	0.499 1.57
Hydrazine	$H_2N{-}NH_2$	32	8.0	12-14	1.16
Sodium borohydride	$Na^+ [BH_4]^-$	38	4.75	6-10	1.24
Dimethylamine brane	$(CH_3)_2NH{-}BH_3$	59	9.8	8-11	–

Electroless Cu deposition

Electroless Cu deposition process is mainly used for plating the printed-circuit board. Such electroless plating of Cu was first discovered by Narcus in 1947 [40]. The first commercial applicability of electroless Cu, with the development of plating solutions for plated-through-hole (PTH) printed wiring boards, was reported in the mid-1950s [41]. In 1957, the first practical bath resembling today's technology was built by Cahill [42]. In Cahill's report, alkaline copper tartrate baths applied formaldehyde as reductant. Although the stability and deposition speed of the Cu baths in 1950s were difficult to control, it accelerated the development of the plating process and industrial applications. Over the years, continual advances in control and capabilities have taken place and continue to be recorded in a variety of research reports [43-50]. At present, over long periods electroless Cu deposition is not only are formulations extremely stable and predictable in behavior, but it also provides excellent physical and metallurgical properties comparable with those of electrolytic deposits.

According to the mixed-potential theory, the overall reaction for electroless Cu deposition, with formaldehyde as the reductant, is shown as equation (6). And it can be decomposed into a simple reduction, the cathodic partial reaction and one oxidation reaction, the anodic partial reaction, as shown as equation (7) and (8) separately.

Overall reaction

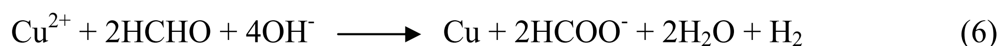

$$Cu^{2+} + 2HCHO + 4OH^- \longrightarrow Cu + 2HCOO^- + 2H_2O + H_2 \quad (6)$$

Cathodic partial reaction

$$Cu^{2+}_{solution} + 2e \xrightarrow{\text{Catalytic surface}} Cu_{lattice} \quad (7)$$

Anodic partial reaction

$$HCHO + 2OH^- \longrightarrow HCOO^- + H_2O + 1/2H_2O + e \quad (8)$$

Electroless Pd deposition

Much effort has been invested in the development of methods for electroless deposition of platinum and palladium alongside the rapid technological growth in the electronics industry. In particular, it is the communication industry that requires electroless Pd plating, since it has been focused as one of the substitutes for Au because of its high resistance to corrosion, low contact resistance, low cost, and solderability. The electroless Pd plating was recognized by Brenner that electroless deposition of Pd

is possible but also that the progress toward homogeneous deposition of Pd results in a high degree of instability of the deposition bath [51]. Before this, Pd was focused as a promising material and plating technique of Pd was only developed in electrodeposition process. Recently, the past studies of the electroless and electrochemical deposition of platinum group metals and their applications were reviewed by Rao and Trivedi [52].

In the electroless Pd deposition process, the main reaction occurring with an approximately neutral bath is shown below:

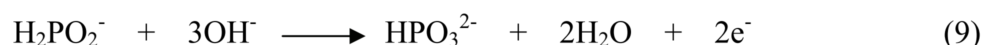

$$H_2PO_2^- + 3OH^- \longrightarrow HPO_3^{2-} + 2H_2O + 2e^- \quad (9)$$

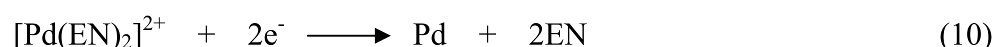

$$[Pd(EN)_2]^{2+} + 2e^- \longrightarrow Pd + 2EN \quad (10)$$

In the equations, hypophosphite ion, ethylenediamine (EN), and thiodiglycolic acid is applied as reductant, complexing agent, and an additive, respectively, for stabilizing the bath.

Electroless Pd deposition process is now applied in various fields of material research, such as superconductivity, optoelectronics, and electrocatalysis. Because it even can be used for catalyzing of some substrates without catalytic activity, such as Cu surfaces for hypophosphite ion. Therefore, the electroless Pd deposition is considered as one of the most necessary techniques for the finer metal deposition of the other metal surfaces as well as for some applications of itself.

1.1.3 Reductants

In the electroless deposition process, the oxidation of reductants is a dominant factor which drives the whole process. Several reductants are commonly used in the electroless deposition process solutions, such as hypophosphite ion, hydrazine, or formaldehyde. However, the complexity of the reaction mechanism for reductants oxidation makes it difficult to improve the efficiency of electroless deposition. In order to understand the fundamental characteristics of reductants, the outlines of each chemical are introduced with brief review of the previous epoch-making experimental and theoretical analysis of them.

Hypophosphite ion

The hypophosphite ion is a well-known reductant for electroless deposition process [53] and electrodeposition of alloys [54]; and it is also a promising hydrogen donor in the catalytic hydrogenation of organic molecules [55]. Hypophosphite ion is the anion ($H_2PO_2^-$), which composes the salt of hypophosphorus acid, such as sodium hypophosphite, calcium hypophosphite, and potassium hypophosphite. The hypophosphite ion consists of one phosphorus atom, as a center atom; two hydrogen atoms attached directly to the phosphorus atom; and two oxygen atoms, which are bond to the center to form a tetrahedral-like structure. It can be made by heating white phosphorus in warm aqueous alkaline solution as shown below:

$$P_4 + 3OH^- + 3H_2O \longrightarrow 3H_2PO_2^- + PH_3 \qquad (11)$$

Although the reaction mechanism of the hypophosphite ion on Ni has been the subject of several studies since the first establishment of the deposition bath [56-60], the sufficient analyses of the hypophosphite reactions from the principal viewpoint had not been reported. In the present study [61], part of reaction pathways of hypophosphite ion is shown in Figure 1.1.10. Figure 1.1.11 shows the reaction energy profiles for the oxidation of hypophosphite ion in the isolated system [62]. The horizontal axis of Fig. 1.1.11 is the reaction steps, which corresponds to the total reaction pathway all intermediates as shown in Fig. 1.1.10. It is indicated that the reaction pathway via five-coordinate intermediate (●) preferentially proceeds than via three-coordinate (○), and the pathway via dianion free intermediate (□) is slightly preferable rather than via five-coordinate intermediate (●).

Five-coordinate intermediate is considered to be a kind of hypervalent molecule,

which can be formed in the case that phosphorous atom can pass its valence electrons easily to near atoms to form the "non-bonding orbitals". Therefore, the theoretical fact that the most stable pathway of hypophosphite ion may be via five-coordinate intermediate, since phosphorous has various oxidation numbers.

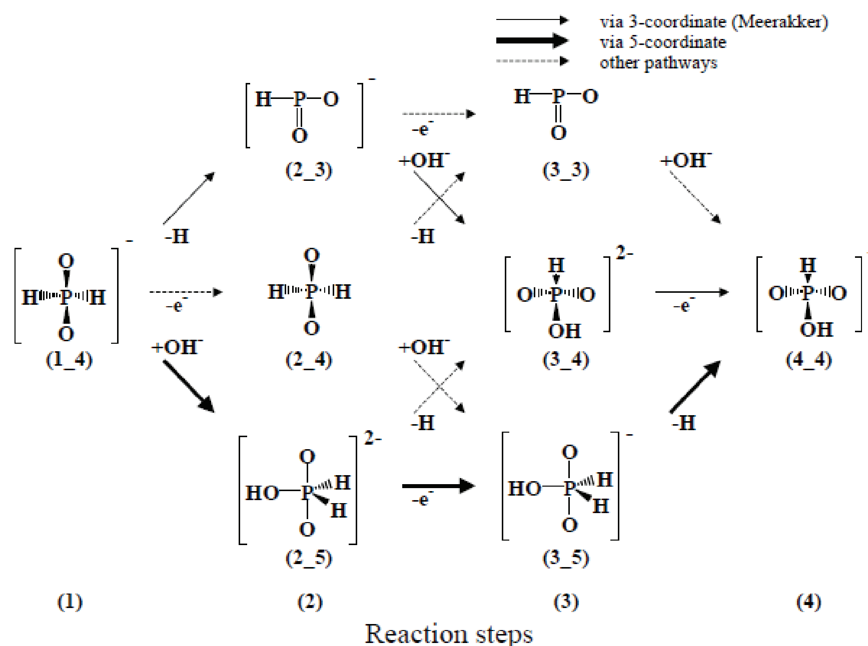

Fig. 1.1.10 Reaction pathways for the oxidation process of hypophosphite ion via all intermediates [61].

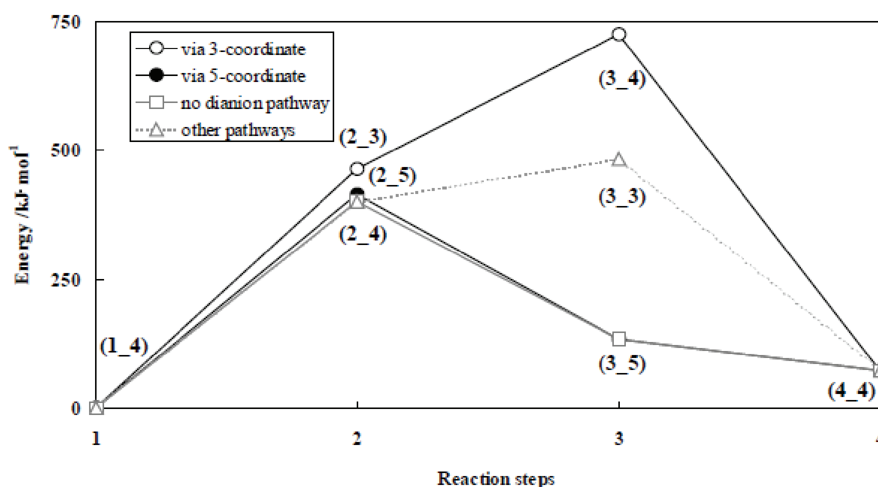

Fig. 1.1.11 Energy diagram for the oxidation reaction of hypophosphite ion via three-coordinate intermediates (○); via five-coordinate intermediates (●); via dianion free intermediates (□); and other pathways [62].

Hydrazine

Hydrazine is a highly reactive base and reductant. As a result of its war-time applications, hydrazine is now applied in various industrial applications and chemical reactions such as nickel plating, photographic development, and so on. The molecular structure of hydrazine is NH_2-NH_2, which has 1.47 Å N-N and 1.04 Å N-H bonds.

The first compound relating to hydrazine was produced in 1887, which became a trigger to seed the method to synthesize pure hydrazine. After that, T. Curtius [63] synthesized free hydrazine for the first time in 1889. In 1907, the pure hydrazine was synthesized by Rasching's remarkable method which relies on the reaction of chloramines with ammonia. In the method, hydrazine was produced in the Olin Rasching process from chloramines; and the reaction mechanism is simply shown as below [64]:

$$NH_2Cl + NH_3 \longrightarrow NH_2\text{-}NH_2 + HCl \qquad (12)$$

Although hydrazine was produced over 100 years ago, the reaction mechanism of hydrazine has not been sufficiently clarified. Much effort has been devoted for improving on our understanding of the reaction mechanism by researchers. Among them, the oxidation pathway of hydrazine as shown in Figure 1.1.12, proposed by van den Meerakker [65], has been verified by the energy file as shown in Figure 1.1.13. Moreover, another alternative oxidation pathway of hydrazine as shown in Figure 1.1.14, proposed by Harrison [66], has also been estimated by the energy file as shown in Figure 1.1.15. The horizontal axes are the reaction steps, which corresponds to the reaction pathways.

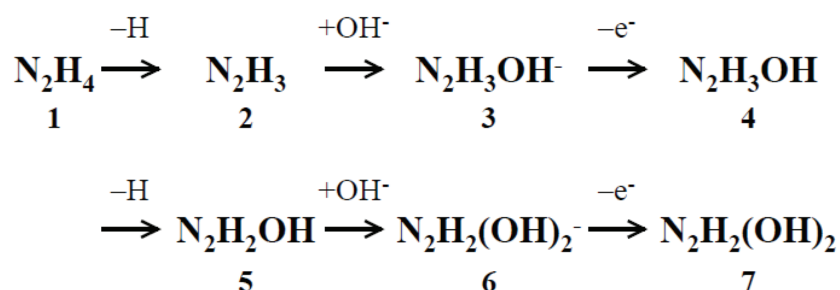

Fig. 1.1.12 The oxidation reaction scheme of hydrazine (Meerakker's proposal pathway) [65].

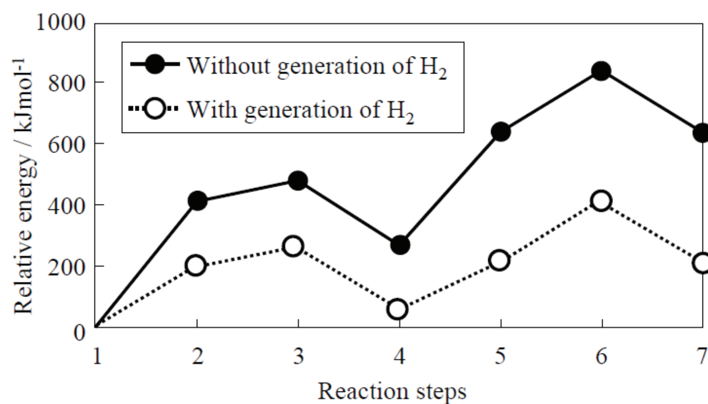

Fig. 1.1.13 Energy diagram for the oxidation reaction process of hydrazine proposed by Meerakker [65].

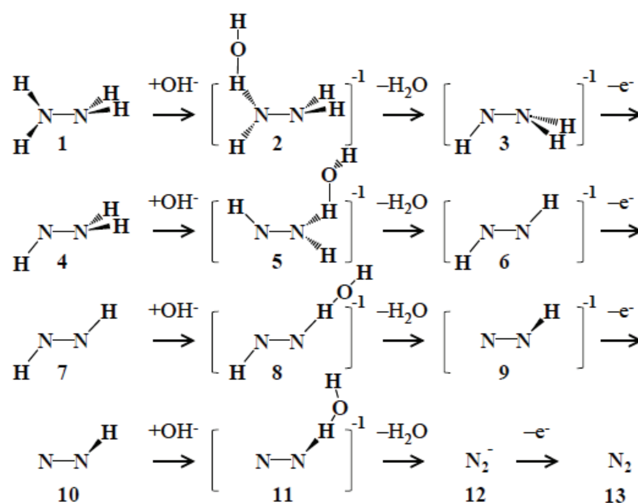

Fig. 1.1.14 The oxidation reaction scheme of hydrazine (Harrison's proposal pathway) [66].

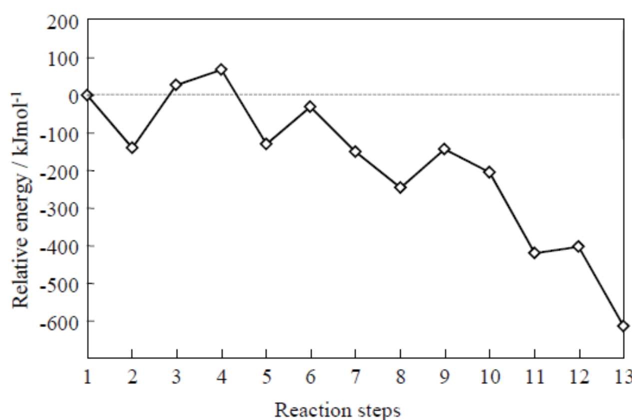

Fig. 1.1.15 Energy diagram for the oxidation reaction process of hydrazine proposed by Harrison [66].

Formaldehyde

Formaldehyde is a strong reductant with the formula CH_2O or HCHO, especially in the presence of alkalis. It is the simplest aldehyde of all organic compounds, which can be obtained by oxidizing the methanol in principle. However, this route is not industrially viable because formaldehyde is more easily oxidized than methane. The most common process to produce formaldehyde is shown as below:

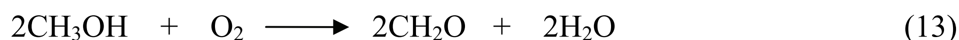

$$2CH_3OH + O_2 \longrightarrow 2CH_2O + 2H_2O \quad (13)$$

Formaldehyde was first reported in 1859 by A. Butlerov [67], and was conclusively indentified in 1869 by W. von. Horfmann [68]. Despite formaldehyde was not isolated and purified until 1892, this was achieved by F. V. Stradonitz. After then, the chemical property of formaldehyde started to be utilized in electroless Cu deposition in 1900s. The application example of formaldehyde in electroless deposition was also reported in Japan in 1934. Although it has environmental load, formaldehyde has been widely applied in the electroless deposition process for its advantages in its cost and the reactivity on the Cu substrates.

The theoretical analysis of the reaction mechanism of formaldehyde, relating to other aldehydes, was reported by T. Shimada et al. [69]. In their report, the total reaction pathway of aldehydes was proposed as shown in Fig. 1.1.16. Meanwhile, Figure 1.1.17 shows the energy profile for the oxidation process of formaldehyde to estimate the reaction pathway [70]. Our interests are highly motivated by these theoretical results of the simplest organic compounds such as formaldehyde.

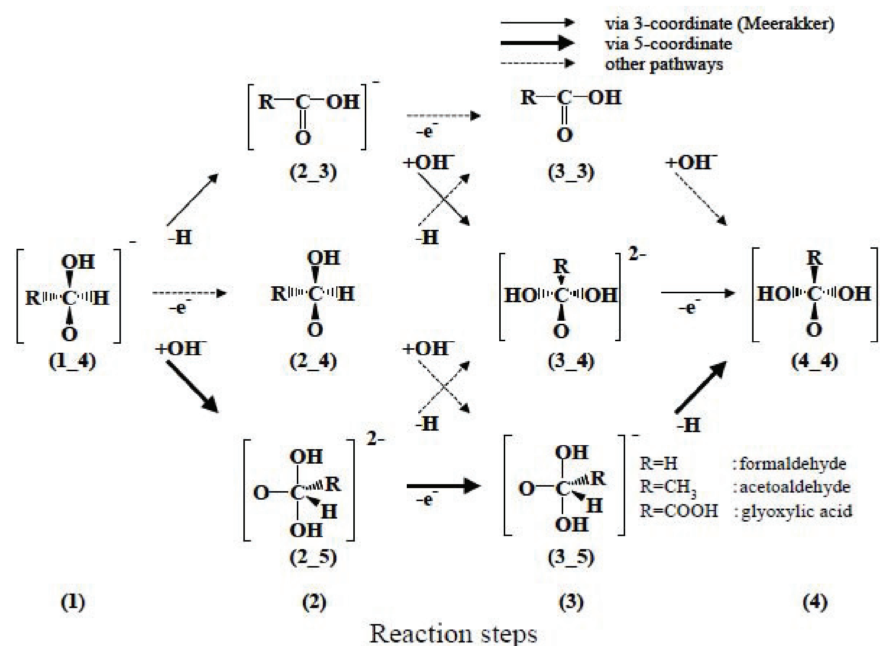

Fig. 1.1.16 Reaction pathways for the oxidation process of aldehyde via all intermediates [69].

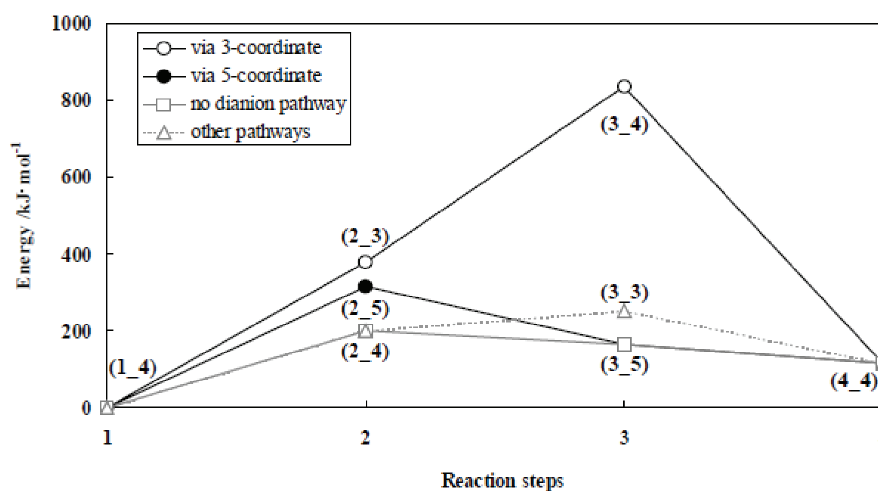

Fig. 1.1.17 Energy diagram for the oxidation reaction process of formaldehyde via 3-coordinate intermediates (○); via 5-coordinate intermediates (●); via dianion free intermediates (□); and other pathways [70].

1.1.4 Catalytic activity of metal surfaces

Electroless deposition process involves the catalytically-activated anodic reaction of reductants and the cathodic reaction of metal ions. In this process, the catalytic effect of metal surfaces on the oxidation reaction of the reductants plays a key role. Since the deposited metal surfaces become the reaction field and act as the catalytic surfaces, understanding and controlling the mechanisms of catalytic activity of metal surfaces are significant to design and develop the fine electroless deposition process.

Although some information of various reductants were shown in previous section such as development, and the oxidation mechanisms, it did not take into account other factors, especially the metal surfaces. The significant of catalytic activities of each metal surface on the reaction of major reductants was shown in Figure 1.1.4 [19]. Thus, this section attempts to introduce some aspects of catalytic activity of metal surfaces through exhibiting the catalytic activity of some important metal surfaces such as Cu surface, Ag surface, and Ni surface.

Cu surface

Cu surface can be selectively plated on various substrates; and it can exhibit catalytic activity on many reductants. Huge numbers of research for reactions on Cu surface have been investigated by various methods. One of them was the analysis of hydrogenation of CO_2 to methanol on Cu surface, as shown in Figure 1.1.18 [71]. In the figure, the geometries of intermediates in the pathway, the transition state, and the energy diagram were calculated to elucidate the rate-determining step.

Figure 1.1.19 shows the energy profile for the oxidation of hydrazine on the Cu surface. In the figure, the horizontal axis is the reaction steps, which corresponds to Fig. 1.1.14 proposed by Harrison [66]. In vertical axis, energy is plotted with respect to the energy level of hydrazine in the isolated system. Lower energy and profile show more stable condition. This calculation result indicated that Cu surface received only one electron from the first step of the oxidation reaction of hydrazine, which triggers the following reaction explosively over the deposited Cu surface; it also helped to correspond the explanation of experimental results that hydrazine was easily decomposed itself and unstable reductant.

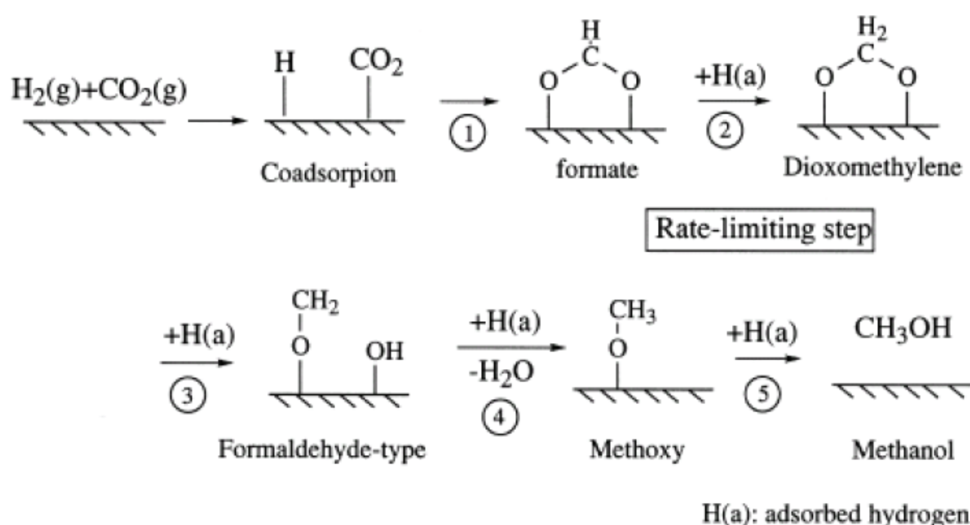

Fig. 1.1.18 Proposed reaction mechanism of the hydrogenation of CO_2 to methanol on a Cu (100) surface [71].

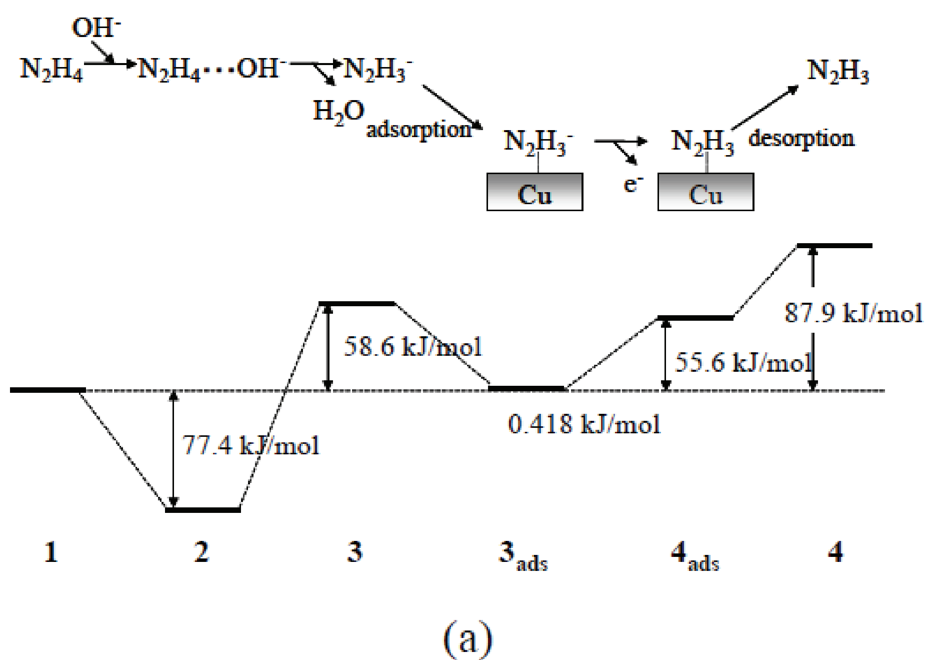

(a)

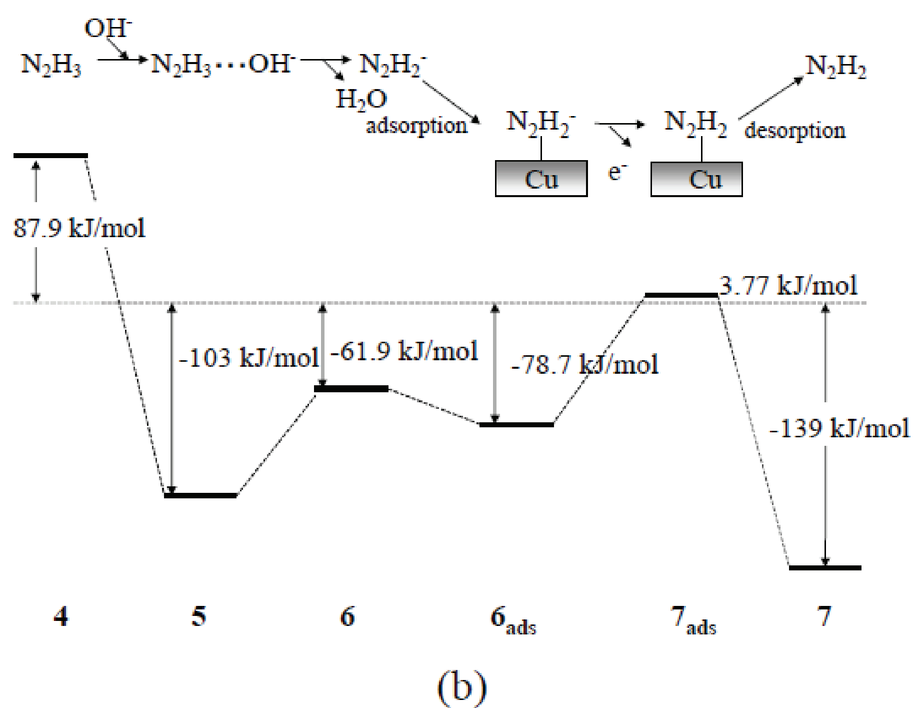

(b)

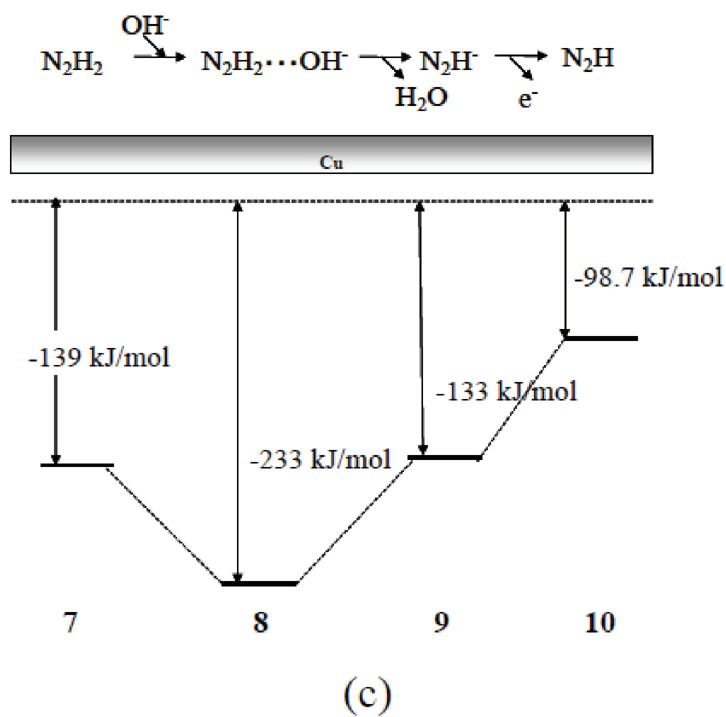

(c)

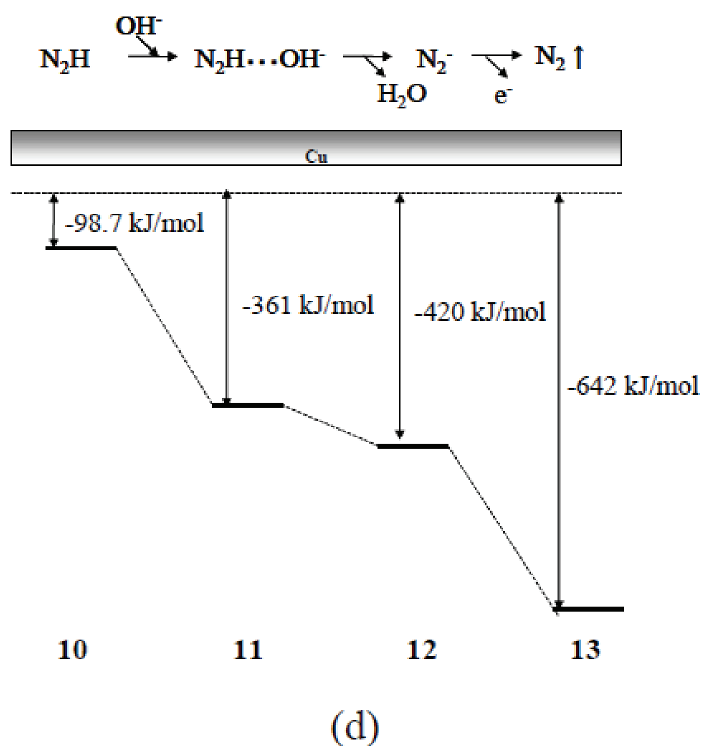

(d)

Fig. 1.1.19 Energy diagram for the oxidation reaction process of hydrazine on Cu surface proposed by Harrison, (a): $N_2H_4 \rightarrow N_2H_3$; (b): $N_2H_3 \rightarrow N_2H_2$; (c): $N_2H_2 \rightarrow N_2H$; and (d): $N_2H \rightarrow N_2$.

Ag surface

Ag surface is not only a uniquely effective catalyst for the oxidation of reductants but also plays an important role in fast deposition of particles on substrates. Therefore, Shimada et al. investigated the oxidation process of reductants on the Ag surface [70]. In their report, the energy profile for the oxidation process of three reductants (DMAB, hypophosphite ion, and formaldehyde) via five-coordinate intermediate species, in isolated system and on the Ag surface, was shown as Figure 1.1.20. In the figure, the relative energy is plotted with respect to that of each initial species; and the horizontal axis indicates the reaction steps as shown in Figure 1.1.21 [70]. Fig. 1.1.20 implies that the energy levels of every intermediate species are stabilized on the Ag surface. It is assumed that the oxidation reaction of every reductant took place on the Ag surface rather than in the isolated system. The five-coordinate intermediate is the most destabilized species, which indicates that the rate-determining step of the pathway is the coordination of OH^- to the reductant (step 1 to step 2). Moreover, the energy level of the intermediate decreases on the Ag surface rather than in the isolated system. These results strongly suggest the importance of the metal surface for the electroless deposition process.

Ni surface

Ni surface can also exhibit strong catalytic activity on many reductants, as shown in Figure 1.1.4, which is one of the most suggestive works of Ohno et al. [19]. Moreover, Figure 1.1.22 shows that hypophosphite ion adsorb onto the Ni surface; and donate electrons to the surface (oxidation) or accept electrons from the surface (reduction) to form deposited elemental phosphorous, proposed by Yin et al. [72]. Kunimoto et al. also analyzed the interaction between thiourea and the Ni surface using projected density of states (PDOS) profiles of each component, as shown in Figure 1.1.23 [73]. This figure show two significant interactions between thiourea and the Ni surface in the area around -6 eV and in the area around -2 eV; in both interactions, the S atom has a much larger contribution than the other atoms in thiourea. Therefore, they suggested that thiourea should interact with the Ni surface via a S atom, which stimulates our interests.

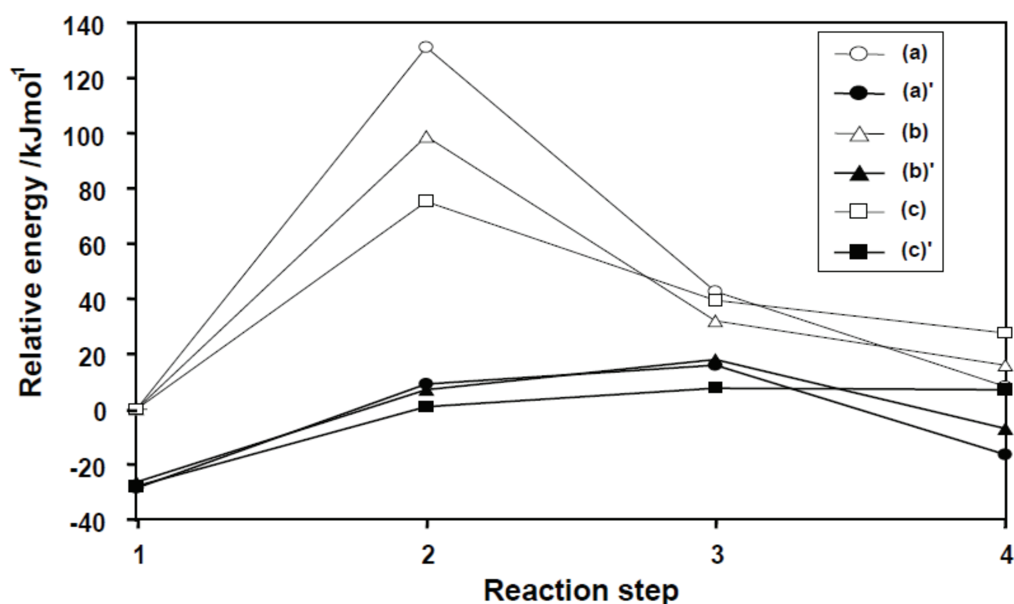

Fig. 1.1.20 Energy diagram for oxidation reaction process of (a) dimetylamine borane in isolated system; (a)' dimetylamine borane on a Ag surface; (b) hypophosphite ion in isolated system; (b)' hypophosphite ion on a Ag surface; (c) formaldehyde in isolated system; and (c)' formaldehyde on a Ag surface via five-coordinate intermediates [70].

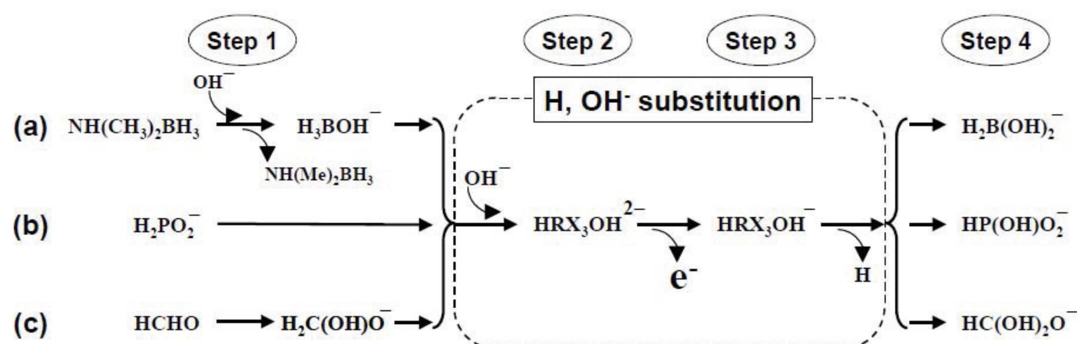

Fig. 1.1.21 Reaction pathways for oxidation process of (a) dimetylamine borane, (b) hypophosphite ion, and (c) formaldehyde via five-coordinate intermediates HRX_3OH^{n-}; (a): R = B, X = H, OH^-, (b): R = P, X = H, OH^-, and (c): R = C, X = H, O, OH^- [70].

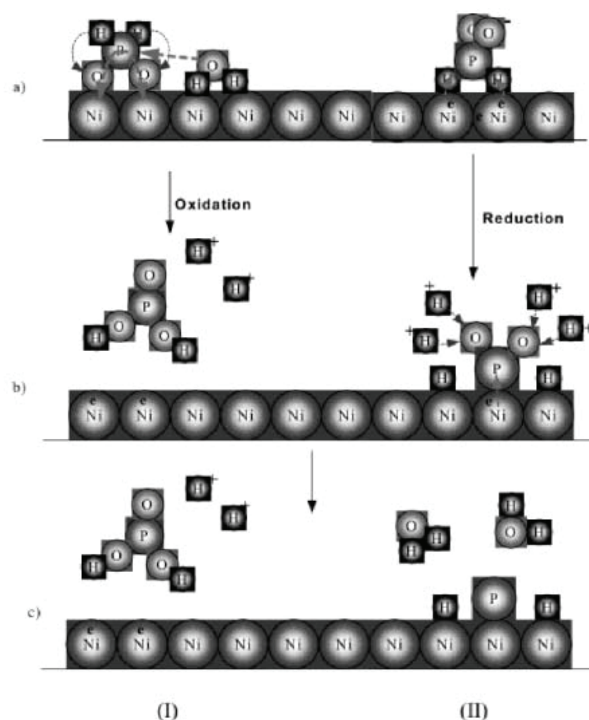

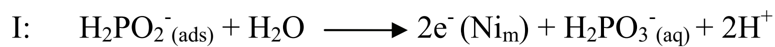
I: $H_2PO_2^-{}_{(ads)} + H_2O \longrightarrow 2e^- (Ni_m) + H_2PO_3^-{}_{(aq)} + 2H^+$

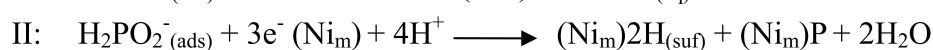
II: $H_2PO_2^-{}_{(ads)} + 3e^- (Ni_m) + 4H^+ \longrightarrow (Ni_m)2H_{(suf)} + (Ni_m)P + 2H_2O$

Fig. 1.1.22 Sketch to show the two different reaction pathways through which hypophosphite ions are converted to orthophosphate and phosphorus, respectively [72].

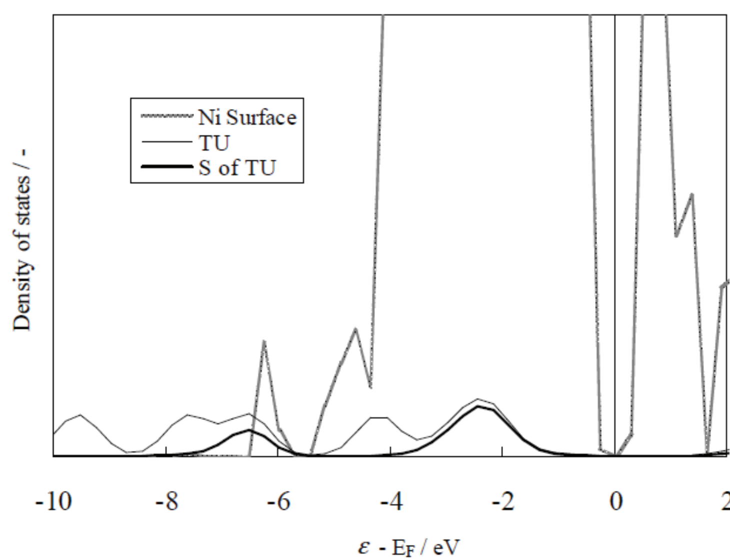

Fig. 1.1.23 PDOS profiles of adsorbing system of thiourea (TU) on the Ni surface as projected on the Ni surface, TU, and the S atom of TU [73].

1.1.5 Effects of various factors

There are a number of expected experimental factors that affect the behaviors of electroless deposition except the two most crucial factors (the reactivity of the reductants and the catalytic activity of the metal surfaces.), such as solvent effects, surface morphology, and additives. The following parts briefly introduce each factor.

Solvent effects

Solvent effects are not primal but secondary to influence the relationship between reductants and metal surfaces. It is the group of effects that a solvent has on chemical reactivity, which can have an effect on the reaction rate of the reaction balance, and even the reaction mechanism.

To elucidate the oxidation mechanisms of various reductants, other factors were considered in the electroless deposition, especially the solvent effects. The virtual solvent model is usually the solvent effect as solute distribution in with uniform properties Continuous media (Continuum), also known as the reaction field. There are many models of Continuum, as most commonly used is the Polarization Continuum Model (PCM). Some other commonly used continuum models include Onsager, Conductor-like Screening Model (COSMO), Solvation Model “x” (SMx) etc… PCM was first proposed by Tomasi et al. in 1981 [74]. In their study, PCM defined the cavity as the uniform of a series of interlocking atomic spheres. In addition, the Isodensity PCM (IPCM) model defined the cavity as an isodensity surface of the molecule [75].

Using the PCM model, some past studies elucidated the reaction path and the reactivity of the agents in the solution [76,77]. One of them was the analysis on the solvent effect of the oxidation of $TiCl_3$ using SCRF-IPCM method, as shown in the Figure 1.1.24, proposed by Shimada et al.. One of the models for systems in non-aqueous solution is referred to as Self-Consistent Reaction Field (SCRF) methods. In the figure 1.1.24, the results for hypophosphite ion and DMAB were plotted, which showed that only the reaction in the inner layer was exothermic. Thus, the oxidation reaction of the reductants is expected to proceed preferentially at the solid-liquid interface. To demonstrate the oxidation mechanisms of reductants on metal surfaces, the solvent effect must be considered by PCM model in the electroless deposition process.

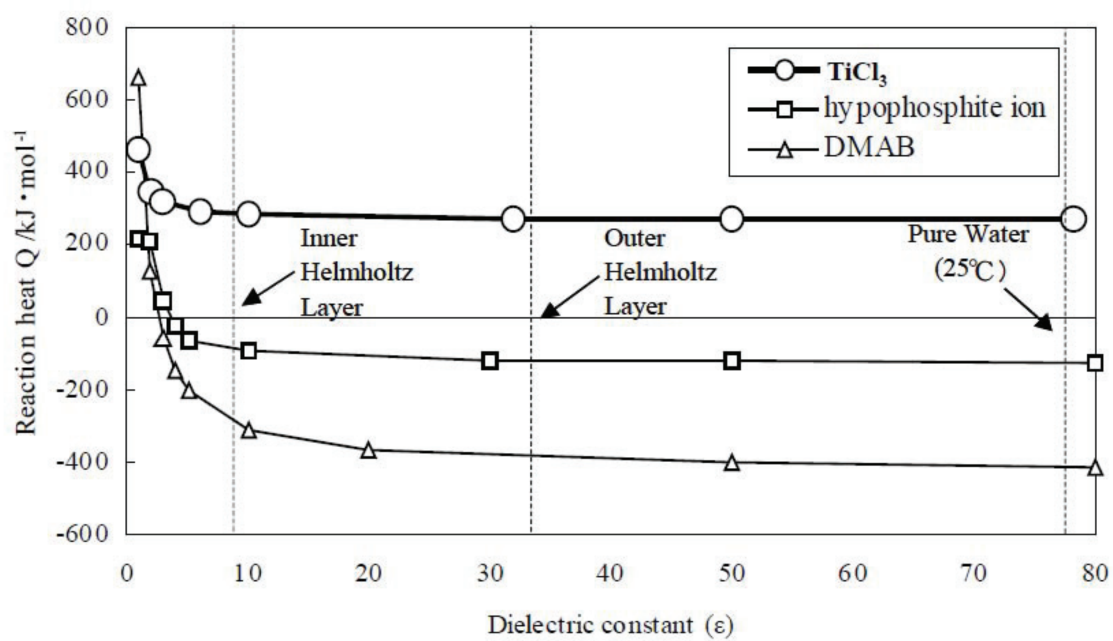

Fig. 1.1.24 Solvent effects on the substitution reaction of $TiCl_3$.

Surface morphology

Over the last several years it has been determined that several factors affect the electroless deposition process, one of which is surface morphology. Surface morphology is well known to importantly influence the behavior of catalytic reactions, because it can significantly influence the electronic states of surface and the geometry of adsorption sites of some molecules. Thus, many researchers have interest in this field, especially the research field of the catalytic chemistry.

The effect of the surface morphology for hydrogen elimination reaction was investigated by Shimada et al.. In their work, it suggested that the reactivity per each reaction reductant depended on the surface orientation, and the surface morphology affected the catalytic activity for the electroless deposition. Moreover, the surface morphology should significantly influence the behavior of the surface reaction in the electroless deposition as described in their studies. Therefore, in order to clarify the reaction mechanisms of electroless deposition, the factor of surface morphology should be considered carefully.

Additives

The electroless deposition reaction is inherently unstable, for the reason that small amount of additives added into the electroless deposition bath can significantly influence the deposition behaviors, such as acceleration or suppression effect on the deposition. Additives present in the electroless deposition bath can influence: (i) kinetics and mechanism of the crystal growth process; (ii) the bath passivation process; (iii) structure and morphology of the deposit; (iv) physical properties of metal deposit; and (v) purity of deposit [78-80].

The first analysis of the additive effects on the electroless deposition was proposed by Sallo et al. [81]. In their work, the influences of thiourea on the electroless Ni deposition process were investigated. After then, a few publications on the effect of thiourea on the electroless Ni deposition process were achieved. Among them, Kunimoto et al. analyzed the accelerating effect of thiourea on the electroless Ni deposition using hypophosphite ion, as the first step of the series of the investigation for thiourea [73]. In the study, a bath system in which the anodic and cathodic reactions are physically separated was constructed, as shown in Figure 1.1.25. To indentify which reaction, anodic or cathodic, was most influenced by thiourea, current density was measured in both the case in which thiourea was added only to the anodic reaction and the case in which thiourea was added only to cathodic reaction bath, as shown in Figure

1.1.26. Although their results indicated that thiourea had an acceleration effect on both the anodic and cathodic reactions, the acceleration effect was mainly derived from acceleration of the anodic reaction. Based on this conclusion, they also analyzed the influence of thiourea on the deposition process on a molecular level by DFT focusing on the anodic reaction of the hypophosphite ion. As a result, they demonstrated that the accelerating effect of thiourea primarily affects the anodic reaction of the hypophosphite ions, while its effect on adsorption is thought to be most important.

In a word, the chemistry of additives involves many suggestions for the electroless deposition process, which is necessary to be much more properly applied to improve the efficiency and quality of the process. To achieve such further improvement, it is obviously necessary to know more about the additive behaviors in the electroless deposition process for details.

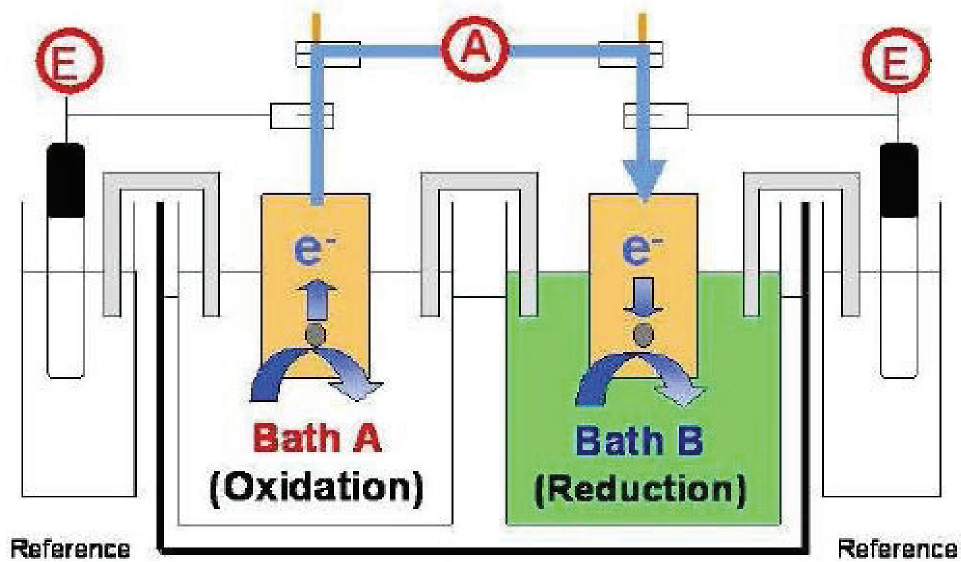

Fig. 1.1.25 Composition of the separated bath system [73].

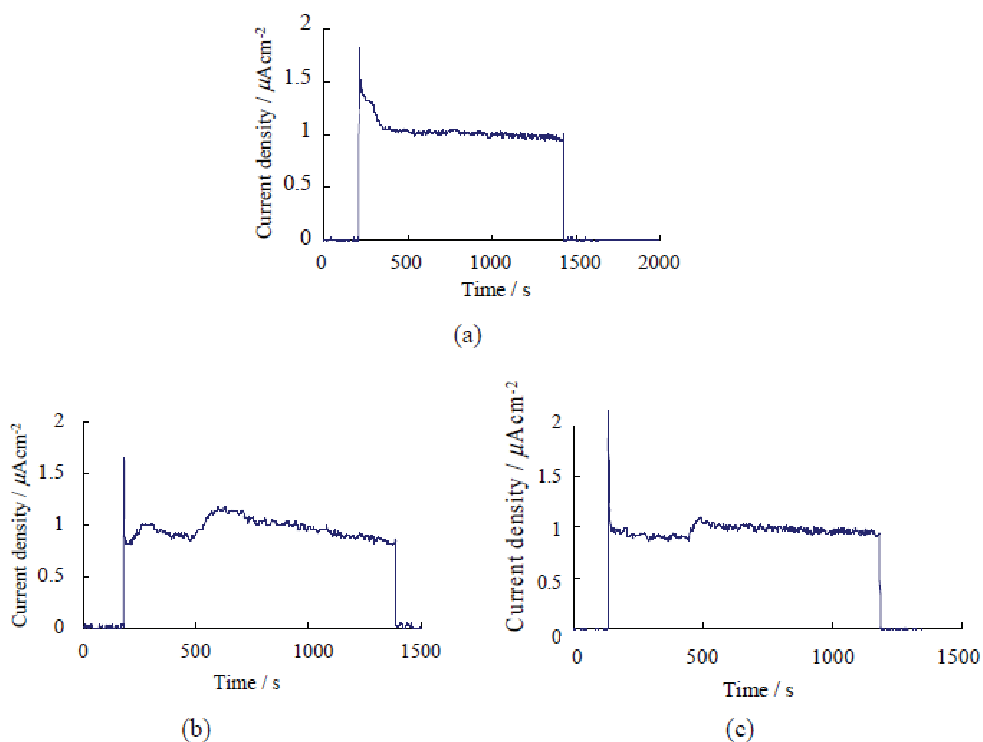

Fig. 1.1.26 Time dependency of current density with (a) no thiourea added; (b) thiourea added only to the anodic reaction bath; and (c) thiourea added only to the cathodic reaction bath [73].

1.2 Surface enhanced Raman spectroscopy

The experimental techniques have been widely applied to elucidate some chemical phenomena in the research fields of analytic chemistry. Among experimental approaches, one of the most frequently used is the Surface Enhanced Raman Spectroscopy (SERS). Some other commonly used are X-ray diffraction (XRD), Neutron scattering, and Infrared spectroscopy (IR spectroscopy) etc... Although these methods have many advantages, they have their respective disadvantages summarized below:

XRD, which is developed by Bragg et al. in 1913 [82], has disadvantages as follows [83]: i. Special training and experience is necessary to use this method; ii. The initial high cost of diffraction equipment; iii. The necessity of having standard patterns for comparison before the diffraction pattern of the unknown can be meaningful; and iv. The weak diffraction peaks of some substances.

Neutron scattering, which is first proposed by Shull et al. in 1949 [84], has disadvantages as follows: i. Neutron sources are weak; ii. Neutrons are generally not selective for particular elements; and iii. Kinematic restrictions.

The disadvantages of IR spectroscopy are as follows: i. Atoms or monatomic ions do not have infrared spectra; ii. Homonuclear diatomic molecules do not posses infrared spectra; and iii. Complex mixture and aqueous solutions are difficult to analyze using infrared spectroscopy.

SERS effect is a breakthrough technique that can provides in-situ, ultrasensitive characterization of chemicals on metals down to single molecular level for analysis of solid-liquid interface [85,86]. In general, molecular level detection at solid-liquid interface by SERS sensors has been investigated by applying plasmonic metal either with roughened surfaces or nanostructures [87-89]. An amplification of the Raman signal due to the electromagnetic field depends crucially on the size of the plasmonic metals and the distance from the plasmonic metals in the range of 1-2 nm [90-93]. Thus, it is difficult to define the place where the detected molecules are existed, which stimulates this study to overcome the problem.

Since the experimental approaches involve several categories each with its own advantages and disadvantages; and each methodology should be used in proper application. In this section, thus, some fundamental information about SERS like concepts, mechanisms, and development will be introduced, because SERS play a very important role in the experimental analyses on the characterization of chemicals at the

solid-liquid interface. Moreover, some examples of SERS and their recent applications will also be introduced in the following parts.

1.2.1 Outline of surface enhanced Raman spectroscopy

Raman spectroscopy is a powerful technique which has become one of the optical workhorses in analytical chemistry where it is used to detect and quantify a variety of chemical substances [94]. The phenomenon of inelastic scattering of light was first postulated by Smekal in 1923 [95], and first experimentally observed in 1928 by C. V. Raman and K. S. Krishnan [96]. When a monochromatic light (at frequency v_0) illuminates molecules with internal modes of vibration (at frequency v_{mol}), a very small portion of the incident light is scattered off from the molecules with its color either red or blue shifted (from v_0 to v_0'), as shown in Figure 1.2.1. The frequency difference between the incident light and the scattered light equals to the molecular vibrational frequency:

$$v_0 = v_0' \pm v_{mol} \quad (14)$$

Since then, this phenomenon is referred to as Raman effect.

A simple explanation for the principle of Raman spectroscopy is the following: the incidental photons are destroyed and their energy is used for creating scattered photons and creating ($v_0' - v_{mol}$, stokes process (red shifted)) or destroying ($v_0' + v_{mol}$, anti-stokes process (blue shifted)) vibrations in the studied sample. Raman spectroscopy involves molecular and crystal lattice vibrations and is therefore sensitive to the composition, bonding, chemical environment, phase, and crystalline structure of the sample material in any physical form: gases, liquids, solutions, and crystalline or amorphous solids. However, the low cross-section, and intrinsically weak limits its applications. The introduction of surface enhanced Raman spectroscopy (SERS) in 1974, which was reported by Fleischmann et al. [97], has attracted a lot of attention from researchers due to large enhancement of weak Raman signal; and it facilitates identification in chemical and biological systems [98].

SERS is a technique that takes advantage of the fact that the plasmon structure enhances both the excitation and scattering processes. It can provide greatly enhanced Raman signal from Raman active analytic molecules that have been adsorbed on certain specially prepared metal surfaces. It also has the capability of detecting analyses at the

single molecule level, because the Raman signals can get efficiently enhanced up to 11 to 14 orders of magnitude by an interaction of analytic molecules with a nanostructured metallic surface [99]. Figure 1.2.2 shows localized surface plasmons may dramatically enhance the otherwise intrinsically weak Raman scattering [100]. In the figure, (a) is the energy diagram for the Raman scattering process involving the absorption of an incident photon with energy ħw, and a subsequent emission of a photon with energy ħw' via an intermediate virtual state in a molecule. The scattering is inelastic and the scattered light is Stokes shifted by Δw = w – w'; (b) is the metallic periodic structure composed of infinite half-cylinders of radius R. The normal incident electrical field E_i is polarized transverse to the cylinders; and (c) is the magnification of the groove structure indicating the nanoscale cutoff modelled by a finite radius of curvature δR.

There are two widely accepted mechanisms contributing to the SERS effect: an electromagnetic enhancement and a chemical enhancement. The electromagnetic effect is dominant, while the chemical effect contribute enhancement only on the order of an order or two of magnitude [101]. The chemical enhancement involves changes to the adsorbate electronic states due to chemisorptions of the analyte [102], while the electromagnetic enhancement is dependent on the presence of the metal surface's roughness features.

The pioneers summarized the key features of SERS and listed briefly as below [103-105]:

• SERS occurs when molecules are brought to the metal surfaces in varieties of morphologies. The smooth surface is not active for the enhancement.

• Surface roughness in the scale from 10 to 200 nm with appropriate preparation is crucial to produce a strong SERS signal. The roughness at atomic scale, such as certain ad-clusters, ad-atoms, kinks, steps or vacancies can assist further enhancement.

• SERS has been observed at solid-liquid, solid-gas, and solid-solid interfaces as an interface-sensitive technique. Although molecules adsorbed in the first layer on the surface show the largest enhancement, the enhancement also has some long-range aspect of about tens of nanometers.

• The excitation profile (scattering intensity vs. exciting frequency) deviates from the fourth power dependence of normal Raman scattering.

• Large numbers of molecules adsorbed on metal surfaces exhibit SERS, but their enhanced factor values could be very different. It depends on the bonding type between metals and molecules.

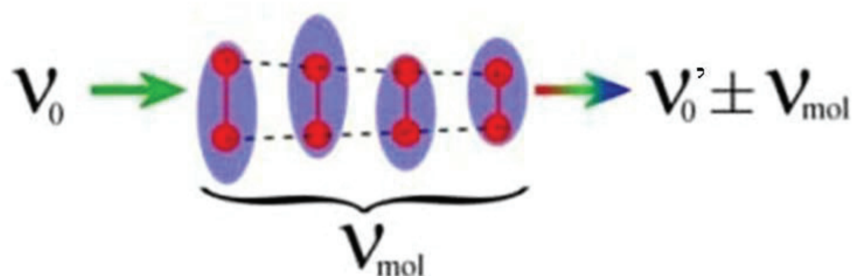

Fig. 1.2.1 Schematic drawing of Raman scattering.

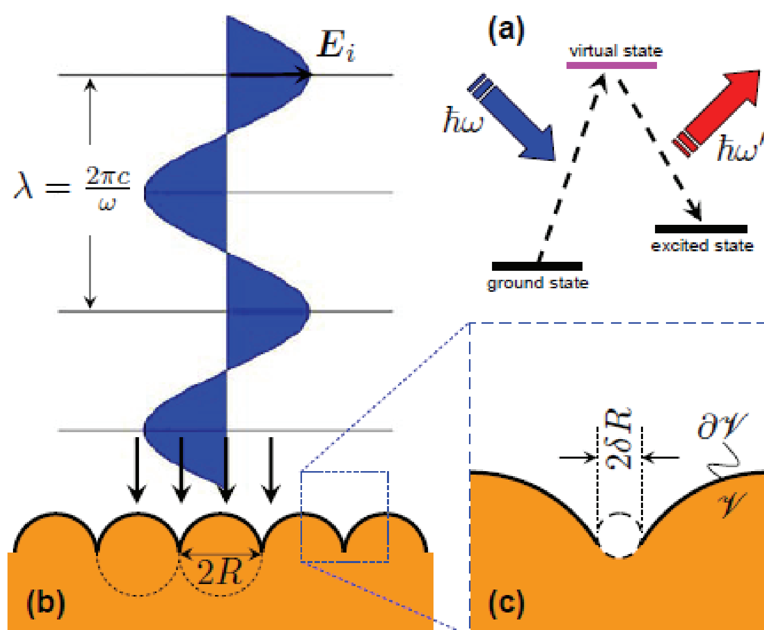

Fig. 1.2.2 Schematic illustration of Raman scattering enhanced by localized surface plasmons [100].

1.2.2 Examples of surface enhanced Raman spectroscopy

Many efforts have been made to design and fabricate SERS substrates that routinely deliver high enhancement factors in recent decades. It is well known that some typical structures can generate strong SERS effect such as antennas with small gap, double resonance substrates, and antennas integrated with gratings; owing to electromagnetic enhancement originating from surface plasmon coupling. Thus, this section introduces some typical examples of SERS substrate and their recent applications in the following parts.

Antennas with small gap

The "dimer" structure, consisting of two metallic nanoparticles separated by a small gap, can generate effective SERS. It is commonly believed that substantial electromagnetic field generated in dimer gaps is one of the main enhancement mechanisms in SERS. This motivates the development of a reproducible method for the fabrication of antennas with small gaps, especially below 10 nm.

Zhu et al. have developed a lithographic fabrication technique that enables fabrication of arrays of antennas with gap size well below 10 nm are shown in Figure 1.2.3 [106]. In the figure, (a) shows the SEM image of the antenna with gap size well below 10 nm; (b) shows that the enhancement factor can be high as 1.1×10^8 from arrays of dimer structure with gap sizes as small as 3 nm. Furthermore, a substrate with gap size as 5 nm based on silver nanoparticle was developed by Wang et al. [107], as shown in Figure 1.2.4. By comparison with SERS substrates made from metallic colloids and roughened metal surfaces, in their study, the low variation of the enhanced Raman signal over various substrates further indicates that the Raman enhancement effect can be attributed to the fact that the substrate has the gaps between neighboring nanoparticles.

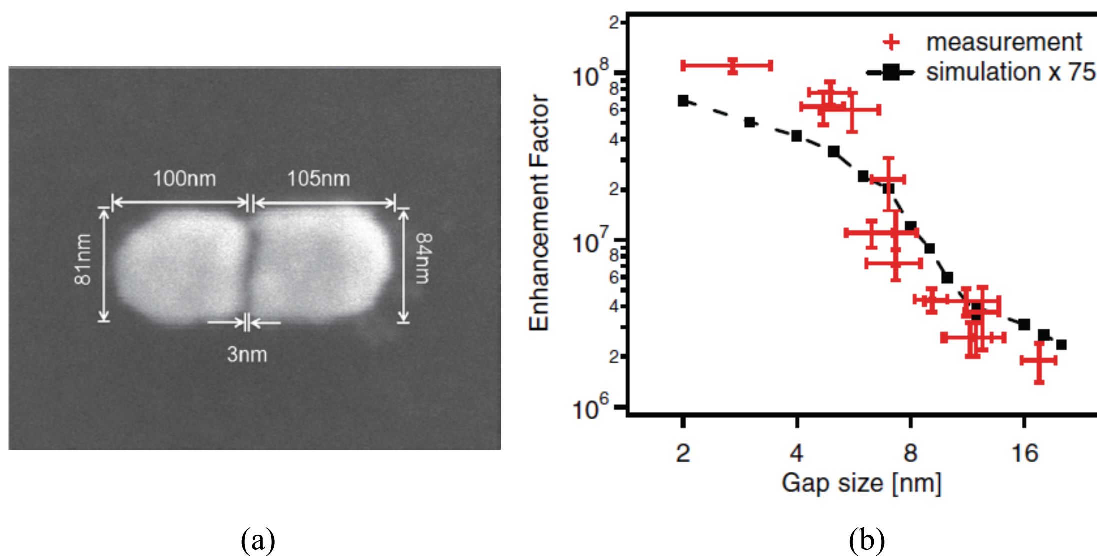

(a) (b)

Fig. 1.2.3 (a) SEM image of antenna with gap size well below 10 nm; (b) Measured SERS enhancement factor as a function of gap size [106].

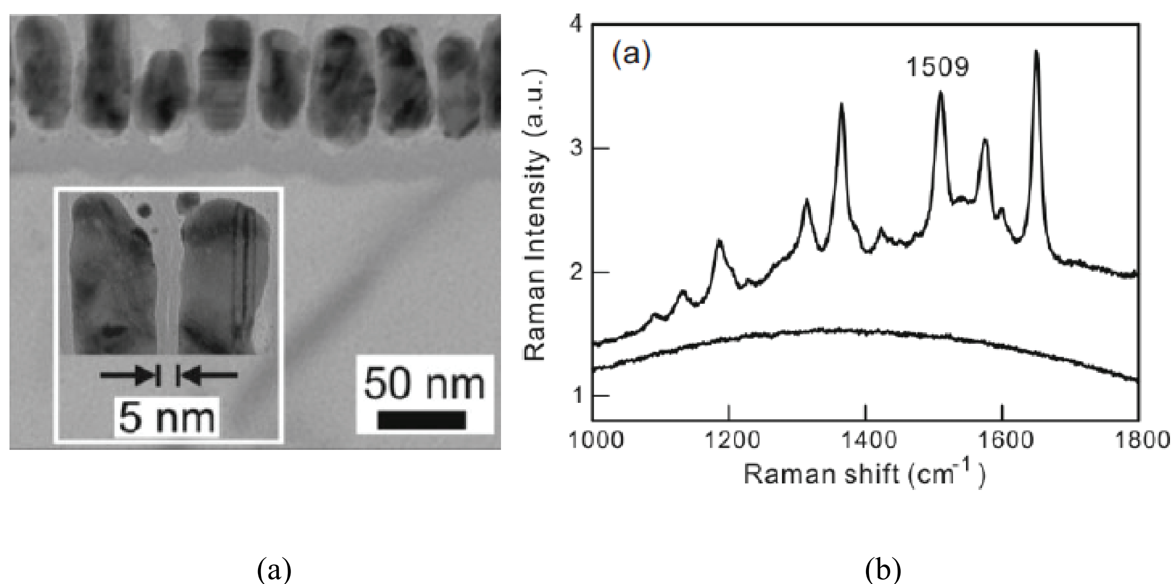

(a) (b)

Fig. 1.2.4 (a) SEM image of the substrate; (b) SERS spectrum of 10^{-6} M R6G solution on the substrate (top); and on a typical SERS substrate prepared by depositing 30 nm Ag on Si (bottom) [107].

Double resonance substrates

The enhanced local fields generated by antennas are crucial to boost the normally weak Raman signals of molecules. As the source of huge local fields, the localized surface plasmon resonances (LSPRs) of antennas have been intensively investigated. LSPRs of metal nanoparticles strongly depend on their shape, size, arrangement, for pairs of closely spaced nanoparticles, and the width of the gaps between them [108-110]. Moreover, it has been shown that SERS enhancement factor is maximized if the LSPR frequency is positioned between pump and stokes frequencies.

Recently, many structures with double resonances have been developed. By appropriate design, these structures can be positioned to between pump and stokes frequencies, enabling the SERS enhancement factor to be increase. Figure 1.2.5 shows the double resonance structure which consists of a square array of metal disks formed above a metal film with a SiO_2 spacer layer in between them. The structure was proposed by Chu et al. [111]. In their work, they designed the structure so that modes match the pump and stokes frequencies as shown in Fig. 1.2.5 (c), where it can be seen that the outermost peaks of the extinction spectrum (which approximates the near-field enhancement) match the pump and strokes frequencies (at 1072 cm^{-1}). Their results indicated that the double resonance structures have SERS enhancement factors about two orders of magnitude larger than their single resonance counter parts (gold disks on glass).

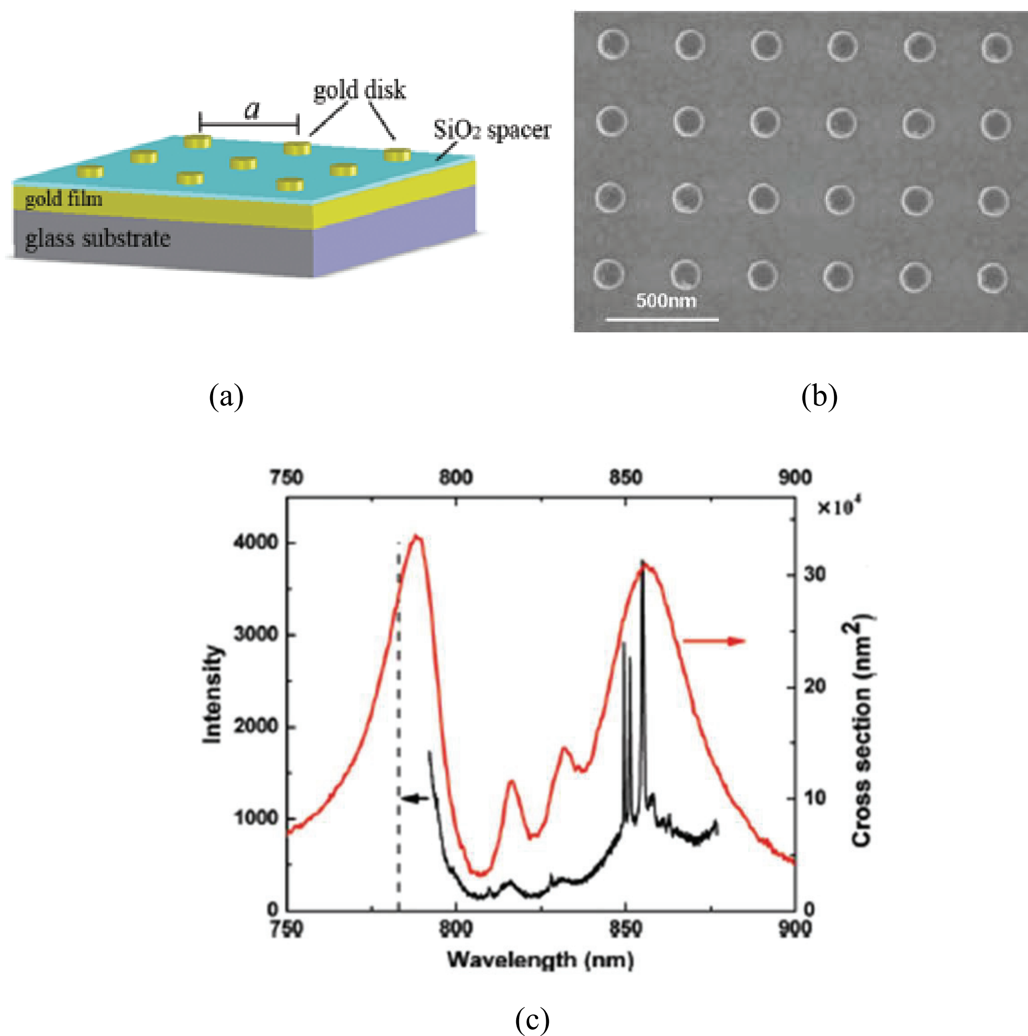

(a) (b)

(c)

Fig. 1.2.5 (a) Schematic of double resonance SERS substrates; (b) SEM image of fabricated double resonance SERS substrates; (c) Red: measured extinction cross section of double resonance SERS substrates; Black: measured Raman scattering spectrum; Dashed line is the pump wavelength [111].

Antennas integrated with gratings

Previous studies have frequently measured SERS from molecules on metal particles such as dimmers, sitting on dielectric substrates etc... Microscope objective lenses are typically used to focus the excitation light onto the particles, and to collect the SERS emission. In recent researches, some additional nanostructures have been developed to improve the SERS effect.

An advanced antenna with surrounding nanostructures has been proposed by Yanagisawa et al. [112]. In their design, the antenna is integrated with metallic gratings that simultaneously concentrate the incident illumination and collimate the SERS emission. The SEM image of the antenna is shown in Figure 1.2.6. In the figure, it can be seen that the structure of antenna is designed as the concentric pattern, which consists of six lines and spaces with a pitch of 550nm and a center dimple with a diameter of 250nm, using Finite-Difference Time-Domain (FDTD) calculation. In the response to the illumination, the ring gratings generate surface plasmon waves that converge to the center. Figure 1.2.7 shows Raman spectra of the antenna (a) at the center and (b) at the outside. The results indicate that the Raman enhancement at the center of the device was estimated to be 2,000 times greater than it was at the outside of the device. Therefore, the antenna that they developed offers promising potential for the detection of an unknown single molecule and for applications such as sensors and solid-liquid interfaces with a high sensitivity and a high space resolution, which stimulates our interests.

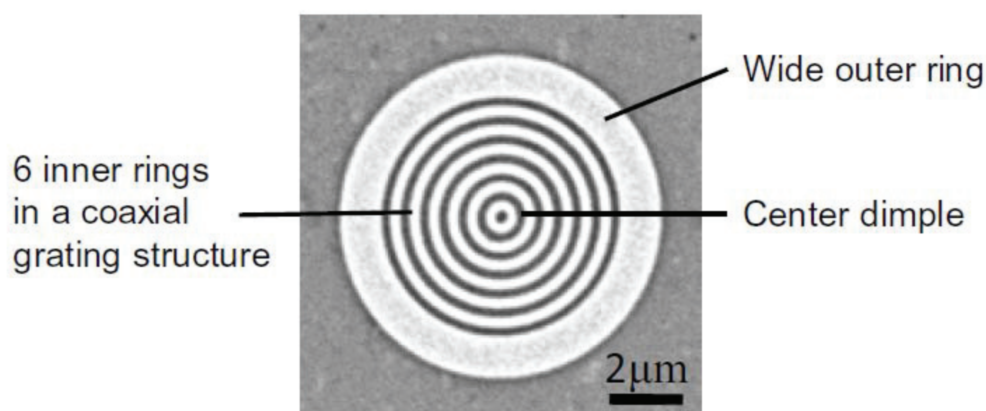

Fig. 1.2.6 The SEM image of the antenna proposed by Yanagisawa et al. [112].

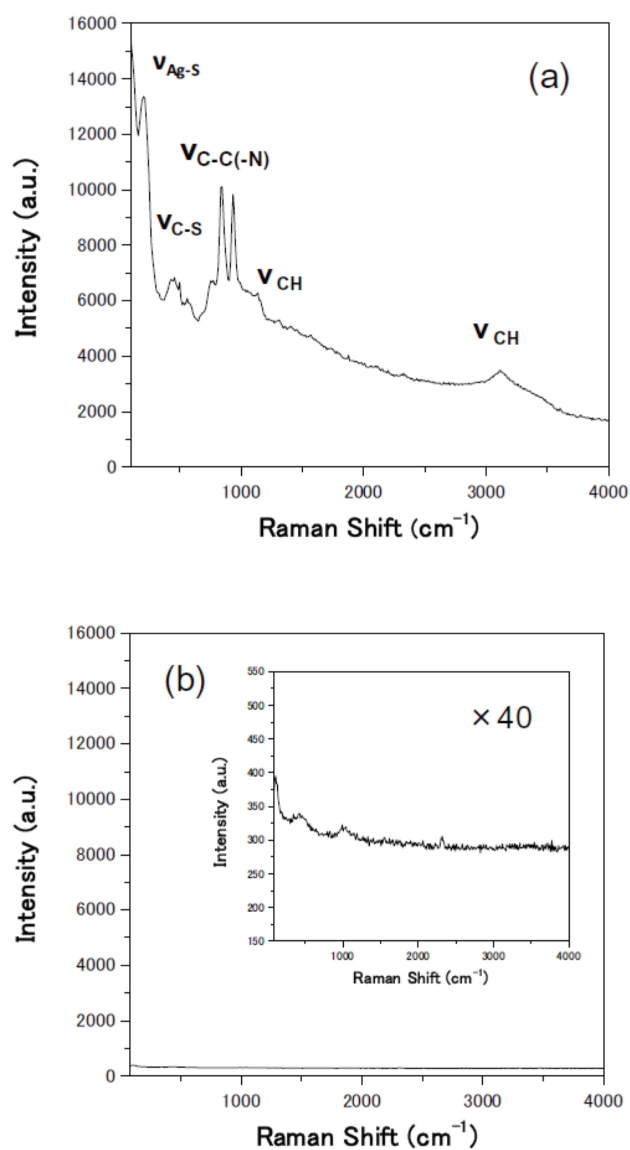

Fig. 1.2.7 Raman spectra of the antenna (a) at the center and (b) at the outside [112].

1.2.3 Theoretical approaches

Theoretical approaches have been widely applied in the research fields of analytic chemistry to support and compare with experimental analyses. As a result of the development of numbers of remarkable calculation theories and the progress in the computing technology, computational chemistry has been focused as an important and powerful tool which can provide the chemists with information difficult to obtain using experimental procedures.

Computational chemistry is a branch of chemistry that uses principles of computer science to assist in solving chemical problems, and uses the results of theoretical chemistry to calculate the structures and properties of molecules and solids. It mainly involves two types of simulation techniques, quantum chemical simulation and molecular simulation.

The quantum chemical simulation, benefited from various theoretical approximations in computational simulation over the last century, is the technique that simulates the behaviors of electrons around some atoms or molecules and calculates the interaction between them [113,114]. In principle, it is the method to solve the stable states of molecule based on Schrödinger equation, which is very important to analyze in the field of chemistry and is one of the most important missions of the quantum chemistry research field. The quantum chemical simulations involve two major theories: i. density functional theory (DFT) that can be used to investigate the states of electrons using distribution of electron density; ii. wave function theory (WFT) that can be used to calculate the states of electron using wave function of electrons.

The molecular simulation is the molecular dynamics technique that can simulate the molecular behaviors based on classic dynamic expression. It involves two major types of method: i. Monte-Carlo (MC) simulations that are used to analyze the behavior of statistic ensembles using statistical thermodynamics; ii. molecular dynamics (MD) that are applied to analyze the time dependency of the kinetics of molecules using Newton equation.

The computational chemistry involves several categories each with its own theory and philosophy, and each methodology should be used in proper application. In this section, thus, DFT calculation and MC simulation will be introduced, which play a very important role in the theoretical analyses on the chemical reaction at the solid-liquid interface.

Density functional theory calculation

Density functional theory (DFT) for electrons in atoms, molecules and solids has a long and increasingly rich and successful history that has its roots in the early development of analytic chemistry. Over the past 20 years, DFT has become a much used tool in most branches of chemistry. Many experimental investigations in research fields of chemistry and materials routinely include such calculation, using a popular code, a standard basis, and a standard functional approximation, as shown in Fig. 1.2.8 [115].

DFT is a clever way to solve the Schrödinger equation for a many-body system [116,117]. Pure DFT methods are defined by pairing an exchange functional with a correlation functional. For example, the well-known BLYP functional pairs Becke's gradient-corrected exchange functional with the gradient-corrected correlation functional of Lee, Yang, and Parr [118,119]. Becke has formulated functionals [120], which include a mixture of Hartee-Fock theory pointed out by Kohn-Sham and DFT exchange along with DFT correlation, conceptually defining E^{XC} as below:

$$E^{XC}_{hybrid} = c_{HF} E^{X}_{HF} + c_{DFT} E^{XC}_{DFT} \quad (15)$$

where, the c's are constants. Moreover, the Becke-style three-parameter functional can be defined as below:

$$\begin{aligned} E^{XC}_{B3LYP} = & E^{X}_{LDA} + c_0 (E^{X}_{HF} - E^{X}_{LDA}) + c_X E^{XC}_{B88} \\ & + E^{C}_{VWN3} + c_C (E^{C}_{LYP} - E^{C}_{VWN3}) \end{aligned} \quad (16)$$

$$c_0 = 0.20,\ c_X = 0.72,\ c_C = 0.81$$

In the B3LYP functional, which hybridizes several functionals, the parameter values are those specified by Becke as shown above (c_0, c_X, and c_C).

Kunimoto et al. analyzed orbital interaction between hypophosphite ions and metal surfaces using DFT calculation, in which the electronic exchange and correlation energy were estimated with the generalized gradient approximation in the B3LYP functional [121]. Figure 1.2.9 shows the adsorption structure and labeling for metal atoms by DFT calculation. Hence, B3LYP functional can be applied widely to the analyses of chemistry and many purposes, which should be noted.

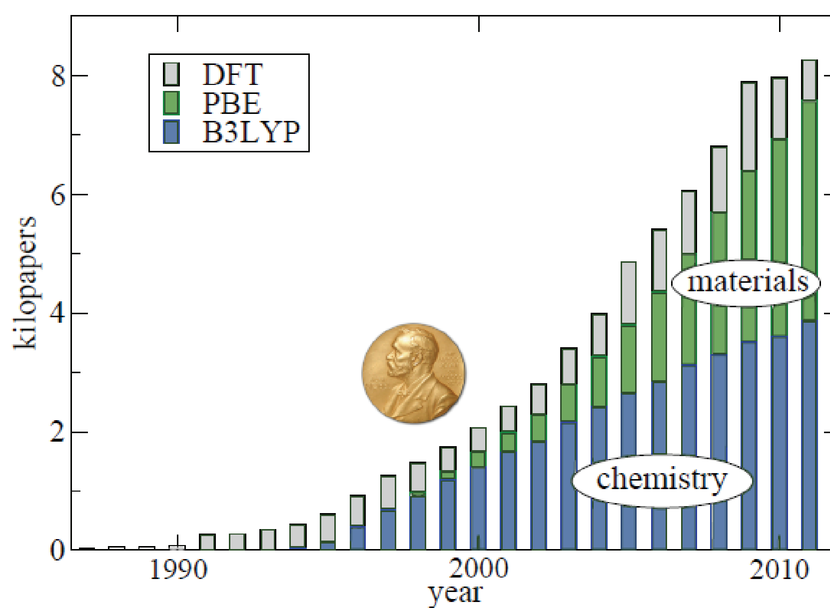

Fig. 1.2.8 Numbers of papers when DFT is searched as a topic in Web of Knowledge (grey), B3LYP citations (blue), and PBE citations (green, on top of blue) [115].

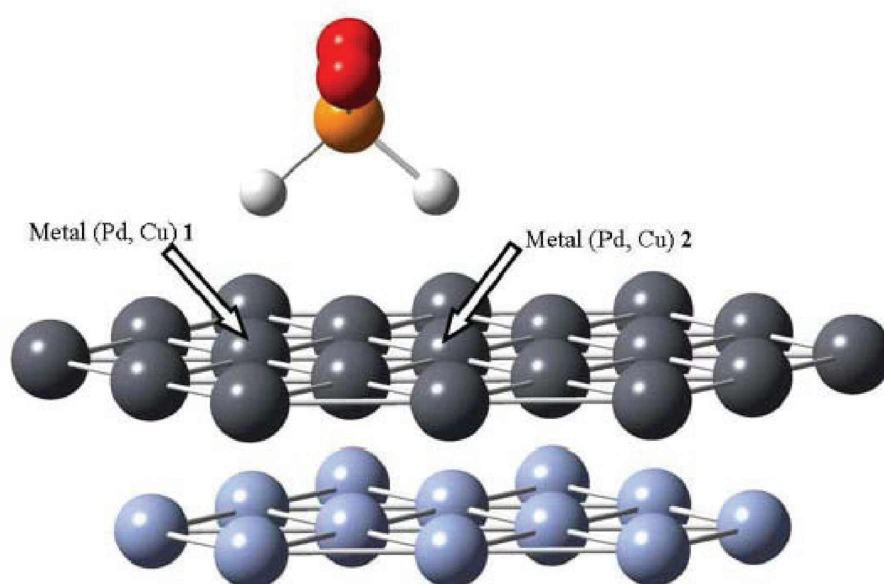

Fig. 1.2.9 The adsorption structure and labeling for metal atoms 1, 2 [121].

Monte-Carlo simulation

Monte-Carlo (MC) simulation is extensively used in various fields such as physics, chemistry, engineering, and finance that rely on repeated random sampling to compute results. In chemical systems, MC can provide the statistically rational structure of some particle ensembles by choosing randomly and evaluating the statistical adequacies of their own.

The name and the systematic development of MC date from about 1950s. Monte-Carlo first named by N. Metropolis et al. [122], who estimated for the eigenvalues of Schrödinger equation. Metropolis method originally used to sample the Boltzmann distribution; it has become one of the most widely processes. The process of Metropolis method is simply shown below:

i. The ensemble consisting of some particles is somehow prepared;
ii. One particle composing the ensemble are randomly chosen;
iii. The chosen particle is moved to the random direction and random distance so that the new configuration of the ensemble is obtain;
iv. The new ensemble is tested whether it is statistically adequate;
v. The statistically adequate samples are gathered;
vi. Using these samples, statistically average ensemble states or some physical parameters are obtained.

Although some empirical parameters and the classic force equation are applied in the energy calculation step, this method has been still used as one of the most powerful tools, which can provide very meaningful results about the large size system.

1.3 Strategy of this study

The electroless deposition process is very important for fabricating metal thin films and is widely applied for various kinds of applications; and oxidation of the reductants is a dominant factor in the electroless deposition process. However, the complexity of the reaction mechanism for reductant oxidation and additives in the process make it difficult to improve the efficiency of electroless deposition.

To achieve more precise control of the electroless deposition process for fabricating further advanced devices, it is significant to elucidate the reaction mechanisms of the process in molecular-level. Therefore, the first strategy of this study is to focus on the reaction mechanisms of reductants on each metal surface from the experimental and computational perspectives.

In order to analyze the interaction mechanisms between reductants on metal surface, the second strategy of this study is to use SERS and DFT calculation to analyze the interaction mechanism of hydrazine and hypophosphite ions on a Cu surface.

Finally, to obtain the mechanisms on the complicated behaviors of the additive in acidic/alkaline electroless deposition baths, the third strategy of this study is to focus on the acceleration and suppression effect of thiourea on the oxidation reaction of hypophosphite ions on a Ni surface.

References

[1] Pearlstein, F. *Modern Electroplating*, Lowenheim, F. A. (Ed), Wiley New York (1974).
[2] A. Brenner, and G. E. Riddell, *J. Res. Nat'l Bur. Std.*, 37, 31 (1946).
[3] A. Brenner, and G. E. Riddell, *J. Res. Nat'l Bur. Std.*, 39, 385 (1947).
[4] A. Brenner, *Plat. Surf. Finish.*, 71, 24 (1984).
[5] A. Wurtz, *Ann. Chim. et Phys.*, 3, 11 (1844).
[6] P. Breteau, *Bull. Soc. Chim.*, p. 9 (1911).
[7] F. A. Roux, U. S. patent 1, 207, 218 (1916).
[8] G. Gutzeit, *Plating*, 46, 1158 (1959).
[9] H. Gerischer, and C. W. Tobias, *Advances in Electrochemical Science and Engineering. Volume 3*, VSH, Weinheim, (1994).
[10] T. Hayashi, M. Matsuoka, and H. Nawafune, *Mudenkai-Mekki: Kiso-to-ouyo*, Nikkan Kogyo Shimbun Ltd., Tokyo, (1994).
[11] M. Saito, *J. Surf. Finish. Soc. Jpn.*, 16, 300 (1965).
[12] M. Saito, *J. Surf. Finish. Soc. Jpn.*, 17, 14 (1966).
[13] M. Saito, *J. Surf. Finish. Soc. Jpn.*, 17, 258 (1966).
[14] M. Saito, *J. Surf. Finish. Soc. Jpn.*, 17, 264 (1966).
[15] M. Paunovic, *Plating*, 55, 1161 (1968).
[16] M. Paunovic, and M. Schlesiger, *Fundamentals of Electrochemical Deposition*, John Wiley & Sons, Inc., (1998).
[17] M. Saito, *J. Met. Finish. Soc. Jpn*, 16, 300 (1965).
[18] I. Ohno, *Mater. Sci. Eng., A*, 146, 33 (1991).
[19] I. Ohno, O. Wakabayashi, and S. Haruyama, *J. Electrochem. Soc.*, 132, 2323 (1985).
[20] D. L. Graham, H. A. Ferreira, and P. P. Freitas, *Trend. Biotechnol.*, 22, 455 (2004).
[21] N. V. Myunga, D. Y. Parkb, B. Y. Yoob, and P. T. A. Sumodjo, *J. Magn. Magn. Mater.*, 265, 189 (2003).
[22] X. T. Tang, G. C. Wang, and M. Shima, *J. Magn. Magn. Mater.*, 309, 188 (2007).
[23] L. Gao, L. P. Yue, T. Yokota, R. Skomski, S. H. Liou, H. Takahoshi, H. Saito, and S. Ishio, *IEEE Trans. Magn.*, 16, 2194 (2004).
[24] H. J. Richter, A. Y. Dobin, O. Heinonen, K. Z. Gao, R. J. M. v. d. Veerdonk, R. T. Lynch, J. Xue, D. Weller, P. Asselin, M. F. Erden, and R. M. Brockie, *IEEE Trans. Magn.*, 42, 2255 (2006).

[25] T. Osaka, Y. Yamazaki, and H. Ishihara, *"Handbook of materials for recording and memory devices"*, Asakura Syoten, Japan, (2000) [in Japanese].
[26] R. Kaneko, and S. Yoshii, Reports in NTT, 31, 241 (1982).
[27] Y. Sato, et al., Reports in NTT, 36, 458 (1987).
[28] F. Goto, Y. Suganuma, and T. Osaka, *Kinzoku Hyomen Gizyustu,* 33, 414 (1982).
[29] T. Homma, T. Nakamura, J. Shiokawa, and T. Osaka, *J Mag. Soc. Jpn.*, 18, 73 (1994).
[30] T. Homma, Y. Sezai, and T. Osaka, *Electrochim. Acta.*, 42, 3041 (1997).
[31] K. Itakura, T. Homma, and T. Osaka, *Electrochim. Acta.*, 44, 3707 (1999).
[32] T. Yokoshima, Y. Yamaji, K. Kikuchi, H. Nakagawa, and M. Aoyagi, *J. Electrochem. Soc.*, 157, D65 (2010).
[33] C. D. Iacovangelo, *J. Electrochem. Soc.*, 138, 976 (1991).
[34] Y. Saito, K. Tashiro, I. Koiwa, and H. Honma, *J. Japan Institute of Electronics Packaging*, 10, 62 (2007).
[35] T. Homma, T. Osaka, and H. Sato, *Hyomenkagaku*, 22, 350 (2001).
[36] T. Homma, H. Asai, T. Osaka, K. Takei, and Y. Maeda, *Chem. Lett.*, 17, 83 (1992).
[37] J. Kawaji, F. Kitaizumi, H. Oikawa, D. Niwa, T. Homma, and T. Osaka, *J. Magn. Magn. Mater.*, 287, 245 (2005).
[38] T. Ouchi, N. Shimano, and T. Homma, *Electrochim. Acta,* 56, 9575 (2011).
[39] G. O. Mallory, and J. B. Hajdu, *American Electroplaters and Surface Finishers Society*, Orland, (1990).
[40] H. Narcus, *Metal Finishing*, 45, 64 (1947).
[41] S. Wein, *Metal Finishing*, 46, 58 (1948).
[42] A. E. Cahill, *Proc. Am. Electroplat. Soc.*, 44, 130 (1957).
[43] Z. Wang, O. Yaegashi, H. Sakaue, T. Takahagi, and S. Shingubara, *J. Electrochem. Soc.*, 151, C781 (2004).
[44] M. Sone, K. Kobayakawa, M. Saitou, and Y. Sato, *Electrochim. Acta*, 49, 233 (2004).
[45] T. Fujinami, *J. Surface Finish. Soc. Jpn.*, 48, 387 (1997).
[46] F. Pearlstein, and R. F. Weightman, *Plating*, 60, 474 (1973).
[47] H. Honma, M. Komatsu, and T. Fujinami, *J. Surface Finish. Soc. Jpn.*, 42, 913 (1991).
[48] A. Hung, *Plat. Surf. Finish.*, 75, 62 (1998).
[49] A. Vaskelis, E. Norkus, J. Jaciauskiene, and J. Reclaitis, *Galvanotechnik*, 90, 1556 (1999).
[50] J. Li, and P. A. Kohl, *J. Electrochem. Soc.*, 149, C631 (2002).

[51] A. Brenner, *Met. Finish.*, 52, 61 (1954).
[52] C. R. K. Rao, and D. C. Trivedi, *Coord. Chem. Rev.*, 249, 613 (2005).
[53] L. M. Abrantes, and J. P. Correia, *J. Electrochem. Soc.*, 141, 2356 (1994).
[54] B. Popov, *Plat. Surf. Finish.*, 91, 40 (2004).
[55] R. Johnstone, A. Wilby, and I. Endtwistle, *Chem. Rev.*, 85, 129 (1995).
[56] L. M. Abrantes, A. Bewick, M. Kalaji, and M. C. Oliveira, *J. Chem. Soc. Faraday Trans.*, 92, 4663 (1996).
[57] L. M. Abrantes, and M. C. Oliveira, *J. Electrochem. Soc.*, 147, 2981 (2000).
[58] L. M. Abrantes, E. Vieil, and M. C. Oliveira, *Electrochim. Acta*, 41, 1515 (1996).
[59] Y. Zeng, and S. Zhou, *J. Electroanal. Chem.*, 79, 469 (1999).
[60] Y. Zeng, and S. Zhou, *Electrochem. Commun.*, 1, 217 (1999).
[61] M. Kunimoto, T. Shimada, S. Odagiril, H. Nakai, and T. Homma, *J. Electrochem. Soc.*, 158, D585 (2011).
[62] T. Shimada, A. Tamaki, H. Nakai, and T. Homma, *Electrochemistry*, 75, 45 (2007).
[63] T. Curtius, *J. Prakt. Chem*., 39, 107 (1889).
[64] T. Adams, and R. Brown, *Org. Synth.; Coll.*, 1, 309 (1941).
[65] J. E. A. M. van den Meerakker, *J. Appl. Electrochem.*, 11, 395 (1981).
[66] J. A. Harrison, and Z. A. Khan, *J. Electroanal. Chem.*, 26, 1 (1970).
[67] A. Butlerov, *Annalen der Chemie und Pharmacie*, 111, 242 (1859).
[68] A. W. Horfmann, *Journal für praktische Chemie*, 107, 414 (1869).
[69] T. Shimada, K. Sakata, T. Homma, H. Nakai, and T. Osaka, *Electrochim. Acta*, 51, 906 (2005).
[70] T. Shimada, H. Nakai, and T. Homma, *J. Electrochem. Soc.*, 154, D273 (2007).
[71] Z. M. Hu, K. Takahashi, and H. Nakatsuji, *Surface Sci.*, 442, 90 (1999).
[72] X. Yin, L. Hong, and B. H. Chen, *J. Phys. Chem. B*, 108, 10919 (2004).
[73] M. Kunimoto, K. Endo, H. Nakai, and T. Homma, *Electrochim. Acta*, 100, 311 (2013).
[74] S. Miertus, and J. Tomasi, *Chem. Phys.*, 65, 239 (1982).
[75] J. B. Foresman, T. A. Keith, K. B. Wiberg, J. Snoonian, and M. J. Frisch, *J. Phys. Chem.*, 100, 16098 (1996).
[76] T. Homma, I. Komatsu, A. Tamaki, H. Nakai, and T. Osaka, *Electrochim. Acta*, 47, 47 (2001).
[77] H. Nakai, T. Homma, I. Komatsu, and T. Osaka, *J. Phys. Chem. B*, 105, 1701 (2001).
[78] H. Hirohata, M. Oita, and K. Honjo, *J. Met. Finish. Soc. Jpn.*, 21, 485 (1970).
[79] A. Molenaar, J. Meerakker, and J. Boven, *Plating*, 61, 649 (1974).

[80] M. Saito, and H. Houma, *Met. Surf. Technol. Jpn.*, 29, 88 (1978).
[81] J. S. Sallo, J. Kivel, and F. C. Albers, *J. Electrochem. Soc.*, 110, 890 (1963).
[82] W. H. Bragg, *Phil. Mag.*, 23, 647 (1912).
[83] B. Marvin, and J. J. Garbarino, *J. Crim. L.*, 4, 44 (1954).
[84] C. G. Shull, *Phys. Rev.*, 76, 8 (1949).
[85] A. Campion, and P. Kambhampati, *Chem. Soc. Rev.*, 27, 241 (1998).
[86] M. Moskovits, *J. Raman Spectrosc.*, 36, 485 (2005).
[87] K. Kneipp, H. Kneipp, I. Itzkan, R. R. Dasari, and M. S. Feld, *Chem. Rev.*, 99, 2957 (1999).
[88] K. C. Grabar, R. G. Freeman, M. B. Hommer, and M. J. Natan, *Anal. Chem*., 67, 735 (1995).
[89] M. E. Stewart, C. R. Anderton, L. B. Thompson, J. Maria, S. K. Gray, J. A. Rogers, and R. G. Nuzzo, *Chem. Rev.*, 108, 494 (2008).
[90] Z. Q. Tian, B. Ren, and D. Y. Wu, *J. Phys. Chem.*, 106, 9464 (2002).
[91] J. Jiang, K. Bosnick, M. Maillard, and L. Brus, *J. Phys. Chem. B*, 107, 9964 (2003).
[92] A. D. McFarland, M. A. Young, J. A. Dieringer, and R. P. V. Duyne, *J. Phys. Chem. B*, 109, 11279 (2005).
[93] C. E. Talley, J. B. Jackson, C. Oubre, N. K. Grady, C. W. Hollars, S. M. Lane, T. R. Huser, R. Nordlander, and N. J. Halas, *Nano Lett.*, 5, 1569 (2005).
[94] S. S. Xiao, N. A. Mortensen, and A. P. Jauho, *J. Eur. Opt. Soc.*, 3, 08022 (2008).
[95] A. Smekal, *Naturwissenshaften*, 43, 873 (1923).
[96] C. V. Raman, and K. S. Krishman, *Nature*, 121, 169 (1928).
[97] M. Fleischmann, P. J. Hendra, and A. J. McQuillan, *Chem, Phys. Lett.*, 26, 163 (1974).
[98] U. K. Sur, *Resonance*, 2, 154 (2010).
[99] W. Xu, N. Mao, and J. Zhang, *Small*, 8, 1206 (2013).
[100] K. Kneipp, Y. Wang, H. Kneipp, L. T. Perelman, I. Itzkan, R. Dasari, and M. S. Feld, *Phys. Rev. Lett.*, 78, 1667 (1997).
[101] P. Kambhampati, C. M. Child, M. C. Foster, and A. Campion, *J. Chem. Phys.*, 108, 5013 (1998).
[102] M. J. Weaver, S. Zou, and H. Y. H. Chan, *Anal. Chem.*, 72, 38A (2000).
[103] Z. Q. Tian, and B. Ren, *Raman Spectroscopy of Electrode Surfaces, Encyclopedia of Electrochemistry,* Wiley & VCH, 3, 575 (2003).
[104] V. D. Tuan, *Trends in Anal. Chem.,* 17, 558 (1998).
[105] Z. Q. Tian, Internet J. Vib. Spectrosc., [www.ijvs.com], 4, 2 (2000).

[106] W. Q. Zhu, M. G. Banaee, D. X. Wang, Y. Z. Chu, and K. B. Crozier, *Small*, 13, 1761 (2011).
[107] H. H. Wang, C. Y. Liu, S. B. Wu, N. W. Liu, C. Y. Peng, T. H. Chan, C. F. Hsu, J. K. Wang, and Y. L. Wang, *Adv. Mater.*, 18, 491 (2006).
[108] S. A. Maier, and H. A. Atwater, *J. Appl. Phys.*, 98, 1 (2005).
[109] E. Hao, and G. C. Schatz, *J. Chem. Phys.*, 120, 357 (2004).
[110] G. B. Mohamad, and B. C. Kenneth, *ACS Nano.*, 5, 307 (2011).
[111] Y. Z. Chou, G. B. Mohamad, and B. C. Kenneth, *ACS Nano.*, 4, 2084 (2010).
[112] M. Yanagisawa, M. Shimamoto, T. Naknishi, M. Saito, and T. Osaka, *Electrochem. Soc. Trans.*, 16, 397 (2008).
[113] J. B. Foresman, and A. E, Frisch, *Exploring Chemistry with Electronic Structure Methods*, Gaussian Inc., (1996).
[114] A. Szabo, and N. S. Ostlund, *Modern Quantum Chemistry: Introduction to Advanced Electronic Structure Theory*, Dover Publications, (1989).
[115] K. Burke, *J. Chem. Phys.*, 136, 150901 (2012).
[116] P. Hohenberg, and W. Kohn, *Phys. Rev.*, 136, B864 (1964).
[117] W. Kohn, and L. J. Sham, *Phys. Rev.*, 140, A1133 (1965).
[118] A. D. Becke, *Phys. Rev. A*, 38, 3098 (1988).
[119] C. Lee, W. Yang, and R. G. Parr, *Phys. Rev. B*, 37, 785 (1988).
[120] A. D. Becke, *J. Chem. Phys.*, 98, 5648 (1993).
[121] M. Kunimoto, H. Nakai, and T. Homma, *J. Electrochem. Soc.*, 158, D626 (2011).
[122] N. Metropolis, A. W. Rosenbluth, M. N. Rosenbluth, A. M. Teller, and E. Teller, *J. Chem. Phys.*, 21, 1087 (1953).

Chapter 2:

Characterization of reductants at metal surfaces using SERS and DFT

2.1 Introduction

In order to further control of the solid-liquid interface in electroless deposition process and precise selection of substrate and reductants for the fabrication of functionalized substructures, the characterization of reductants adsorption on metal surfaces should be clarified, which can provide molecular level information for understanding the reaction mechanism of electroless deposition process. Although a few studies attempted to model the characterization of reductants on metal surfaces [1-5], they have no the overall views from experimental and theoretical perspectives.

To consider this issue, this chapter characterizes the behaviors of reductants adsorption on metal surfaces as follows.

The experimental method (Surface Enhanced Raman Spectroscopy, SERS) [6-9] is applicable for characterizing reductants adsorption on metal surfaces with high-selectivity component at right angle down to sub-monolayer level using a surface enhanced Raman antenna, which can define the location and structure of adsorbed reductants just only at 1-2 nm from the antenna surface. The plasmon antenna with concentric pattern is designed by using FDTD calculation to enhance the Raman scattering on the surface of Ag, Au, and Cu. Yanagisawa et al. have demonstrated the sub-nanoscale detection of self-assembled monolayer (SAM) on the Ag antenna [10]. The schematic diagram of the antenna is shown in Figure 2.1.1. The Raman scattering is further enhanced on this antenna by the laser from the perpendicular direction to the surface. Therefore it is easy to realize in-situ measurements. Furthermore, the electric field has a well-defined, rapidly-decaying intensity as a function of radial distance from the center of the antenna. This well-defined functional form of the electric field allows us to relate the strength of the Raman signal we detect with the location of the detected molecule. In order to utilize this precipitous electric field, we have applied piezo stage to realize the step by step measurement in changing the distance from the antenna with 1 nm/step.

Meanwhile, the theoretical method (Density Functional Theory, DFT) [11-13] can provide molecular level, basic level information for understanding the mechanism according to the chemical characteristics. In the DFT calculation, the metal surface can be modeled as a cluster whose size is sufficient to express the reaction field of some adsorbates. Although it is much smaller, such a model is known to provide sufficient results for analysis of adsorption behavior [14,15]. The solvent can be modeled as the dielectric material using polarized continuum model (PCM) [16]. Because PCM is

insufficient for modeling the solid-liquid interface, which cannot construct gradually changing constant dielectric field, this chapter considers solvent molecules on the metal surfaces.

The objective of this study in this chapter is to investigate the structure and the bonding of adsorbed reductants on metal surfaces, using experimental and theoretical methodologies shown above. To achieve this objective, this study characterizes three reductants hydrazine, hypophosphite ion, and formaldehyde on the Ag surface and analyzes the adsorption state of the formaldehyde on the Cu surface.

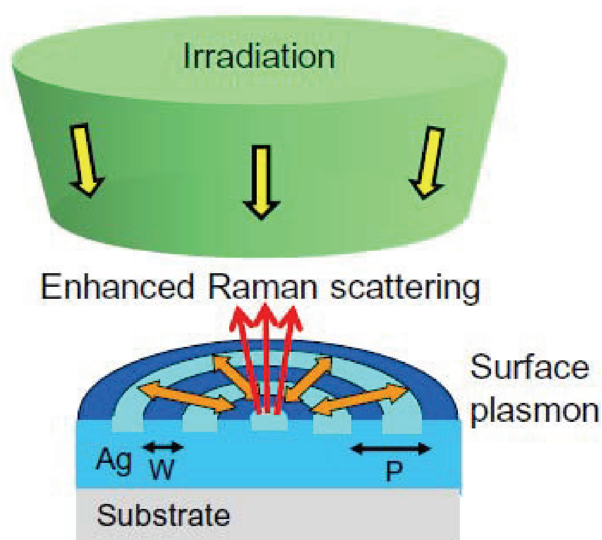

Fig. 2.1.1 Schematic diagram of plasmon antenna [10].

2.2 Methodology

In this study, it is important to propose the method for characterizing the behaviors of reductants adsorption on metal surfaces. The characterization of reductants on metal surfaces can provide some fundamental knowledge for understanding the reaction mechanism of electroless deposition process; and the overall views could be complicated. To solve this problem, reductants adsorption on metal surfaces was initially characterized by using a surface enhanced Raman antenna. Then, the bonding and structure of adsorbed reductants on metal surfaces were calculated by DFT calculation, which can provide molecular level, basic level information according to the chemical characteristics.

The information of the surface enhanced Raman antenna is shown below. The structure of plasmon antenna was designed as the concentric pattern which consists of six lines and spaces with a pitch of 550 nm and a center dimple with a diameter of 250 nm for enhancing Raman scattering effectively on metal surfaces by using Finite-Difference Time-Domain (FDTD) calculation based on Yanagisawa et al. [10]. The electric field was calculated with the FDTD solver (Fullwave) provided by RSoft Design Group, Inc. The three dimensional simulated area including the antenna was $10\mu m\times10\mu m\times0.5\mu m$ in which the mesh size was 10 nm. The electric field was assumed to be polarized along the x-axis where the propagation direction of the plain wave (532.2 nm and 632.8 nm wavelength) was along the z-axis. Refractory indices were 0.0543+3.4291i for 532.3 nm wavelength on Ag and 1.27 +3.41i for 632.8 nm wavelength on Cu in the FDTD calculation.

The fabrication processes of the surface enhanced Raman antenna is shown below. The concentric pattern was formed on a Si substrate by using electron beam (EB) lithography and UV-nanoimprint lithography (Kyodo-international). Then Ag (23) or fcc-Cu (111) layer with 100 nm thickness was sputter deposited on the concentric pattern. The schematic illustration of process steps for the fabrication of metal plasmon antenna was shown in Figure 2.2.1.

A 0.5-μL aliquot of hydrazine ($H_2NNH_2\cdot H_2O$, Kanto Chemical Co., Inc.), hypophosphite ($NaPH_2O_2\cdot H_2O$, Kanto Chemical Co., Inc.), formaldehyde (HCHO, Kanto Chemical Co., Inc.), or a mixture of hydrazine and hypophosphite, each at concentration of 100 mM, as summarized in Table 2.2.1, was placed on the antenna surface. The solutions with antenna were then measured using a Raman microspectroscopy device (Nanofinder 30, Tokyo Instruments, Inc.) equipped with a

confocal microscope. The condition of Raman spectroscopy is shown in Table 2.2.2. The 532.2 nm and 632.8 nm line from a He-Ne laser was used for the excitation of Raman scattering. The laser beam was focused onto spot around 1μm in diameter through an objective lens at a magnification of 100 × with NA (0.9). The data acquisition time was 1.0 s. The wavenumber resolution was 2.4 cm^{-1} when the grating (600 grooves/mm) was used, and the wavenumber range was 50 cm^{-1} - 4000 cm^{-1}. The laser power irradiated on the sample surface was 3 mW. Bath temperature and pH were 50 ^{o}C and 8.6.

Figure 2.2.2 shows the schematic model of the antenna and calculation results of electric field on the Cu antenna. Fig. 2.2.2 (a) is the schematic diagram of the antenna, which is composed of coaxial dimples structure on the Si substrate. Meanwhile, Cu is deposited on the Si substrate in Fig. 2.2.2 (a). Comparing Fig. 2.2.2 (a) and (b), the concentric structure enhanced the electric field at the top edge of center part of the antenna. The electric field |E| was attenuated progressively with distance from the surface of Cu plasmon antenna to the solution as shown in Fig. 2.2.2 (c). The SERS enhancement factor is proportional to the fourth power of the electric field, as shown below:

$$I = a\,|E|^4 \tag{1}$$

I is Raman intensity; |E| is intensity of electric field. With these results, the Raman spectra of the target molecules were enhanced only at the surface of the antenna. Therefore the strongest spectrum was defined as information of the molecules just on the plasmon antenna.

Since the electric field |E| has a well-defined, rapidly-decaying intensity as a function of radial distance from the center of the antenna, this well-defined functional form of the electric field allows us to relate the strength of the Raman signal we detect with the location of the detected molecule. Moreover, the enhanced area of plasmon antenna was around 50 nm where a localized plasmon was generated according to FDTD calculation, as shown in Figure 2.2.3. In addition, the surface roughness was within the 1 nm in the enhanced area, where could enhance the Raman scattering at right angle. In order to utilize this precipitous electric field and enhance area, therefore, we changed the focus of measurement precisely with 1 nm step by using a piezometer stage, which could allow us to take measurements at varying distances from the antenna with 1 nm/step. The schematic illustration of the Raman spectroscopy with Z moving stage is shown in Figure 2.2.4.

The conditions of the DFT calculations are shown below. All calculations were performed using the B3LYP functional as implemented in the Gaussian 03 package [17], which was a combination of Becke's three-parameter hybrid exchange functional (B3) [18] and the Lee-Yang-Parr correlation functional (LYP) [19]. The Gaussian Basis sets were P, C, H/6-31G** [20] and O, N/6-31 +G** [21]. For Cu, Ar core was replaced by an effective core potential by Hay and Wadt [22]. Valence electrons were represented by a (5s5p4d)/[3s3p2d] basis set. The solvation effect was taken into account by the self-consistent reaction field method with an isodensity surface polarized continuum model (SCRF-IPCM) [16], which used dielectric constant 80.0 [-].

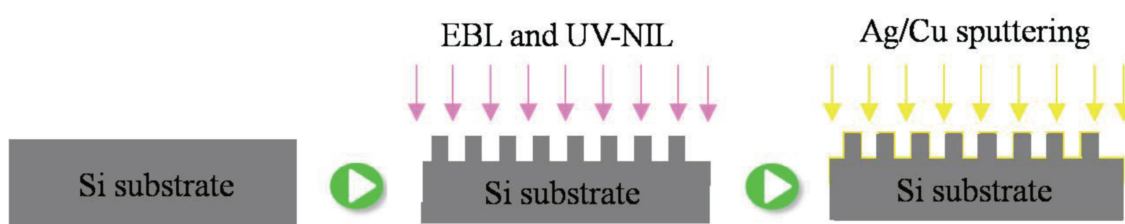

Fig. 2.2.1 Schematic illustration of process steps for the fabrication of metal plasmon antenna.

Table 2.2.1 Experimental conditions of reductant solutions.

Chemicals	**Concentration (mM)**			
	(a)	**(b)**	**(c)**	**(d)**
$H_2NNH_2{\cdot}H_2O$	100	-	-	100
$NaH_2PO_2{\cdot}H_2O$	-	100	-	100
HCHO	-	-	100	-

Table 2.2.2 Experimental condition of Raman spectroscopy.

Nanofinder - 30	
Exposure time	30s
Wave length (He/Ne Laser)	532/633 nm
Measuring range	0-4000 cm^{-1}
Resolution	XY: 2 nm, Z: 1 nm

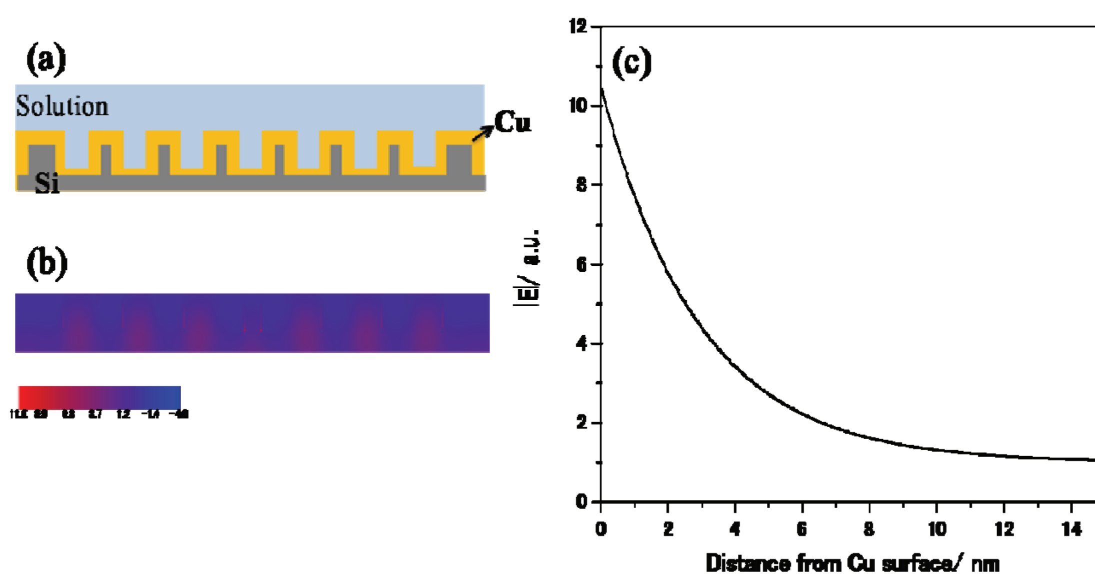

Fig. 2.2.2 The schematic model of plasmon antenna (a); Calculated values of electric field on the plasmon antenna (b, c).

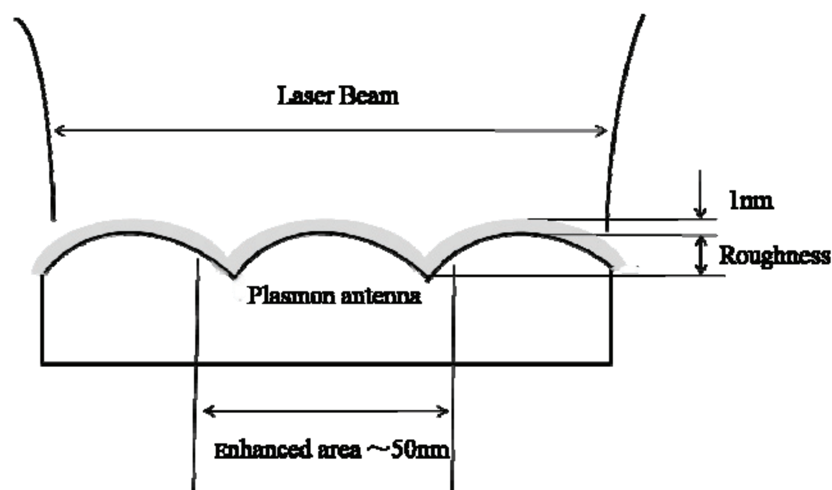

Fig. 2.2.3 Surface topography of plasmon antenna.

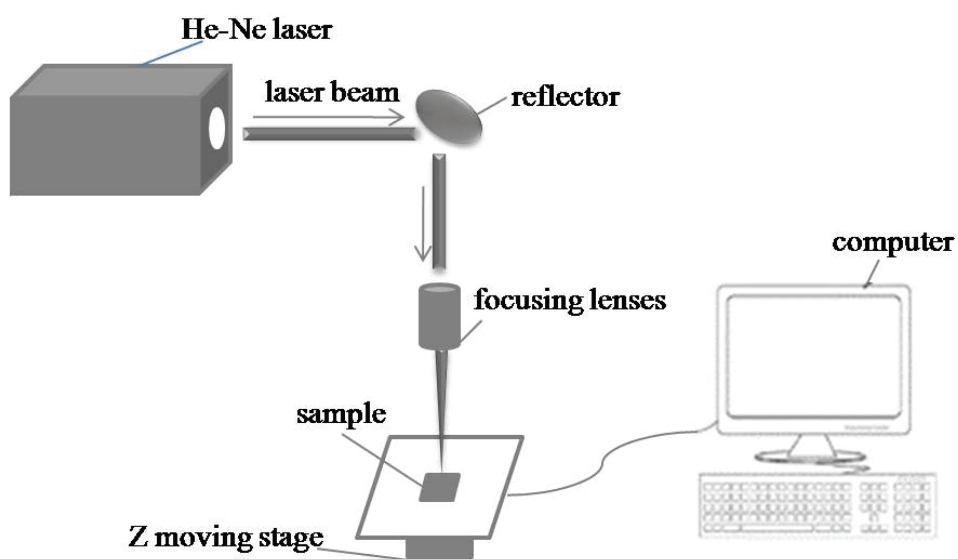

Fig. 2.2.4 Schematic illustration of the Raman spectroscopy with Z moving stage.

2.3 Results and Discussion

2.3.1 SERS of reductants

To obtain the bonding and structure of adsorbed reductants on metal surfaces, the characterization of reductants (not in contact with the antenna) was analyzed by Raman spectroscopy and DFT calculation above all.

Table 2.3.1 and Figure 2.3.1 show the theoretical Raman spectrum calculated by using DFT and experimental Raman spectra of the reductant solutions. A Raman spectrum of reductants was given as Fig. 2.3.1. Corresponding to the theoretical Raman spectrum of reductants in Table 2.3.1, All Characteristic peaks of reductants were found as follows:

1. Solid line (a) showed the Raman spectrum of N_2H_4 which had six pronounced, polarized lines at 469, 796/924, 1132, 1303/1366, 1633 (overlapping Raman band), and 3293 (3213, 3356) cm^{-1}. We assigned these lines to the NH_2 torsional (vertical), NH_2 bending (out of plane), NN stretching, NH_2 torsional (horizontal), NH_2 bending (in plane), and NH stretching, respectively, by comparing them with the theoretical Raman spectrum of hydrazine.

2. Dash line (b) showed the Raman spectrum of NaH_2PO_2 which had six pronounced, polarized lines at 466, 776, 921, 1060/1197, 1136 (overlapping Raman band), and 2368 cm^{-1} (overlapping Raman band). These lines were assigned to the OPO bending (in plane), HPH torsional (vertical), HPH torsional (horizontal), PO stretching, HPH bending (out of plane) or HPH bending (in plane), and PH stretching, respectively, by comparing them with the theoretical Raman spectrum of hypophosphite ion.

3. Dot line (c) showed the Raman spectrum of HCHO which had eight pronounced, polarized lines at 458, 776/1386, 984, 1122, 1296, 1426, 1613, and 2350 cm^{-1}(overlapping Raman band). We also had assigned these lines to the OCO bending, CO stretching, COH bending, CH_2 torsional (horizontal), CH_2 torsional (vertical), HCH bending (out of plane), HCH bending (in plane), and CH stretching, respectively, by comparing them with the theoretical Raman spectrum of formaldehyde.

4. Dash dot line (d) showed the Raman spectrum of mixture (N_2H_4 and NaH_2PO_2) which had mixing pronounced as same as polarized lines of hydrazine and hypophosphite ion.

Overlapping Raman bands were observed in Raman spectra, and three possible explanations for the phenomenon were as follows: 1. Peaks reflect the average vibration

of many molecules in the experimental Raman spectra, while DFT only calculate one molecule; 2. The grating of Raman spectroscopy is very suitable for getting good peak strength, but it is not fit for detecting the very close peaks in this study; 3. Raman laser with high energy can move chemical molecules by moving laser focus position on molecules. Therefore, some chemical bonds, which have similar peaks and intensities, can be influenced by these factors; and they are observed as overlapping Raman bands.

From these results, the characteristic peaks of reductants were revealed. They were applied to define the bonding of reductants on Ag/Cu surface as basic information.

Table 2.3.1 The DFT calculation of reductants.

Vibrational mode	**Wavenumber (cm^{-1})**
NH_2 torsional(vertical)	467.3
NH_2 bending(out of plane)	798.1,953.1
NN stretching	1119.2
NH_2 torsional(horizontal)	1292.6,1321.9
NH_2 bending (in plane)	1680.9,1698.7
NH stretching	3469.0,3475.8,3585.7,3590.4
OPO bending (in plane)	437.8
HPH torsional(vertical)	795.2
HPH torsional(horizontal)	920.1
PO stretching	1023.3,1218.2
HPH bending(out of plane)	1112.4
HPH bending(in plane)	1176.8
PH stretching	2236.3,2176.6
COH bending	76.8,1068.1
OCO bending	424.8
CO stretching	664.5,1362.1
CH_2 torsional (horizontal)	1097.4
CH_2 torsional (vertical)	1233.3
HCH bending(out of plane)	1388.2
HCH bending(in plane)	1536.7
CH stretching	2494.8,2595.8

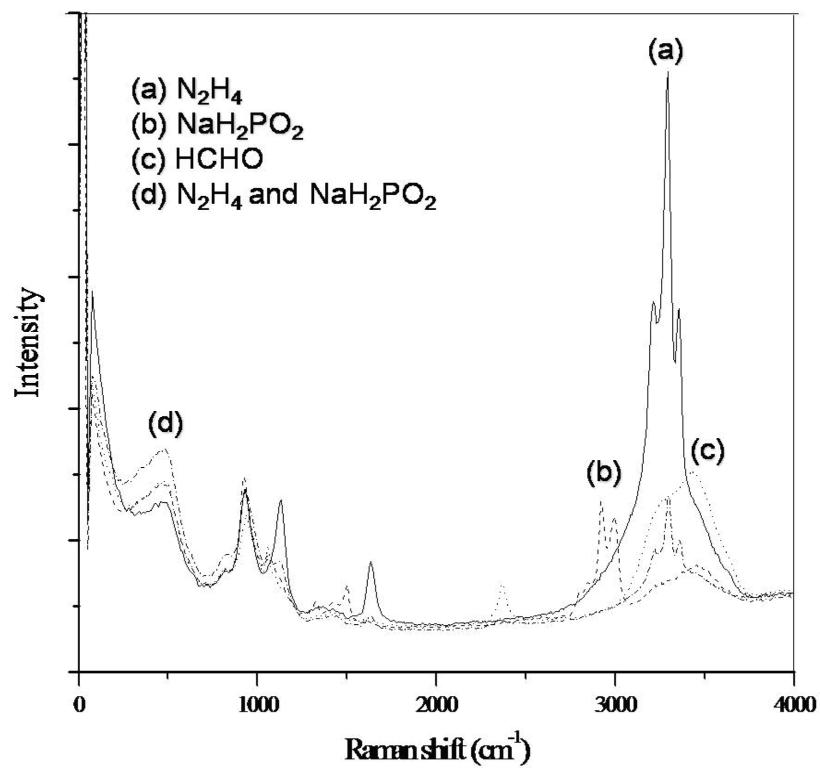

Fig. 2.3.1 Raman spectra of reductant solutions.

2.3.2 SERS of reductants on a Ag surface

Then, we attempted to drop the reductants solution on a Ag plasmon antenna to describe the characterization of reductants adsorption on the Ag surface. The information of the Ag antenna is shown below. First, Figure 2.3.2 shows the SEM image of surface enhanced Raman antenna (Ag). As described above, the pattern of the Ag antenna was fabricated by electron beam (EB) lithography and UV-nanoimprint lithography; then Ag (23) layer with 100 nm thickness was sputter deposited on the concentric pattern. Because the structure of the antenna was designed for efficiently enhancing of Raman scattering on Ag by FDTD calculation based on Yanagisawa's proposal for that of on Ag, the SERS effect of deposited Ag is much higher than other metals, as shown in Figure 2.3.3 [10]. In the figure, it can be seen that they have checked the dielectric constants of several metals and found that the best is Ag. Moreover, they discovered that the calculated electric field |E| at the center of plasmon antenna could be increased by 2000 times using the Ag surface with optimized pitch and the plasmon wave length for the wavelength of the excitation laser (532.2 nm).

Therefore, we attempted to investigate the function of the plasmon antenna by focusing on the adsorbed reductants on Ag antenna by using Raman spectroscopy. The schematic illustration of reductants on the Ag plasmon antenna is shown in Figure 2.3.4.

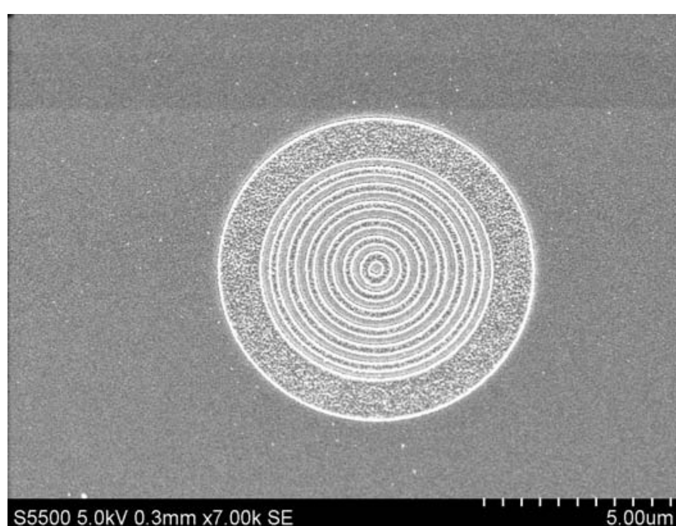

Fig. 2.3.2 SEM image of Ag plasmon antenna.

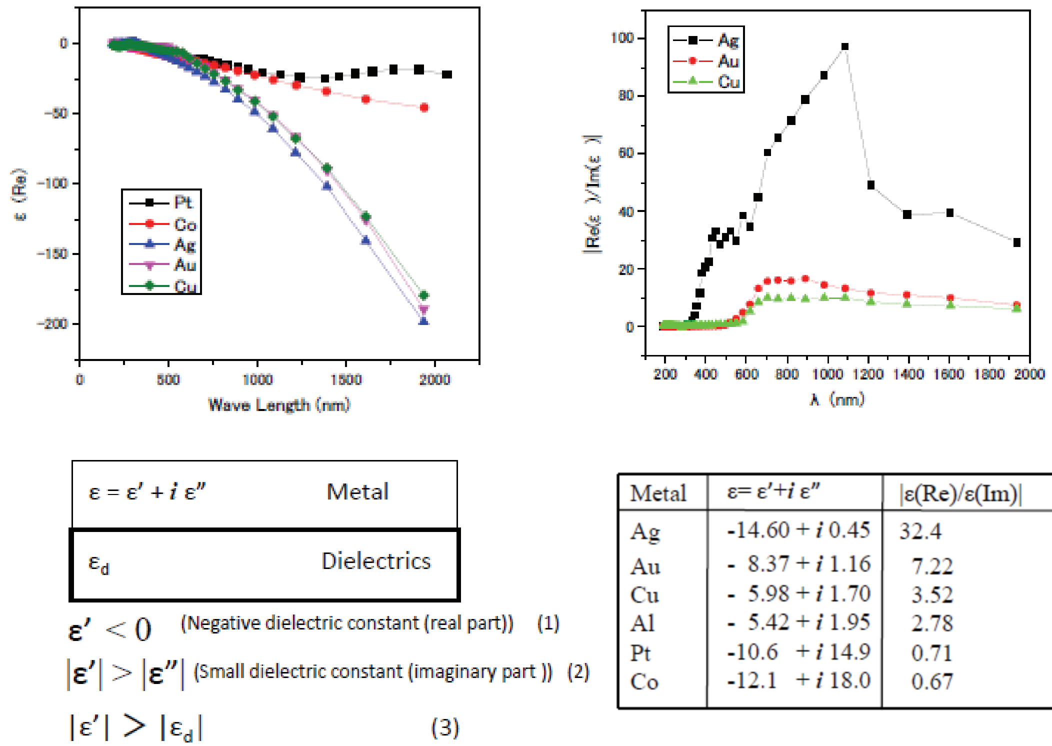

Metal	ε= ε′+*i* ε″	|ε(Re)/ε(Im)|
Ag	-14.60 + *i* 0.45	32.4
Au	- 8.37 + *i* 1.16	7.22
Cu	- 5.98 + *i* 1.70	3.52
Al	- 5.42 + *i* 1.95	2.78
Pt	-10.6 + *i* 14.9	0.71
Co	-12.1 + *i* 18.0	0.67

Fig. 2.3.3 Dielectric constants of metals (λ=600 nm) [10].

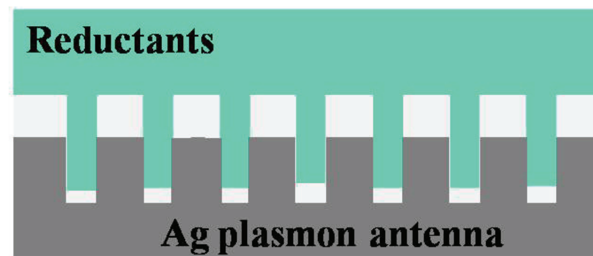

Fig. 2.3.4 Schematic illustration of reductants on Ag plasmon antenna.

As a next step, the adsorption behaviors of reductants on the Ag antenna were characterized by Raman spectroscopy. Figure 2.3.5 shows the experimental Raman spectra of the reductant solutions on the Ag antenna. In the figure, Raman spectrum of adsorbed hydrazine on Ag (a); adsorbed hypophosphite ions on Ag (b); adsorbed formaldehyde on Ag (c); adsorbed mixture of hydrazine and hypophosphite ions on Ag (d); and only Ag antenna were given. By comparing with the Raman spectra of only reductant solutions (not in contact with the antenna), extra Raman shifts at 360 cm^{-1} were observed in Fig. 2.3.5. Because these Raman peaks were observed only after the reductants were dropped on the Ag antenna, while there were no these peaks in the Raman spectra of only reductant solutions. Therefore, we defined this wavenumber domain as Ag-reductants bonding. Moreover, there were other lines of undetermined scattered radiation which we had assigned tentatively to the characteristic peaks of reductants. Since the surface enhanced Raman antenna can provide the characterization of reductants adsorption on metal surfaces down to sub-monolayer level, we then attempted to use Raman spectroscopy and DFT calculation to define the bonding and structure of adsorbed reductants on the Cu surface to understand the reaction mechanism of electroless deposition.

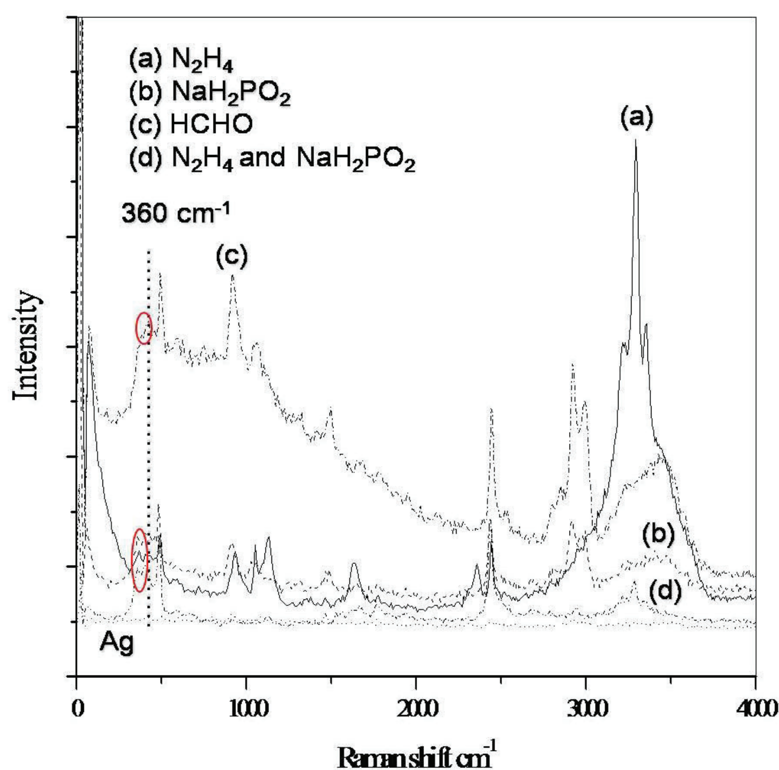

Fig. 2.3.5 Raman spectra of reductants on the Ag antenna.

2.3.3 SERS and DFT of formaldehyde on a Cu surface

In previous studies on the reaction mechanism of formaldehyde, Shimada et al. investigated the adsorption and oxidation process of formaldehyde on the Ag surface [4]. However, their theoretical results have not been identified by experiments and the most stable configure of formaldehyde adsorption on metal surface has not been proposed. To clarify them and understand the reaction mechanism of electroless deposition, a Cu deposited surface enhanced antenna was made to analyze the bonging and structure of formaldehyde on the Cu surface, which can determine the reaction behaviors of the formaldehyde. Information of the Cu antenna is shown below. First, Figure 2.3.6 shows the SEM image of surface enhanced Raman antenna (Cu). The process steps for fabrication of the Cu antenna are shown above. The structure of the antenna was designed by FDTD calculation based on Yanagisawa's proposal for that of on Ag. The SERS effect of deposited Cu was less than deposited Ag. As the result of dielectric constant, for the ratio of real part to imaginary part of the complex dielectric constant (|ε (Re)/ε (Im)|), Ag was 32.4 more than 3.52, which was the ratio of Cu as shown in Fig. 2.3.3. However, calculated electric field |E| at the center of plasmon antenna could be increased by 14% by using the antenna with optimized pitch and corresponding the plasmon wave length for the wavelength of the excitation laser (632.8 nm). Estimated Raman intensity could also increased by 69% because the reduced Raman intensity, which is proportional to the fourth power of |E|. Hence, the Cu antenna also can induce the Raman enhancement effect. Then, we attempted to investigate the characterization of formaldehyde on the Cu antenna by using Raman spectroscopy and DFT calculation.

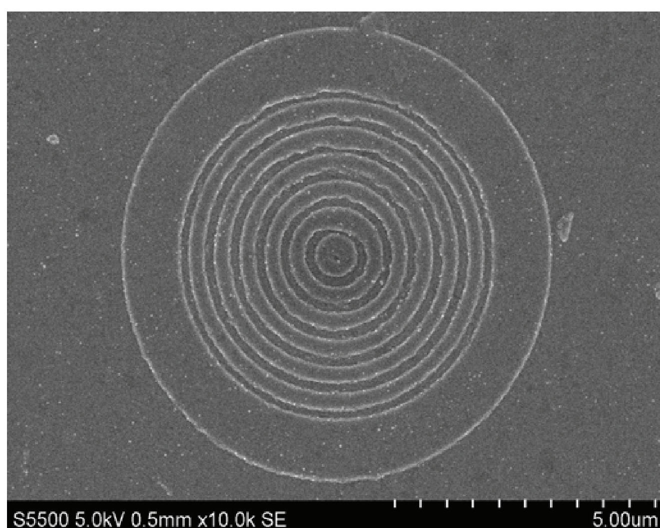

Fig. 2.3.6 SEM image of Cu plasmon antenna.

Next, the adsorption behaviors of formaldehyde on the Cu antenna were investigated by Raman spectroscopy and DFT. Table 2.3.2 and Figure 2.3.7 show the theoretical Raman spectrum calculated by using DFT and experimental Raman spectra of formaldehyde on the Cu antenna. Because of the device which is coupled with a piezo stage, the top-line and bottom line were defined as Raman scattering of formaldehyde solution and Cu antenna, and the intermediate lines could be considered as Raman scattering of formaldehyde on Cu antenna in Fig. 2.3.7. Meanwhile, Cu-O stretching mode on 395.1 cm^{-1} in Table 2.3.2 was also given by DFT calculation. This wavenumber domain is near to that of experimental result of Raman spectroscopy. Thus, the Raman shift at 382 cm^{-1} was defined as Cu-O bond in Fig. 2.3.7. Moreover, there were other lines at 514, 613, 1097 and 1462 cm^{-1} of undetermined scattered radiation which we had assigned to the OCO bending, CO stretching, CH_2 torsional (horizontal), and HCH bending (in plane), respectively. These corresponded to the calculation of formaldehyde adsorption on Cu as shown in Table 2.3.2. From these results, the adsorption model of formaldehyde in electroless deposition was revealed. Furthermore, these peaks were only observed at 1-2 nm from the antenna surface which meant that this method absolutely could to define the bonding of adsorbed formaldehyde just only on the Cu antenna.

Then, we attempted to use DFT calculation to define the structure of adsorbed formaldehyde on Cu.

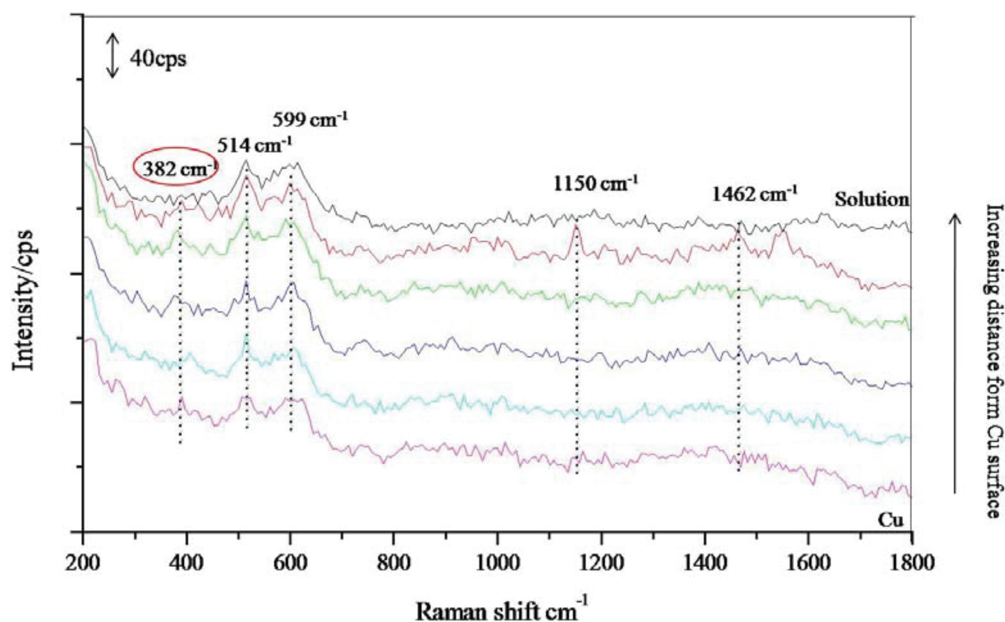

Fig. 2.3.7 Raman spectra of formaldehyde on the Cu antenna.

Table 2.3.2 The theoretical Raman spectra calculation of formaldehyde on Cu by using DFT.

Vibrational mode	Wavenumber (cm^{-1})
Cu-O stretching	395.1
OCO bending	519.8
CO stretching	713.6
CH_2 torsional (horizontal)	1097.1,1124.9
CH_2 torsional (vertical)	1246.6
COH bending	1293.5
HCH bending(out of plane)	1310.9
HCH bending(in plane)	1412.6
CH stretching	2865.6,2908.4
OH stretching	3783.7

In order to elucidate the structure of formaldehyde on the Cu surface, DFT calculation was applied to model the adsorption of formaldehyde on a Cu surface. The conditions of DFT calculation are described above. Figure 2.3.8 shows prospective configuration of formaldehyde on fcc-Cu (111) calculated by DFT. In Fig. 2.3.8, the surface model was the tetrahedral cluster model made up of 20 Cu atoms [23]. Moreover, all parameters of adsorbing system are optimized, including the cluster structure and molecular structure.

Consequently, the most stable conformation of adsorbed formaldehyde on Cu was given as di-σ-bonded conformation by DFT calculation in Fig. 2.3.8. Therefore, the adsorbed bonding and structure of formaldehyde on Cu could be identified by Raman spectroscopy and DFT calculation.

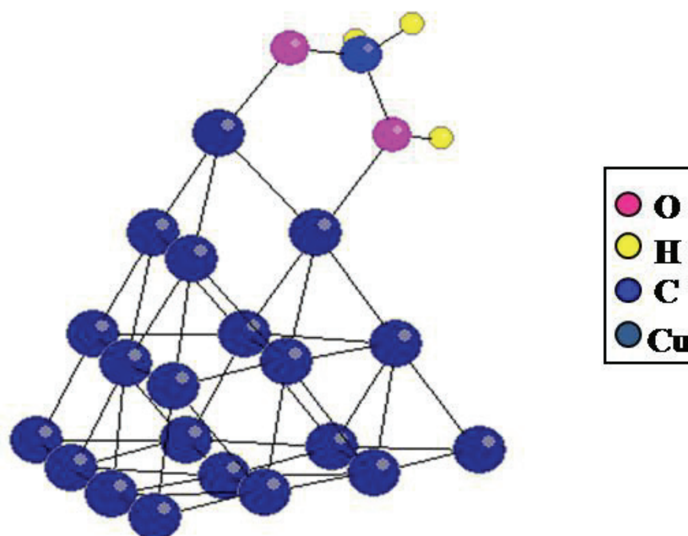

Fig. 2.3.8 The prospective configuration of formaldehyde on Cu (di-σ-bonded conformation).

2.4 Conclusions

In this chapter, an approach for analyzing the characterization of reductants adsorption on metal surfaces using surface enhanced Raman antenna was proposed. By using the antenna and comparison with DFT results, Raman peaks of adsorbed reductants on Ag and Cu were provided, defining as Ag/Cu-reductants bond. Although the dielectric constant of Cu surface is much lower than the dielectric constant of Ag, Cu surface is also able to give efficient SERS effect by using the surface enhanced Raman antenna. Furthermore, the characteristic peaks in the Raman spectra were in good agreement with DFT results.

From the experimental and calculated results, author demonstrated that this method had a possibility to define the structure of adsorbed reductants just only on the plasmon antenna. Meanwhile, the di-σ-bonded conformation of adsorbed formaldehyde on the Cu surface was given by DFT calculation as the most stable configuration.

Moreover, the most important conclusion for the later chapters is that such in-situ characterization approach down to sub-monolayer level is required for analysis of variety of systems at solid-liquid interface such as analysis of catalytic reaction which is one of the most difficult applications. According to this conclusion, this approach proposes an important basis for the analyses of the reaction mechanisms of reductants on metal surfaces in the later chapters.

References

[1] M. Kunimoto, T. Shimada, S. Odagiril, H. Nakai, and T. Homma, *J. Electrochem. Soc.*, 158, D585 (2011).
[2] T. Shimada, A. Tamaki, H. Nakai, and T. Homma, *Electrochemistry*, 75, 45 (2007).
[3] T. Shimada, K. Sakata, T. Homma, H. Nakai, and T. Osaka, *Electrochim. Acta*, 51, 906 (2005).
[4] T. Shimada, H. Nakai, and T. Homma, *J. Electrochem. Soc.*, 154, D273 (2007).
[5] M. Kunimoto, H. Nakai, and T. Homma, *J. Electrochem. Soc.*, 158, D626 (2011).
[6] A. Campion, and P. Kambhampati, *Chem. Soc. Rev.*, 27, 241 (1998).
[7] M. Moskovits, *J. Raman Spectrosc.*, 36, 485 (2005).
[8] K. Kneipp, H. Kneipp, I. Itzkan, R. R. Dasari, and M. S. Feld, *Chem. Rev.*, 99, 2957 (1999).
[9] K. C. Grabar, R. G. Freeman, M. B. Hommer, and M. J. Natan, *Anal. Chem.*, 67, 735 (1995).
[10]M. Yanagisawa, M. Shimamoto, T. Naknishi, M. Saito, and T. Osaka, *Electrochem. Soc. Trans.*, 16, 397 (2008).
[11] K. Burke, *J. Chem. Phys.*, 136, 150901 (2012).
[12] P. Hohenberg, and W. Kohn, *Phys. Rev.*, 136, B864 (1964).
[13] W. Kohn, and L. J. Sham, *Phys. Rev.*, 140, A1133 (1965).
[14] H. Nakatsuji, M. Hada, and T. Yonezawa, *J. Am. Chem. Soc.*, 109, 1902 (1987).
[15] S. P. Walch, J. D. Komadina, and F. B. Prinz, *J. Phys. Chem. B*, 113, 7298 (2009).
[16] J. B. Foresman, T. A. Keith, K. B. Winberg, J. M. Sniinian, and J. Frisch, *J. Phys. Chem.*, 100, 16098 (1996).
[17] M. J. Frisch, G. W. Trucks, H. B. Schlegel, G. E. Scuseria, M. A. Robb, J. R. Cheeseman, J. A. Montgomery, Jr., T. Vreven, K. N. Kudin, J. C. Burant, J. M. Millam, S. S. Iyengar, J. Tomasi, V. Barone, B. Mennucci, M. Cossi, G. Scalmani, N. Rega, G. A. Petersson, H. Nakatsuji, M. Hada, M. Ehara, K. Toyota, R. Fukuda, J. Hasegawa, M. Ishida, T. Nakajima, Y. Honda, O. Kitao, H. Nakai, M. Klene, X. Li, J. E. Knox, H. P. Hratchian, J. B. Cross, V. Bakken, C. Adamo, J. Jaramillo, R. Gomperts, R. E. Stratmann, O. Yazyev, A. J. Austin, R. Cammi, C. Pomelli, J. W. Ochterski, P. Y. Ayala, K. Morokuma, G. A. Voth, P. Salvador, J. J. Dannenberg, V. G. Zakrzewski, S. Dapprich, A. D. Daniels, M. C. Strain, O. Farkas, D. K. Malick, A. D. Rabuck, K. Raghavachari, J. B. Foresman, J. V. Ortiz, Q. Cui, A. G. Baboul, S. Clifford, J. Cioslowski, B. B. Stefanov, G. Liu, A. Liashenko, P. Piskorz, I. Komaromi, R. L.

Martin, D. J. Fox, T. Keith, M. A. Al-Laham, C. Y. Peng, A. Nanayakkara, M. Challacombe, P. M. W. Gill, B. Johnson, W. Chen, M. W. Wong, C. Gonzalez, and J. A. Pople, Gaussian 03, Revision C.02, Gaussian, Inc., Wallingford, CT, (2004).
[18] A. D. Becke, *J. Chem. Phys.*, 98, 5648 (1993).
[19] C. Lee, W. Yang, and R. G. Parr, *Phys. Rev. B*, 37, 785 (1988).
[20] D. E. Woon, and T. H. Dunning Jr., *J. Chem. Phys.*, 98, 1358 (1993).
[21] T. Clark, J. Chandrasekhar, G. W. Spitznagel, and P. v. R. Schleyer, *J. Comput. Chem.*, 4, 294 (1983).
[22] P. J. Hay, and W. R. Wadt, *J. Chem. Phys.*, 82, 299 (1985).
[23] L. Zhao, L. Jensen, and G. C. Schatz, *J. Am. Chem. Soc.*, 128, 2911 (2006).

Chapter 3:

Analysis of hydrazine and hypophosphite ions on a Cu surface using SERS and DFT

3.1 Introduction

To obtain some fundamental knowledge about the reaction mechanism of oxidation of reductants for more precise control of the solid-liquid interface in the electroless deposition process, author attempts to investigate the behaviors of reductants absorbed on a Cu surface with molecular level resolution from experimental and computational points of view in this chapter.

In the electroless deposition process, the activation of oxidation reaction of each reductant depends on the kind of metal surface as described in chapter 1. In other words, some metal surfaces cannot exhibit catalytic activity for a few reductants, such as Cu surface for hypophosphite ions. To apply the non-catalytic surfaces with the reductants such as Cu with hypophosphite ions, a novel electroless deposition bath with dual reductants was applied for the electroless deposition process. However, the reaction mechanism of dual reductants has not been fully elucidated yet. In this chapter, therefore, author is focusing on the characterization of adsorption of reductants like hydrazine and hypophosphite ion on the Cu surface. These reductants are the most widely used in electroless deposition [1-6]. Moreover, T. Ouchi et al. have previously reported [7] on the fcc-Cu (111) underlayer with dual reductants of sodium hydrazine and hypophosphite for fabricating ultra-thin films with high perpendicular magnetic coercivities, as shown in Figure 3.1.1. Due to the deposits should have high crystallinity during the initial deposition stage in their study, an fcc-Cu (111) underlayer with low lattice mismatch (2.3%) compared to that of hcp-Co (0002) was used to achieve CoNiP nanodot arrays with high magnetic properties [8,9]. The problem with the application of the Cu underlayer in electroless deposition of CoNiP was that $H_2PO_2^-$, which was used as a reductant in the general electroless deposition of CoNiP, was not oxidized to work as a reductant on the Cu surface [10-13]. Therefore, in that study, CoNiP nanodot arrays with high magnetic properties were fabricated using an autocatalytic system with dual reductants, $H_2PO_2^-$ and N_2H_4. The mechanism responsible for the enhancement of perpendicular magnetic coercivities has not been clearly established, however. Thus, author has attempted to characterize the reductants adsorption on a Cu surface to obtain fundamental knowledge about the mechanism by applying an experimental methodology (SERS) and a theoretical calculation methodology (DFT) in this chapter.

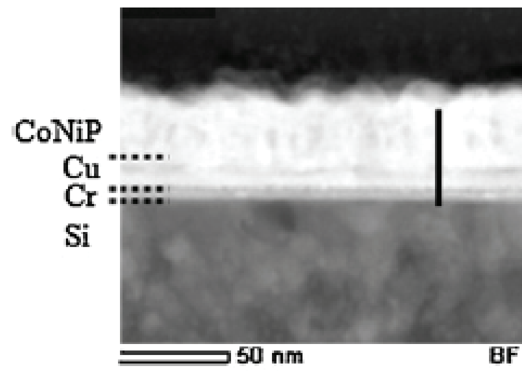

(a)

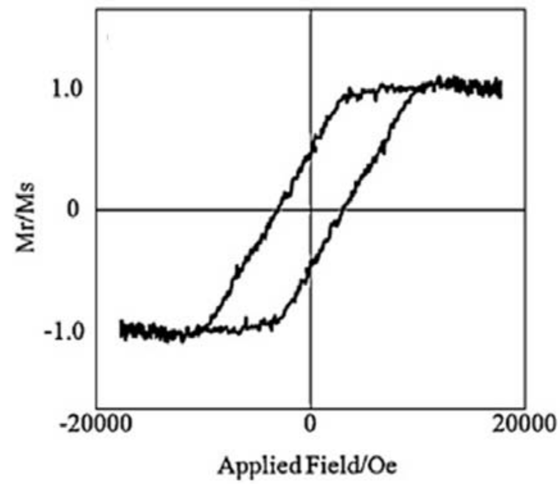

(b)

Fig. 3.1.1 (a) Cross-sectional blight field TEM image of CoNiP film; and (b) perpendicular M-H loop of CoNiP nanodot arrays [7].

3.2 Methodology

In this chapter, the concentric-patterned antenna with coaxial dimples, which consisted of six lines and spaces with a pitch of 550 nm and a center dimple with a diameter of 250 nm, was designed by FDTD calculation to enhance the electric field by focusing surface plasmon, based on Yanagisawa et al. [14]. The three dimensional simulated area was 10μm×10μm×0.5μm in which the mesh size was 10 nm. The electric field calculated with the FDTD solver (Fullwave, provided by RSoft Design Group, Inc.) was polarized along the x-axis where the propagation direction of the plane wave (632.8 nm wavelength) was along the z-axis, as described in the chapter 2.

The fabrication process of the Cu antenna is shown below. First, the concentric pattern of plasmon antenna was formed on a Si substrate by using electron beam (EB) lithography and UV-nanoimprint lithography (Kyodo-International). Then, the fcc-Cu (111) layer with 100 nm thickness was then sputter deposited on the concentric pattern. The SEM image of the plasmon antenna (Cu) was shown in the last chapter.

A 0.5-μL aliquot of hydrazine ($H_2NNH_2{\cdot}H_2O$, Kanto Chemical Co., Inc.), hypophosphite ($NaPH_2O_2{\cdot}H_2O$, Kanto Chemical Co., Inc.), or a mixture of both, each at concentration of 100mM, as summarized in Table 3.2.1, was placed on the antenna surface in the amount of 0.5 μL. The solutions with antenna were then measured by Raman Microspectroscopy (Nanofinder 230, Tokyo Instruments, Inc.) equipped with a confocal microscope. The refractive index was 1.27 + 3.41i for 632.8 nm wavelength on Cu in the FDTD calculation. The 632.8 nm line from a He-Ne laser was used for the excitation of Raman scattering. The laser beam was focused onto a spot around 1μm in diameter through an objective lens at a magnification of 100 × with NA (0.9). In addition, the surface roughness was within 1 nm in the enhanced area, where could enhance the Raman scattering at a right angle which had been discussed in the last chapter. Author had demonstrated that the electric field of the antenna which was weakened progressively with distance from the Cu surface to the solutions; and the nanoscale detection of formaldehyde on the Cu surface by changing the depth (1 nm) of the laser from the perpendicular direction to the surface which meant this approach could define the structure of adsorbed formaldehyde just only on the antenna surface, as shown in the last chapter. In this chapter, however, a piezoelectric motor was used to change the focal depth of measurements by 0.5 nm/step for more precise measurements in this chapter than the 1 nm/step used previously. The data acquisition time was 1.0 s per measurement. The wave number resolution was 2.4 cm^{-1} when the grating (600

grooves/mm) was used. The laser power irradiated on the sample surface was 3 mW.

The conditions of the DFT calculations are shown below. All calculations were performed using the B3LYP functional as implemented in the Gaussian 03 package [15], which was a combination of Becke's three-parameter hybrid exchange functional (B3) [16] and the Lee-Yang-Parr correlation functional (LYP) [17]. The Gaussian Basis sets were P, H/6-31G** [18] and O, N/6-31 +G** [19]. For Cu, Ar core was replaced by an effective core potential by Hay and Wadt [20]. Valence electrons were represented by a (5s5p4d)/[3s3p2d] basis set. The solvation effect was taken into account by the self-consistent reaction field method with an isodensity surface polarized continuum model (SCRF-IPCM) [21], which used dielectric constant 80.0 [-].

Table 3.2.1 Experimental conditions of reductant solutions.

Chemicals	**Concentration (mM)**		
	(a)	**(b)**	**(c)**
$H_2NNH_2 \cdot H_2O$	100	-	100
$NaH_2PO_2 \cdot H_2O$	-	100	100

3.3 Results and Discussion

3.3.1 SERS and DFT of hydrazine and hypophosphite ions

To elucidate the reaction mechanism of electroless deposition by focusing on characterizing the reductants adsorption on a Cu surface, the characterization of reductants were demonstrated by Raman spectroscopy and DFT above all. Table 3.3.1 lists the DFT calculated Raman shifts used for comparison with experimental results. Figure 3.3.1 displays the Raman spectra of the reductant solutions (not in contact with plasmon antenna). Accordingly to the theoretical Raman spectrum of reductants (Table 3.3.1), all characteristic peaks of reductants were observed as follows:

1. Fig. 3.3.1 (a) shows the Raman spectrum of N_2H_4, which has six pronounced, polarized lines at 474, 807/918, 1116, 1296/1346, 1627 (overlapping Raman band), and 3279 (3199, 3334) cm^{-1}. Author assigns these lines to the NH_2 torsional (vertical), NH_2 bending (out of plane), NN stretching, NH_2 torsional (horizontal), NH_2 bending (in plane), and NH stretching, respectively, by comparing them with the theoretical Raman spectrum of hydrazine.

2. Fig. 3.3.1 (b) shows the Raman spectrum of NaH_2PO_2, which has six pronounced, polarized lines at 463, 696, 928, 1054/1209, 1157 (overlapping Raman band), and 2353 cm^{-1} (overlapping Raman band). These lines are assigned to the OPO bending (in plane), HPH torsional (vertical), HPH torsional (horizontal), PO stretching, HPH bending (out of plane) or HPH bending (in plane), and PH stretching, respectively, by comparing them with the theoretical Raman spectrum of hypophosphite ions.

3. Fig. 3.3.1 (c) shows the Raman spectrum of mixture of reductants (100 mM each of N_2H_4 and NaH_2PO_2). Characteristic bands (no overlap) are obvious for both components: a NH_2 bending band at ~1627 cm^{-1} and a PH stretching band at ~2353 cm^{-1}. The two bands in the spectrum of the mixture are completely observed, which means the spectrum of the mixture has all pronounced characteristic bands of N_2H_4 and NaH_2PO_2.

Overlapping Raman bands were observed in Raman spectra, and three possible explanations for the phenomenon were discussed in the chapter 2.

From these results, the characteristic peaks in the Raman spectra of reductants alone were in good agreement with DFT results and could be applied to define the bonding of adsorbed reductants on Cu as basic information.

Table 3.3.1 The DFT calculation of hydrazine and hypophosphite ions.

Vibrational mode	**Wavenumber (cm^{-1})**
NH_2 torsional(vertical)	467.3
NH_2 bending(out of plane)	798.1,953.1
NN stretching	1119.2
NH_2 torsional(horizontal)	1292.6,1321.9
NH_2 bending (in plane)	1680.9,1698.7
NH stretching	3469.0,3475.8,3585.7,3590.4
OPO bending (in plane)	437.8
HPH torsional(vertical)	795.2
HPH torsional(horizontal)	920.1
PO stretching	1023.3,1218.2
HPH bending(out of plane)	1112.4
HPH bending(in plane)	1176.2
PH stretching	2236.3,2176.6

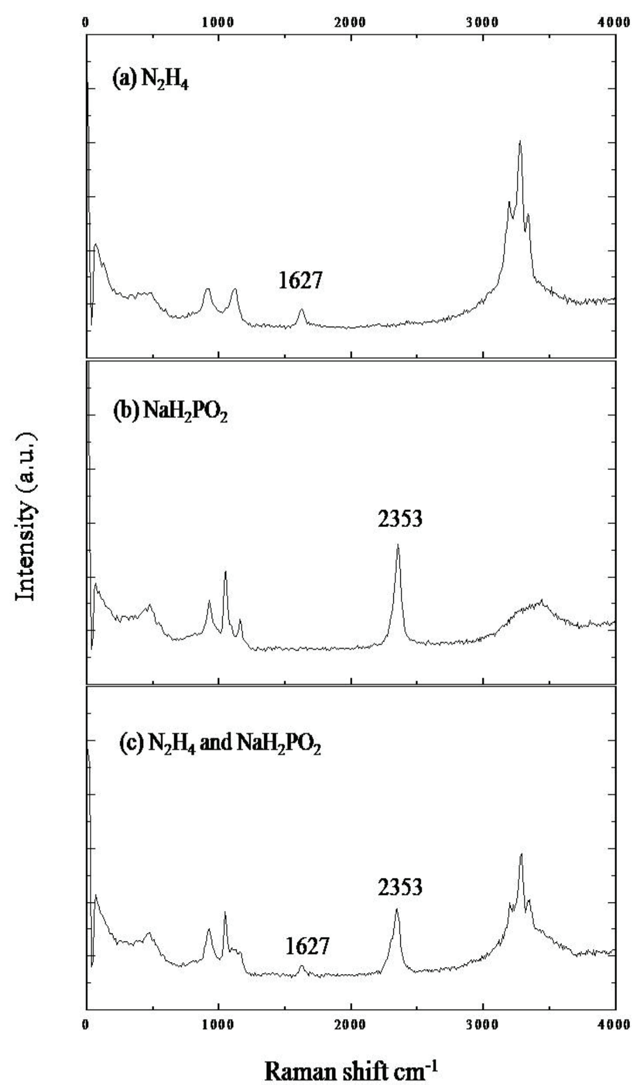

Fig. 3.3.1 Raman spectra of hydrazine and hypophosphite ions.

3.3.2 Analysis of hydrazine on a Cu surface with nano-scale resolution by SERS and DFT

As a next step, author analyzed the characterization of hydrazine on a Cu surface by Raman spectroscopy and DFT calculation. Table 3.3.2 and Figure 3.3.2 show the theoretical Raman spectrum calculated by using DFT and experimental Raman spectra of the solution on the Cu antenna. A Raman spectrum of hydrazine on the Cu antenna was given as Fig. 3.3.2. Because of the device which is coupled with a piezo stage as described in the last chapter, the top-line and bottom line were defined as Raman scattering of hydrazine solution and Cu antenna, and the intermediate lines could be considered as Raman scattering of hydrazine on Cu antenna in Fig. 3.3.2. Meanwhile, Cu-N stretching mode on 341.1 cm^{-1} in Table 3.3.2 was also given by DFT calculation. This wavenumber domain is near to that of experimental result of Raman spectroscopy. Thus, the Raman shift at 385 cm^{-1} was defined as Cu-N bond in Fig. 3.3.2. Moreover, there were other lines at 488, 545, 590, 661, 775, 1084, 1208 and 1279 cm^{-1} of undetermined scattered radiation which author had assigned tentatively to the NH_2 rocking, NN stretching, NH_2 wagging, and NH_2 twisting, respectively. These corresponded to the calculation of hydrazine adsorption on Cu as shown in Table 3.3.2.

One of the major different points between the actual conditions of experimental bath and the theoretical models in this study was the solvent effect on the electronic structure of adsorption state, which should be one of the most important points to provide the different values between the experimental measurement and the calculation. Even though author used PCM model to involve solvent effect in the theoretical model, it seemed not sufficient to reproduce fully accurate spectrum shown in the experimental measurement. This was because although our Raman spectrum showed the influences from the solvent as molecules to interact with adsorbent especially in our highly localized Raman spectrum measurement, PCM method modeled such solvent just as a field around the chemicals. It was therefore important to model more accurate solvent models at this solid-liquid interface in order to obtain values corresponding precisely to experimental data, which would be one of our next targets. However, PCM method was sufficient to obtain qualitative understanding of Raman spectrum and the adsorption model of hydrazine in electroless deposition was revealed from these results.

From these results, the adsorption model of hydrazine in electroless deposition was revealed. Furthermore, these peaks were only observed at 1-2 nm from the antenna surface which meant that this method absolutely could to define the bonding and structure of adsorbed hydrazine just only on the Cu antenna. Then, author applied DFT

calculation to model the structure of adsorbed hydrazine on Cu.

Table 3.3.2 The theoretical Raman spectrum calculation of hydrazine on Cu by using DFT.

Vibrational mode	**Wavenumber (cm^{-1})**
Cu-N stretching	341.1
NH_2 rocking	580.8
NN stretching	919.8
NH_2 wagging	1091.2,1150.3
NH_2 twisting	1302.8,1375.1
NH_2 scissor	1666.6,1676.5

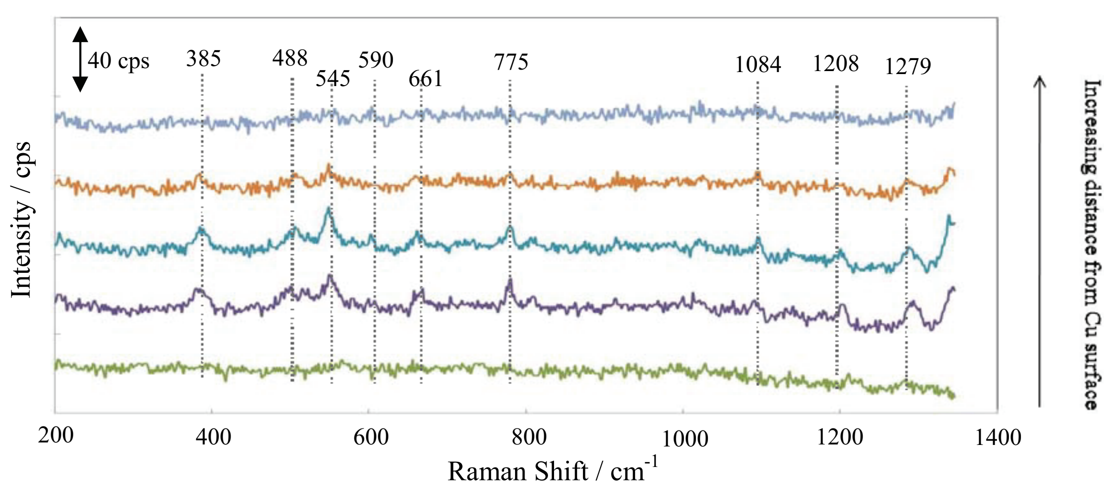

Fig. 3.3.2 Raman spectrum of hydrazine on the Cu antenna (1 nm/step).

In order to elucidate the structure of hydrazine on the Cu surface, DFT was applied to model the adsorption of hydrazine on a Cu surface. The conditions of DFT calculation are described above. Figure 3.3.3 shows the prospective configuration of hydrazine on fcc-Cu (111) calculated by DFT calculation. In the Fig. 3.3.3, the surface model was the tetrahedral cluster model made up of 20 Cu atoms [22]. Moreover, all parameters of adsorbing system are optimized, including the cluster structure and molecular structure.

Consequently, the most stable conformation of adsorbed hydrazine was given as gauche-conformation by DFT calculation; and hydrazine was adsorbed on the Cu surface via the N atom, as shown in Figure 3.3.3. Therefore, the experimental vibrational modes could be identified by using DFT calculation; and the boding and structure of hydrazine adsorption on the Cu surface were demonstrated by experimental and theoretical perspectives.

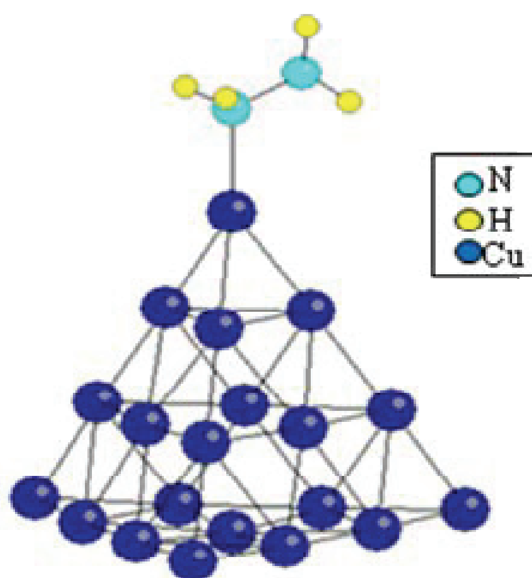

Fig. 3.3.3 The prospective configuration of hydrazine on Cu (gauche-conformation).

To achieve more precise measurements and obtain more information of electroless deposition, a piezoelectric motor was used to change the focal depth of measurements by 0.5 nm step instead of 1 nm step, as described above. Figure 3.3.4 shows the Raman spectra of hydrazine on the Cu antenna with varying height from the antenna with 0.5 nm/ step. The Cu-N stretching mode at 385 cm^{-1} was defined as shown above. There was no such Raman shift in the spectrum of the reductants solution alone. Thus, the Raman shift at 380 cm^{-1} could also be defined as Cu-N bonding in Fig. 3.3.4. Moreover, there were other lines at 619, 928, 1119/1151, 1281/1344 and 1578/1642 cm^{-1} of undetermined scattered radiation which were assigned to the NH_2 rocking, NN stretching, NH_2 wagging, NH_2 twisting, and NH_2 scissor, respectively, by comparing them with the Raman and DFT results of hydrazine adsorption on Cu, as shown above.

Furthermore, these peaks were only observed at 0.5 nm from the antenna surface which meant that this method could define the bonding of adsorbed hydrazine more precisely than 1 nm from the antenna surface. Then, author applied the 0.5 nm measurement to analyze the characterization of adsorbed hypophosphite ions on the Cu antenna.

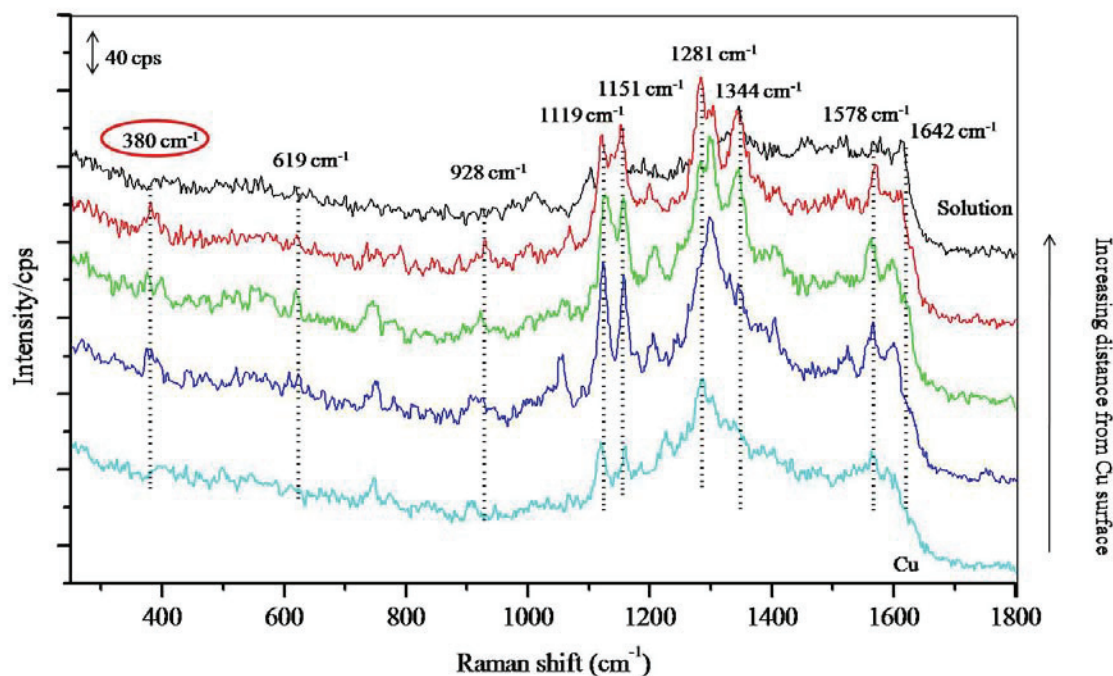

Fig. 3.3.4 Raman spectra of hydrazine on the Cu antenna (0.5 nm/step).

3.3.3 Analysis of hypophosphite ions on a Cu surface with nano-scale resolution by SERS and DFT

Next, to clarify the reaction mechanism of reductants oxidation and the interaction between reductants, author also analyzed the characterization of hypophosphite ions on a Cu surface by Raman spectroscopy and DFT calculation. Figure 3.3.5 shows the experimental Raman spectra of hypophosphite ions on the Cu antenna with varying height from the antenna (0.5 nm/step). However, only the characteristic peaks of hypophosphite ions (in contact with plasmon antenna) were given in Fig. 3.3.5. There were lines at 1037, 1193, 1291 and 1524 cm^{-1} of undetermined scattered radiation which were assigned to the PO stretching and HPH bending (out of plane and in plane) by comparing them with the results of DFT calculation and Raman spectra of only reductants.

It has previously been proved that copper does not have catalytic activity for the oxidation of hypophosphite by experimental identification [10]. M. Kunimoto et al. have also demonstrated [11] that an energy barrier exists in the dehydrogenation step which is one of the elementary steps of hypophosphite oxidation by theoretical identification. Then, author applied SERS and DFT to analyze the characterization of adsorbed hydrazine and hypophosphite ions on the Cu surface.

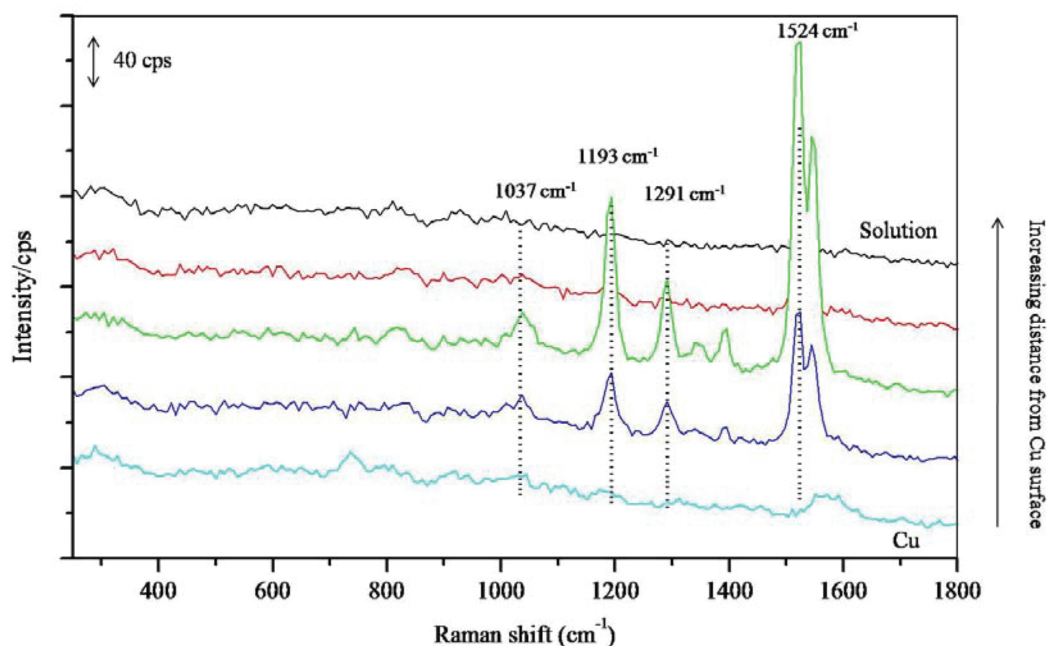

Fig. 3.3.5 Raman spectra of hypophosphite ions on the Cu antenna.

3.3.4 Analysis of hydrazine and hypophosphite ions on a Cu surface with nano-scale resolution by SERS and DFT

In order to demonstrate the interaction mechanism between reductants, author focused on the interaction between hydrazine and hypophosphite ions on a Cu surface using Raman spectroscopy and DFT. Figure 3.3.6 shows the experimental Raman spectra of mixture (hydrazine and hypophosphite ions) on the Cu antenna with varying height from the antenna (0.5 nm/step). By comparing with the Raman spectra of reductants solution with no Cu antenna, an extra Raman shift at 395 cm^{-1} is observed in Fig. 3.3.6. Because this Raman peak was only observed after the mixture was placed on the Cu surface, author defined the Raman shift at 385 cm^{-1} as Cu-N bonding, as shown above, and copper did not have catalytic action for the oxidation of hypophosphite. Author could also define the Raman shift at 395 cm^{-1} as Cu-N bonding. Additional lines at 660, 1124, 1264, 1368 and 1514 cm^{-1} of undetermined scattered radiation were assigned to the NH_2 rocking, NN stretching, NH_2 wagging, NH_2 twisting, and NH_2 scissor, respectively. However, these Raman shifts do not correspond precisely to the Raman spectra of hydrazine and the results which are shown above. Author suggests that there is interaction between hydrazine and hypophosphite ions that lead to this shift. The mechanism responsible for this shift has not been clearly established, however. Hence, the DFT calculation was used to clarify the interaction between hydrazine and hypophosphite ions on the Cu surface.

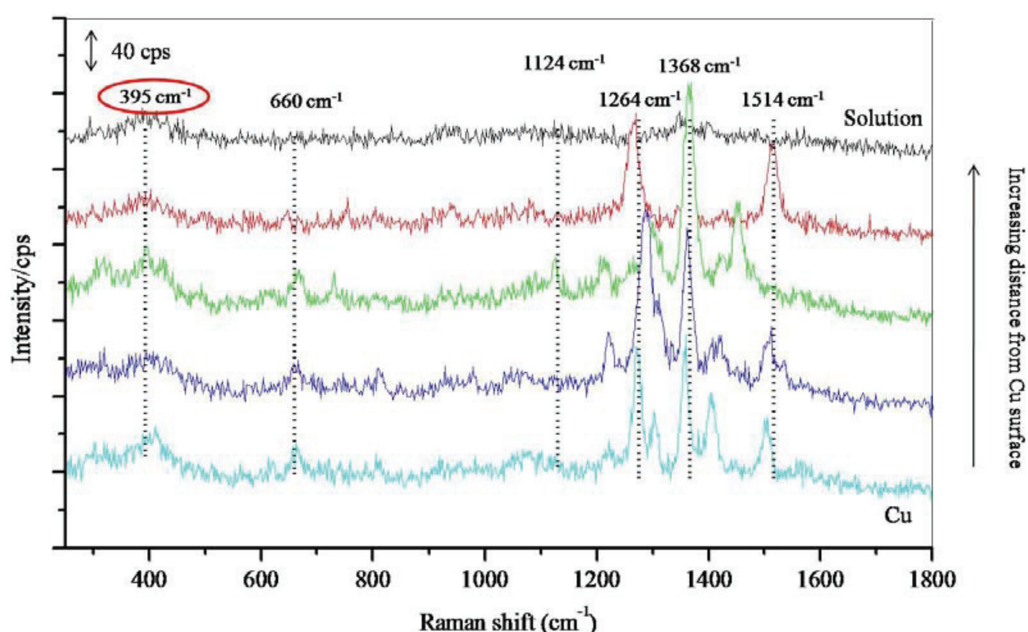

Fig. 3.3.6 Raman spectra of mixture (hydrazine and hypophosphite ions) on Cu antenna.

As a next step, DFT calculation was applied to elucidate the interaction mechanism between hydrazine and hypophosphite ions on a Cu surface. Figure 3.3.7 shows the conformation of adsorbed mixture on Cu by DFT calculation. In Fig. 3.3.7, the surface model was the tetrahedral cluster model made up of 20 Cu atoms, as described above [22]. All parameters of adsorbing system are optimized, including the cluster structure and molecular structure. Fig. 3.3.7 indicates that hydrazine exhibits electrostatic interaction with hypophosphite ions on the surface. There were two evidences supporting this interaction obtained. First, the charge values of hydrogen atoms (H1 and H2) of hydrazine became slightly positive when hypophosphite ion had its two oxygen atoms interact with H1 and H2 on the Cu surface: Mulliken charge of H1 changed from 0.3237 to 0.3891; and the charge of H2 changed from 0.3138 to 0.3637. These changes are likely to be the result of polarization of two molecules so that they have much strong electrostatic interaction; it suggests that the changes in charge values of H1 and H2 should be the first evidence of the interaction between the two reductants. The other evidence is the structural change of hydrazine when hypophosphite ion approaches it. In the conformation (Fig. 3.3.7), a significant difference in the dihedral angle of H1-N-N-H2 between hydrazine and hydrazine with hypophosphite ion, from 31.56^{o} to 16.03^{o}, is observed; it is likely to be the major aspect of the structural change of hydrazine. For the effective interaction between hydrazine and hypophosphite ion, two hydrogen atoms of hydrazine, H1 and H2, and two oxygen atoms of hypophosphite ion should be put on the same plane. In order to form this geometry, dihedral angle of H1-N-N-H2 will be decreased. Thus, the decrease in the dihedral angle H1-N-N-H2 is another evidence of interaction between hydrazine and hypophosphite ion. Furthermore, these charge and structure changes of hydrazine caused by the interaction with hypophosphite ion could explain why the peaks in the Raman spectra of the mixture do not correspond precisely to the Raman spectra of hydrazine alone, and may explain the ultra-thin films with high perpendicular magnetic coercivities in the study of Ouchi et al. [7].

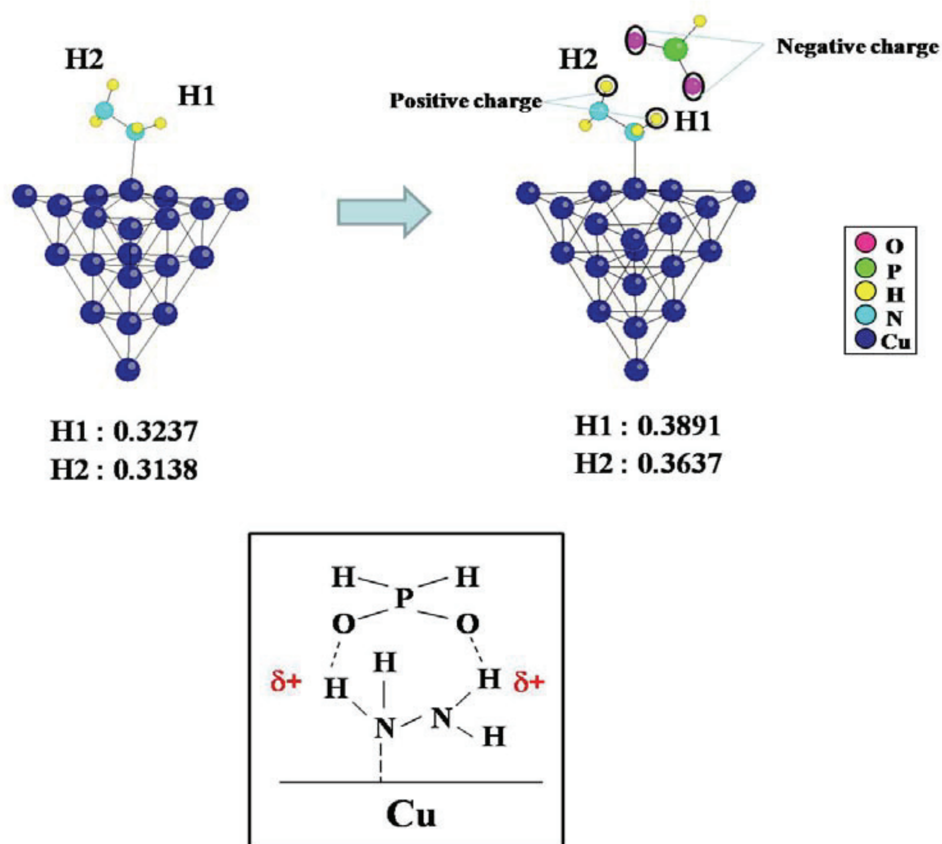

Fig. 3.3.7 The conformation of adsorbed mixture (hydrazine and hypophosphite ion) on Cu given by DFT calculation.

3.4 Conclusions

Characterization of hydrazine and hypophosphite ions on a Cu surface to elucidate the reaction mechanism of reductants on Cu for electroless deposition was performed by SERS and DFT calculation. Experimental results showed that Raman peaks of hydrazine and hypophosphite ions adsorbed on Cu were provided. DFT results were in good agreement with the Raman spectra results.

Moreover, the conformations of adsorbed hydrazine and mixture (hydrazine and hypophosphite ion) on the Cu surface were given by DFT calculation.

From the experimental and calculated results, author demonstrated the interaction mechanism of adsorbed hydrazine and hypophosphite ions on the Cu surface; and such a molecular level characterization approach with experimental and theoretical analysis is beneficial for studying solid-liquid interface in the electroless deposition process.

In the later chapter, such characterization method will also be applied to well understand the acceleration and suppression effect of thiourea on the oxidation reaction of hypophosphite ions on Ni surface.

References

[1] L. M. Abrantes, and J. P. Correia, *J. Electrochem. Soc.*, 141, 2356 (1994).
[2] B. Popov, *Plat. Surf. Finish.*, 91, 40 (2004).
[3] R. Johnstone, A. Wilby, and I. Endtwistle, *Chem. Rev.*, 85, 129 (1995).
[4] T. Curtius, *J. Prakt. Chem.*, 39, 107 (1889).
[5] T. Adams, and R. Brown, *Org. Synth.; Coll.*, 1, 309 (1941).
[6] J. E. A. M. van den Meerakker, *J. Appl. Electrochem.*, 11, 395 (1981).
[7] T. Ouchi, N. Shimano, and T. Homma, *Electrochim. Acta,* 56, 9575 (2011).
[8] T. Yokoshima, Y. Yamaji, K. Kikuchi, H. Nakagawa, and M. Aoyagi, *J. Electrochem. Soc.*, 157, D65 (2010).
[9] T. Ouchi, Y. Arikawa, T. Kuno, and T. Homma, *Electrochem. Soc. Trans.*, 25 (2010) 125.
[10] I. Ohno, O. Wakabayashi, and S. Haruyama, *J. Electrochem. Soc.*, 132, 2323 (1985).
[11] M. Kunimoto, T. Shimada, S. Odagiril, H. Nakai, and T. Homma, *J. Electrochem. Soc.*, 158, D585 (2011).
[12] T. Shimada, A. Tamaki, H. Nakai, and T. Homma, *Electrochemistry*, 75, 45 (2007).
[13] M. Kunimoto, H. Nakai, and T. Homma, *J. Electrochem. Soc.*, 158, D626 (2011).
[14] M. Yanagisawa, M. Shimamoto, T. Naknishi, M. Saito, and T. Osaka, *Electrochem. Soc. Trans.*, 16, 397 (2008).
[15] M. J. Frisch, G. W. Trucks, H. B. Schlegel, G. E. Scuseria, M. A. Robb, J. R. Cheeseman, J. A. Montgomery, Jr., T. Vreven, K. N. Kudin, J. C. Burant, J. M. Millam, S. S. Iyengar, J. Tomasi, V. Barone, B. Mennucci, M. Cossi, G. Scalmani, N. Rega, G. A. Petersson, H. Nakatsuji, M. Hada, M. Ehara, K. Toyota, R. Fukuda, J. Hasegawa, M. Ishida, T. Nakajima, Y. Honda, O. Kitao, H. Nakai, M. Klene, X. Li, J. E. Knox, H. P. Hratchian, J. B. Cross, V. Bakken, C. Adamo, J. Jaramillo, R. Gomperts, R. E. Stratmann, O. Yazyev, A. J. Austin, R. Cammi, C. Pomelli, J. W. Ochterski, P. Y. Ayala, K. Morokuma, G. A. Voth, P. Salvador, J. J. Dannenberg, V. G. Zakrzewski, S. Dapprich, A. D. Daniels, M. C. Strain, O. Farkas, D. K. Malick, A. D. Rabuck, K. Raghavachari, J. B. Foresman, J. V. Ortiz, Q. Cui, A. G. Baboul, S. Clifford, J. Cioslowski, B. B. Stefanov, G. Liu, A. Liashenko, P. Piskorz, I. Komaromi, R. L. Martin, D. J. Fox, T. Keith, M. A. Al-Laham, C. Y. Peng, A. Nanayakkara, M. Challacombe, P. M. W. Gill, B. Johnson, W. Chen, M. W. Wong, C. Gonzalez, and J. A. Pople, Gaussian 03, Revision C.02, Gaussian, Inc., Wallingford, CT, (2004).

[16] A. D. Becke, *J. Chem. Phys.*, 98, 5648 (1993).
[17] C. Lee, W. Yang, and R. G. Parr, *Phys. Rev. B*, 37, 785 (1988).
[18] D. E. Woon, and T. H. Dunning Jr., *J. Chem. Phys.*, 98, 1358 (1993).
[19] T. Clark, J. Chandrasekhar, G. W. Spitznagel, and P. v. R. Schleyer, *J. Comput. Chem.*, 4, 294 (1983).
[20] P. J. Hay, and W. R. Wadt, *J. Chem. Phys.*, 82, 299 (1985).
[21] J. B. Foresman, T. A. Keith, K. B. Winberg, J. M. Sniinian, and J. Frisch, *J. Phys. Chem.*, 100, 16098 (1996).
[22] L. Zhao, L. Jensen, and G. C. Schatz, *J. Am. Chem. Soc.*, 128, 2911 (2006).

Chapter 4:

Analysis of acceleration and suppression effect of thiourea on the reaction of hypophosphite ions on Ni surface using Raman spectroscopy and DFT

4.1 Introduction

From the previous chapters, it was indicated that the secret of reductants reaction on metal surfaces can be analyzed by experimental approaches and theoretical approaches. Therefore, it is necessary to understand the reductants reaction in detail to elucidate the mechanism of the electroless deposition.

This chapter attempts to clarify the reaction mechanism of the electroless deposition process using experimental and theoretical methodologies focusing on the acceleration and suppression effects of the additive on the oxidation reaction of reductant on the Ni surface.

Thiourea is one of the most widely used additives for controlling the rate of electroless Ni deposition [1-3], which enables the fabrication of well structured and well controlled metal films with complex behaviors[4-6]. For example, while thiourea works as an accelerating factor in the electroless Ni deposition in an acidic bath, it works as a suppressing factor in electroless Ni deposition in an alkaline bath [7-9]. Furthermore, Kunimoto et al. have demonstrated [10] that the acceleration effect of thiourea is mainly on the anodic reaction of the hypophosphite ions and the adsorption step is thought to be the most important effect, as described in the chapter 1. However, the acceleration and suppression mechanisms for the complicated behavior of thiourea in acidic/alkaline electroless plating bath has not been fully understood.

In order to elucidate such mechanisms, the experimental method is applicable for characterizing thiourea and hypophosphite ions adsorption on Ni surface with high-selectivity component at right angle down to sub-monolayer level using surface enhanced Raman spectroscopy technique using so called plasmon antenna [11], which can define the place and structure of detected molecules just only at 1-2 nm from the antenna surface [12,13]. Meanwhile, the theoretical method can provide molecular level, basic level information for understanding the mechanisms according to the chemical characteristics [14-17]. In this chapter, therefore, a mechanism for the acceleration and suppression effect of thiourea on electroless Ni deposition has been proposed by a careful analysis of Raman and DFT calculation.

4.2 Methodology

The present investigation is based on the surface enhanced plasmon antenna designed by FDTD calculation to enhance the Raman scattering through the laser perpendicular to the surface, whose details are described elsewhere [11]. A step by step measurement in changing the distance from the antenna within 1 nm was applied, which meant that this method could define the location and structure of the adsorbed molecules that were only 1-2 nm from the antenna surface. The structure, electric field, and three-dimensional simulated area of the antenna are shown in the chapters 2 and 3.

The fabrication process of Ni plasmon antenna is shown below. First, the concentric pattern of the plasmon antenna was formed on a glass substrate using electron beam (EB) lithography and UV-nanoimprint lithography (Kyodo-International). Then, a 5-nm-thick Ti layer was deposited on the concentric pattern, followed by deposition of a 100-nm-thick Ni layer; the two layers were formed by EB evaporation (EBX-6D, ULVAC, Inc.). The SEM image of the plasmon antenna (Ni) was shown in Figure 4.2.1.

A 0.5-μL aliquot of thiourea (H_2NCSNH_2, Kanto Chemical Co., Inc.), hypophosphite ($NaPH_2O_2 \cdot H_2O$, Kanto Chemical Co., Inc.), or a mixture of both, as summarized in Table 4.2.1, was placed on the antenna surface. The solutions with antenna were then measured using a Raman microspectroscopy device (Nanofinder 30, Tokyo Instruments, Inc.) equipped with a confocal microscope. The 632.8 nm line from a He-Ne laser was used for the excitation of Raman scattering. The laser beam was focused onto a spot (~1 μm in diameter) through an objective lens at a magnification of 100× N.A. (0.9). The data acquisition time was 1.0 s per measurement. The wavenumber resolution was 2.4 cm^{-1} when a 600 grooves/mm grating was used. The laser power irradiated onto the sample surface was 3 mW. Ammonium sulfate (100 mM; $(NH_4)_2SO_4$, Kanto Chemical Co., Inc.) was applied to decrease the pH value, while ammonia (NH_3, Kanto Chemical Co., Inc.) was used to increase it.

For the theoretical analysis, DFT calculations were performed using the B3LYP functional, which is a combination of Becke's three-parameter hybrid exchange functional (B3) [18] and the Lee-Yang-Parr correlation functional (LYP) [19], as implemented in the Gaussian 09 package [20]. The 6-31 ++G** basis set was assigned to all atoms [21]. The solvation effect was taken into account via a polarizable continuum model (PCM) [22], which used a dielectric constant of 78.39.

To clarify the acceleration and suppression effects of thiourea on the oxidation of

hypophosphite ions, the amounts of deposits on a Cu substrate were measured as follows: First, 2.0 × 2.0 cm^2 Cu substrates were consecutively rinsed with ethanol, phosphate for 60 s, sulfate for 60 s, and water. Second, they were activated in an activation bath for 5 min at 40 °C; the activation bath was composed of 0.1 M of DMAB, 100 ppm $NiSO_4$, 600 ppm citric acid, and 0.1 M of boric acid to maintain a pH value of 9.0. Last, they were put in an electroless deposition bath for 20 min at 70 °C. The electroless deposition bath was composed of 0.2 M of NaH_2PO_2, 0.1 M of $NiSO_4$, 0.15 M of citric acid, and 0.3 M of $(NH_4)_2SO_4$. The schematic illustration of process steps for measurement of the amounts of deposits on a Cu substrate was shown in Figure 4.2.2.

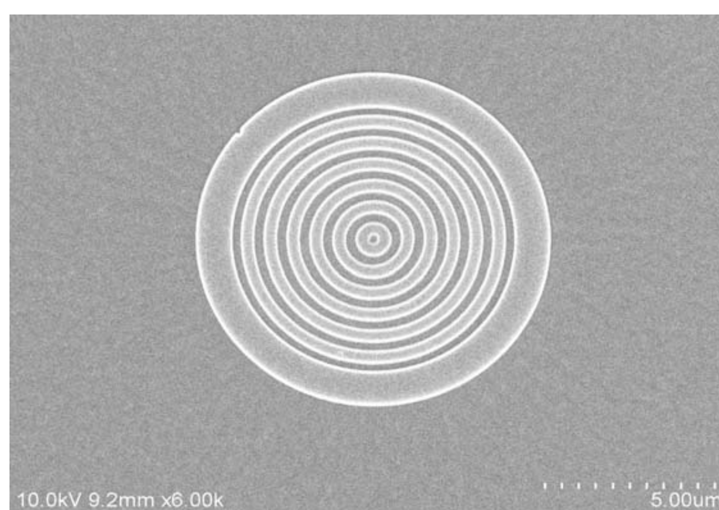

Fig. 4.2.1 SEM image of Ni plasmon antenna.

Table 4.2.1 Experimental conditions of the solutions.

Chemicals	**Concentration (mM)**		
	(a)	**(b)**	**(c)**
$NaH_2PO_2 \cdot H_2O$	300	-	300
Thiourea (ppm)	-	0.5	0.5

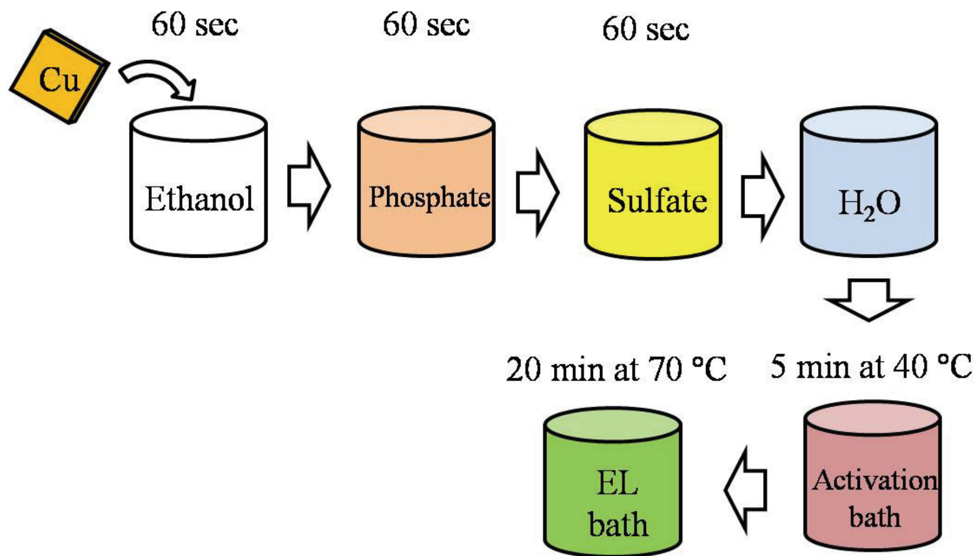

Fig. 4.2.2 The schematic illustration of process steps for measurement of the amounts of deposits on a Cu substrate.

4.3 Results and Discussion

4.3.1 Raman and DFT of thiourea and hypophosphite ions

In this study, detailed mechanisms of the interaction between reductants and the oxidation reaction of reductants on metal surfaces were analyzed by a careful analysis of Raman spectroscopy and DFT calculation as described above. In order to go inside the mechanism of the electroless deposition, however, it is necessary to understand the acceleration and suppression effects of the additive on the oxidation reaction of reductant in the electroless deposition process. To achieve this purpose, author analyzed the characterization of thiourea and hypophosphite ions by Raman spectroscopy above all. Figure 4.3.1 displays the Raman spectra of the "bulk" solutions (not in contact with plasmon antenna); for comparison, Table 4.3.1 lists the corresponding DFT calculated Raman shifts. Accordingly to the theoretical Raman spectra of thiourea and hypophosphite ions (Table 4.3.1), all characteristic peaks of the solutions were observed as follows:

1. The Raman spectra of H_2NCSNH_2, shown in Fig. 4.3.1 (a), features three pronounced polarized lines at 486, 736, and 1085 cm^{-1}, which were assigned to NCN bending, CS stretching, and CNH bending, respectively, by comparing them with the theoretical Raman spectrum of thiourea.

2. The Raman spectra of NaH_2PO_2, shown in Fig. 4.3.1 (b), has five pronounced polarized lines at 475, 928, 1054, 1157, and 2353 cm^{-1}, which were assigned to OPO bending, HPH torsion, PO stretching, HPH bending, and PH stretching, respectively, by comparing them with the theoretical Raman spectrum of hypophosphite ions.

3. The Raman spectra of a mixture of 300 mM NaH_2PO_2 and 0.5 ppm H_2NCSNH_2 is shown in Fig. 4.3.1 (c); characteristic CS stretching and PH stretching bands are evident at ~736 and ~2353 cm^{-1}, respectively, for both components with no overlap. The two bands in the spectra of the mixture are observed completely, which means that the spectra of the mixture contains all the pronounced characteristic bands of H_2NCSNH_2 and NaH_2PO_2.

The characteristic peaks of the Raman spectra of the solutions could be applied as fundamental information to define the bonding of adsorbed thiourea and hypophosphite ions on Ni; in addition, the differences between the Raman spectra of the solutions in contact with and those not in contact with Ni plasmon antenna could be elucidated.

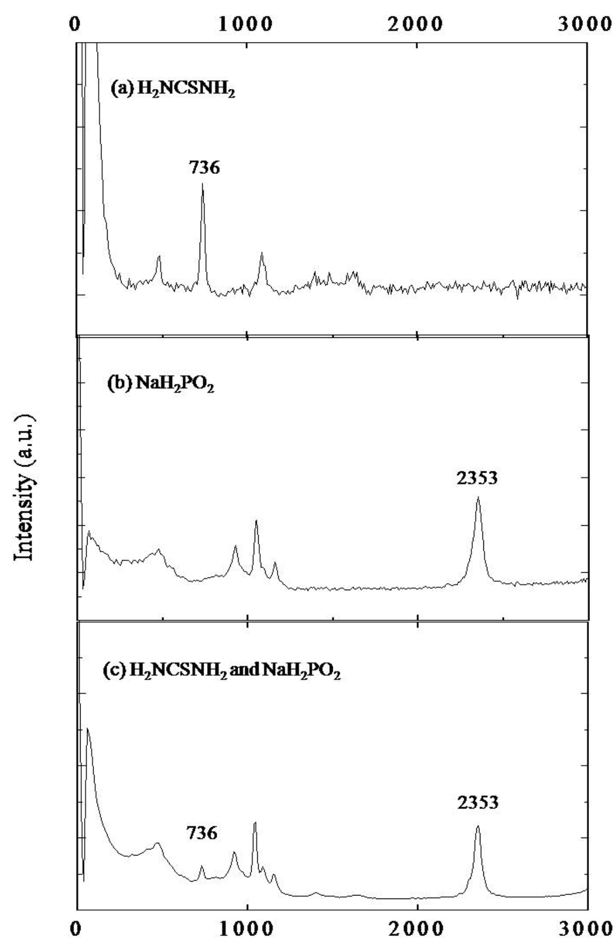

Fig. 4.3.1 Raman spectra of the solutions (not in contact with plasmon antenna).

Table 4.3.1 DFT calculation results for thiourea and hypophosphite ions.

Vibrational mode	Wavenumber (cm^{-1})
NCN bending	462.9
CS stretching	730.7
CNH bending	1075.3
OPO bending	430.2
HPH torsional	780.3, 912.4
PO stretching	1010.4, 1153.3
HPH bending	1166.7
PH stretching	2236.3,2176.6

4.3.2 Analysis of thiourea and hypophosphite ions on a Ni surface with nano-scale resolution by Raman and DFT

In order to elucidate the characterization of thiourea and hypophosphite ions adsorption on a Ni surface, the Raman spectroscopy and DFT calculation were applied. First of all, the behavior of thiourea adsorption on a Ni surface using Raman spectroscopy is shown below. Figure 4.3.2 shows the Raman spectra of a pH 6.4 solution of thiourea, which is the original pH value for thiourea, on the Ni antenna at varying heights from the antenna. Because of the device which is coupled with a piezo stage, the top-line and bottom line were defined as Raman scattering of thiourea solution and Ni antenna, and the intermediate lines could be considered as Raman scattering of thiourea on Ni antenna in Fig. 4.3.2. A Raman shift was observed at 385 cm^{-1}; this signal was not present in the spectrum of thiourea alone. Kunimoto et al. [10] had revealed that thiourea was adsorbed on the Ni surface via the S atom with a declined structure, as determined by theoretical calculations. Thus, the Raman shift at 385 cm^{-1} is likely due to Ni-S bonding with a declined thiourea structure. Moreover, other lines at 474, 736, and 1085 cm^{-1} of undetermined polarization were evident and were assigned to NCN bending, CS stretching, and CNH bending, respectively, by comparing them with the DFT calculated spectrum of thiourea.

Then, author attempted to analyze the characterization of the reductant (hypophosphite ion) adsorption on the Ni surface by Raman spectroscopy.

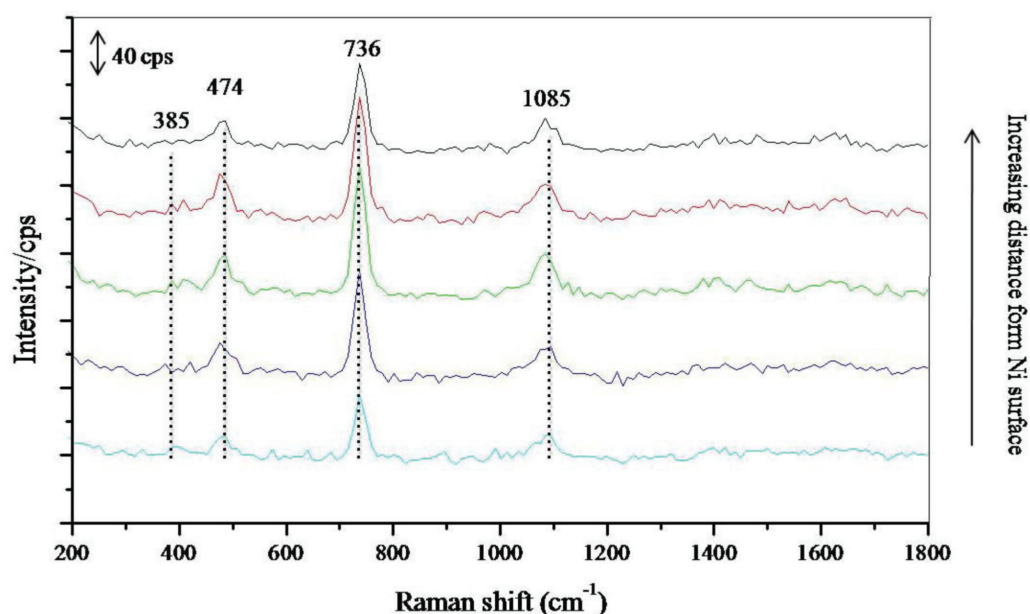

Fig. 4.3.2 Raman spectra of thiourea on a Ni surface (pH 6.4).

As a next step, the characterization of hypophosphite ions adsorption on a Ni surface was also analyzed by Raman spectroscopy. The behavior of adsorbed hypophosphite ions on a Ni surface is shown below. Figure 4.3.3 shows the experimental Raman spectra of a pH 6.4 solution of hypophosphite ions, which is the original pH value for hypophosphite ions, on the Ni antenna at varying heights from the antenna. Only the characteristic peaks of hypophosphite ions (in contact with the antenna) are shown in Fig. 4.3.3; no extra Raman shifts were observed because hypophosphite ions adsorbed onto the Ni surface via an H atom, as determined in the results of Kunimoto et al [10]. The lines at 507, 935, 1086, and 1179 cm^{-1} with undetermined polarization were assigned to OPO bending, HPH torsion, PO stretching, and HPH bending, respectively, by comparing them with the DFT calculated spectrum of hypophosphite ions. However, these peaks do not correspond precisely to the Raman spectra of hypophosphite ions. For example, only one PO stretching, one HPH bending and one HPH torsion peaks were observed. One possible explanation for the difference is that hypophosphite ions may adsorb on Ni surface via three atoms (two H atoms and one O atom). Therefore, the vibration movement of hypophosphite ions should be strongly restricted in the system, and some chemical bonds were not observed in the Raman spectra.

Then, author attempted to characterize a mixture of thiourea and hypophosphite ions on a Ni surface by Raman spectroscopy and DFT calculation.

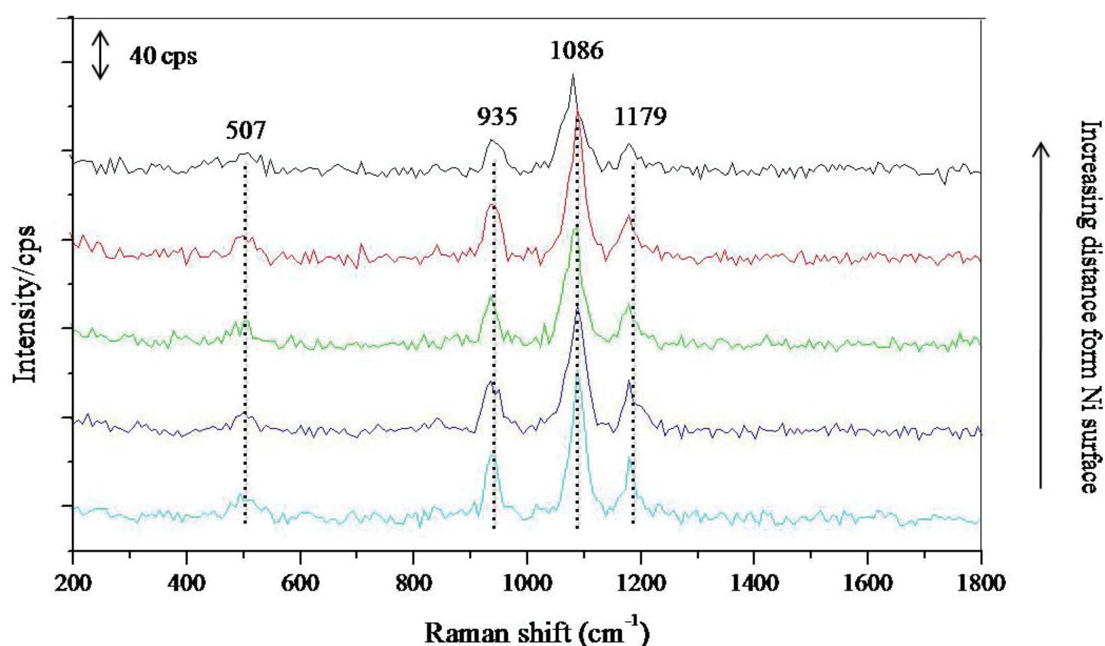

Fig. 4.3.3 Raman spectra of hypophosphite ions on a Ni surface (pH 6.4).

To demonstrate the effects of thiourea on the oxidation reaction of hypophosphite ions on the Ni surface, the characterization of a mixture of thiourea and hypophosphite ions on Ni was analyzed by Raman spectroscopy and DFT calculation. Figure 4.3.4 shows the experimental Raman spectra of a pH 6.4 solution of a mixture of thiourea and hypophosphite ions, which is the original pH value of the mixture, on the Ni antenna at varying heights from the antenna. Raman shifts at 367 cm^{-1} were observed in these spectra that were not present in the Raman spectra of thiourea and hypophosphite ions that were not in contact with the plasmon antenna. Because this Raman peak at 367 cm^{-1} was observed only after the mixture was placed on the Ni surface, it is likely due to Ni-S bonding, as seen in the Raman spectra of thiourea on Ni; there was no such Raman shift in the Raman spectrum of hypophosphite ions. Additional lines at 499, 758, 935, 1079, and 1179 cm^{-1} of undetermined polarization were assigned to OPO bending or NCN bending, CS stretching, HPH torsion, PO stretching or CNH bending, and HPH bending, respectively. The characteristic Raman peaks of both thiourea and hypophosphite ions were observed in the spectra in Fig. 4.3.4, which means that these two co-adsorb on the Ni surface. The comparison of the Raman spectra of thiourea and hypophosphite ions that were not in contact with the Ni plasmon antenna showed that no shift in the Raman peaks due to chemical interactions between thiourea and hypophosphite ions adsorbed on the Ni surface was evident. Therefore, the interaction between thiourea and hypophosphite ions is electrostatic molecular interaction. Moreover, the chemical characteristics of the S atom is expected to induce electronic vacancies on the metal surface to improve the stability of the adsorbed hypophosphite ions, as shown in the study of Kunimoto et al. (see Figure 4.3.5) [10].

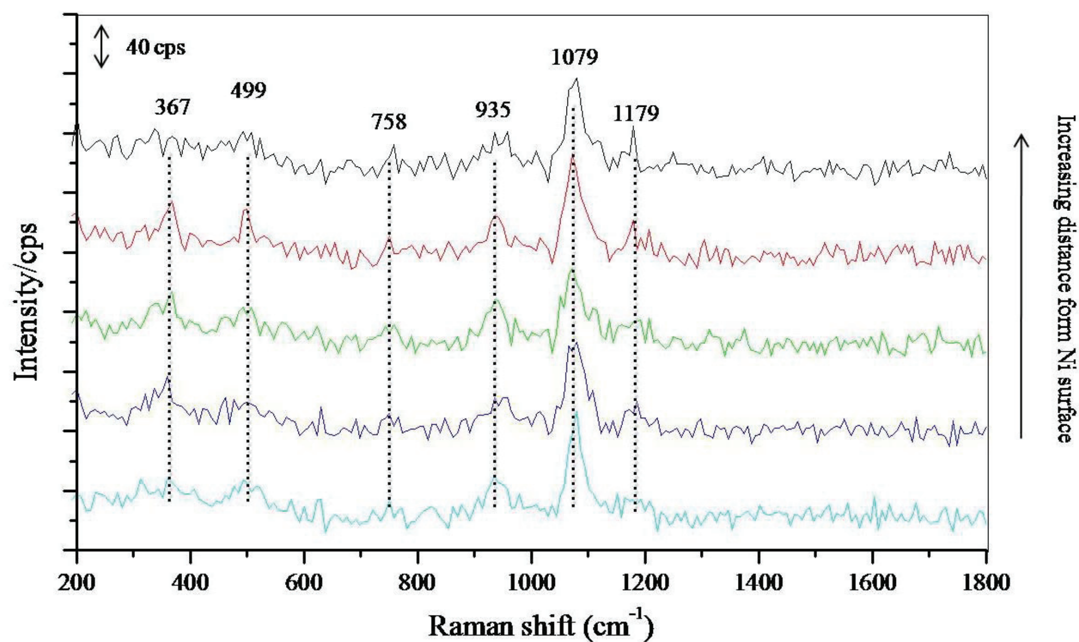

Fig. 4.3.4 Raman spectra of a mixture of thiourea and hypophosphite ions on a Ni surface (pH 6.4).

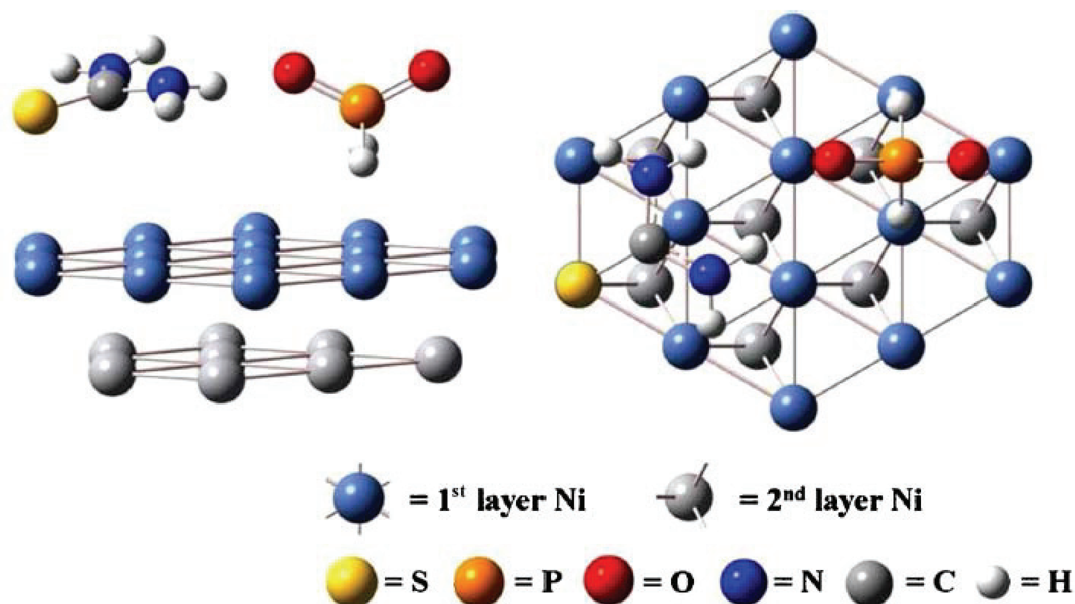

Fig. 4.3.5 Co-adsorption model consisting of thiourea, hypophosphite ion, and the Ni surface [10].

4.3.3 Analysis of the pH effect on thiourea and hypophosphite ions on a Ni surface by Raman and DFT

To elucidate the complicated effects of thiourea on hypophosphite ions in acidic/alkaline electroless Ni deposition baths, thiourea and hypophosphite ions adsorption on the Ni surface in acidic/alkaline baths was characterized.

Figures 4.3.6 (a), (b), and (c) show the experimental Raman spectra of pH 6 solutions of thiourea, hypophosphite ions, and a mixture of thiourea and hypophosphite ions on a Ni surface, respectively, in which the pH values are adjusted with $(NH_4)_2SO_4$, and Figure 4.3.6 (d) shows the experimental Raman spectrum of $(NH_4)_2SO_4$ on a Ni surface. These Raman spectra were of the adsorbed molecules at only 1-2 nm from the antenna surface; the spectra were selected from the Raman spectra of the pH 6 solutions of thiourea, hypophosphite ions, a mixture of thiourea and hypophosphite ions, and the original solution of $(NH_4)_2SO_4$ on a Ni surface at varying heights from the antenna. Note that there is no change in the Raman peaks with pH variation from 6 to 5.5.

Only three pronounced peaks at 477, 645, and 993 cm^{-1} in Fig. 4.3.6 (a); 484, 645, and 1015 cm^{-1} in Fig. 4.3.6 (b); 469, 637, and 986 cm^{-1} in Fig. 4.3.6 (c); and 469, 630, and 993 cm^{-1} in Fig. 4.3.6 (d) were observed. These peaks were assigned to OSO(OH) bending, S(OH) stretching, and SO stretching, respectively, by comparing them with the DFT calculated spectrum of HSO_4^-, as shown in Table 4.3.2. These results suggest that HSO_4^- ions mainly exist when $(NH_4)_2SO_4$ adsorbs on the Ni surface because of the equilibrium described by the equation below, and that the HSO_4^- ions are much closer to the Ni surface than the thiourea and hypophosphite ions.

$$(NH_4)_2SO_4 \rightleftarrows 2NH_4^+ + SO_4^{2-} \quad (1)$$

$$SO_4^{2-} + H^+ \rightleftarrows HSO_4^- \quad (2)$$

In other words, the HSO_4^- ions inhibit the co-adsorption of thiourea and hypophosphite ions. This effect increases the length of the induction period of the deposition process because it delays double-layer charging, intermediate formation, or diffusion-layer formation, which slows the rate of deposition.

To confirm this, the amounts of deposits on the substrate (Cu) were measured, as shown in Table 4.3.3. Comparison with the deposition weight results at high pH, the deposition weight at pH 6 is much lower because of the slow rate of deposition (Table 4.3.3). Therefore, although the induction period was not directly observed in our Raman

results because there was no Ni^{2+} in the bath, it is evident from our experimental results that this will be useful for understanding the long period of electroless plating in some cases. In summary, thiourea provides an accelerating effect by promoting the adsorption of hypophosphite ions in an acidic bath, as shown in Table 4.3.3; however, it cannot overcome the inhibiting effect of HSO_4^- to regenerate the high deposition rate seen with much higher pH values, as shown in Table 4.3.3. Therefore, this study proposes that HSO_4^- is chemically inert, but has a geometric influence on the electroless deposition process.

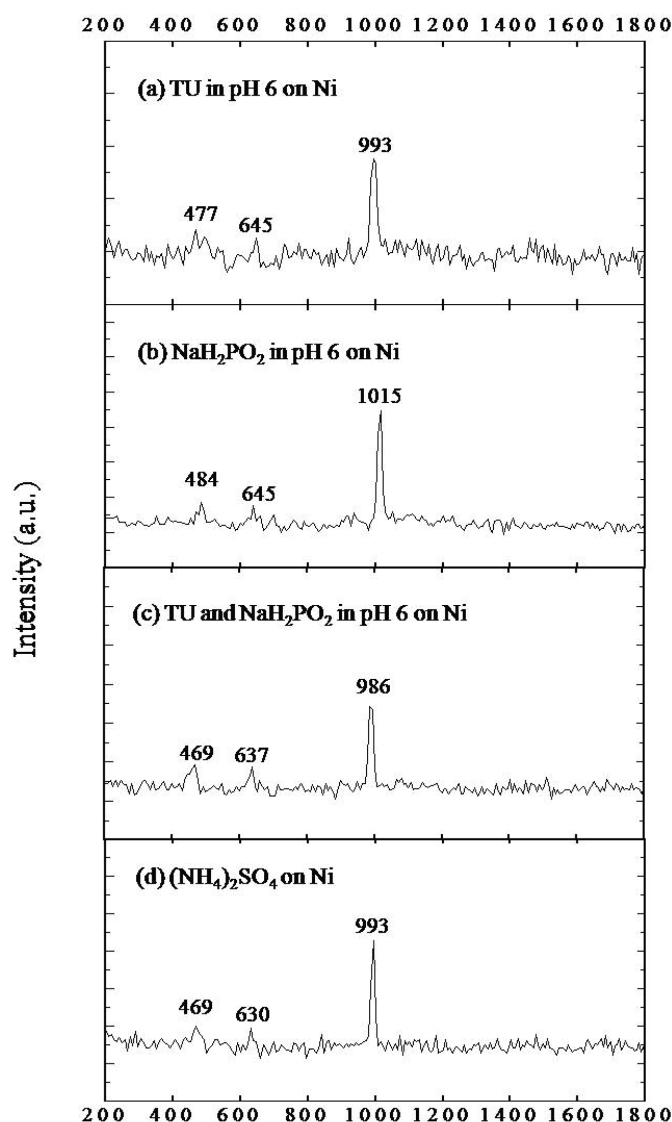

Fig. 4.3.6 Raman spectra of pH 6 solutions of (a) thiourea (TU); (b) hypophosphite ions; (c) a mixture of thiourea and hypophosphite ions on a Ni surface; and (d) $(NH_4)_2SO_4$ on a Ni surface.

Table 4.3.2 DFT calculation results for HSO_4^- ions.

Vibrational mode	**Wavenumber (cm^{-1})**
OSO(OH) bending	508.1, 525.1, 527.7
S(OH) stretching	609.4
SO stretching	988.2

Table 4.3.3 Amount of deposits on substrate (Cu). (TU, thiourea.)

pH	**Deposition weight (mg)**	
	without TU	**with TU**
6	4.25	6.43
7	5.57	6.61
8	10.59	9.76

Figures 4.3.7 (a), (b), and (c) show the experimental Raman spectra of pH 7 solutions of thiourea, hypophosphite ions, and a mixture of thiourea and hypophosphite ions on a Ni surface, respectively; the pH values were adjusted with ammonia solution (NH_3). These Raman spectra were of the adsorbed molecules at only 1-2 nm from the antenna surface and were selected from the corresponding Raman spectra at varying heights from the antenna. Note that there is no change in the Raman peaks throughout the pH adjustment from 7 to 10.

All characteristic Raman peaks of the co-adsorption system of thiourea and hypophosphite ions on a Ni surface were observed in Fig. 4.3.7. No shift in the peaks was observed between these spectra and those of pH 6.4 solutions of thiourea, hypophosphite ions, and a mixture of thiourea and hypophosphite ions on a Ni surface. However, as shown in Table 4.3.3, the deposited amounts on the substrate at pH 8 decreased from 10.59 mg without thiourea to 9.76 mg with thiourea, which shows the suppressing effect of thiourea. This is completely contrary to the phenomenon at pH 6, the deposited amounts increased from 4.25 mg without thiourea to 6.43 mg with thiourea, which indicates the accelerating effect of thiourea. Because HSO_4^- ions were not added to the high-pH bath, and therefore did not adsorb on the Ni surface, they did not inhibit the adsorption of thiourea and hypophosphite ions, so the deposition rate was very fast because of the little induction period. In addition, OH^- ions can also promote the reaction of hypophosphite ions in high-pH electroless deposition processes. However, the adsorption of thiourea can poison the Ni surface because of high coverage of the Ni surface with thiourea in high-pH baths; this coverage could impair the adsorption of OH^- ions, which usually attack the hypophosphite ions on the metal surface to promote the hypophosphite reaction. Because the accelerating effect of thiourea is not expected to be as strong as that of OH^-, the suppression of OH^- adsorption by thiourea results in a slower deposition rate. This is evident in the suppressed rate after the addition of thiourea at high pH, as shown in Table 4.3.3.

As a result, this study explains both the acceleration and suppression mechanisms of thiourea in terms of its fundamental characteristics.

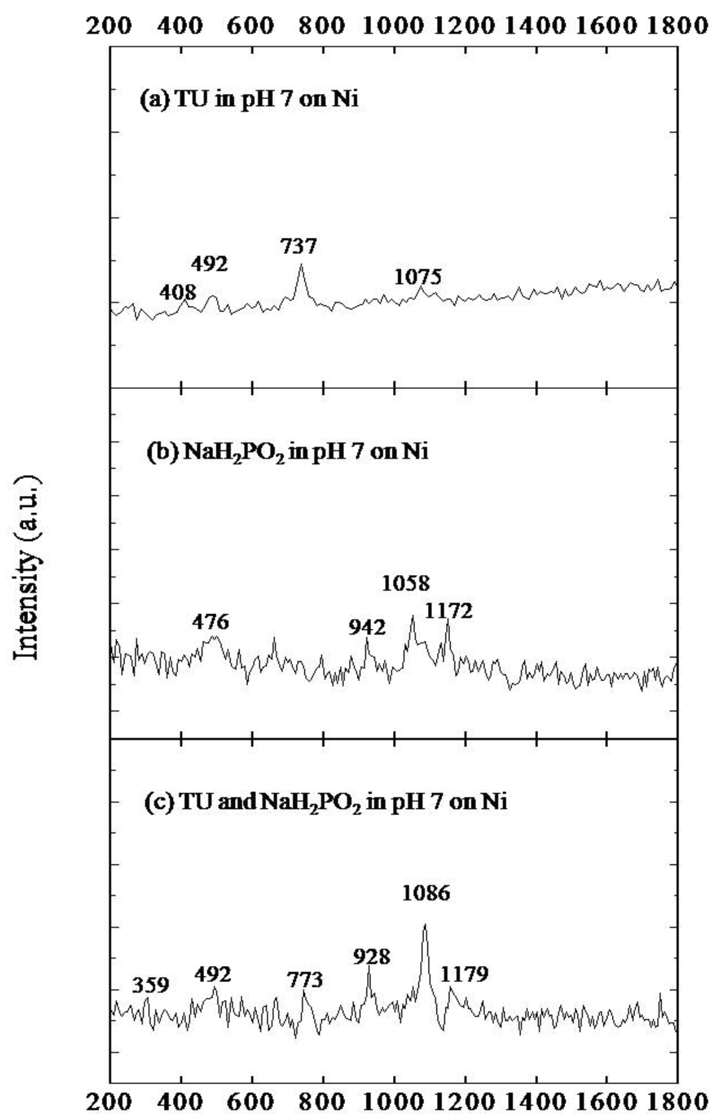

Fig. 4.3.7 Raman spectra of pH 7 solutions of (a) thiourea (TU); (b) hypophosphite ions; (c) a mixture of thiourea and hypophosphite ions on a Ni surface.

4.4 Conclusions

In order to elucidate the acceleration and suppression mechanisms of thiourea on the oxidation reaction of hypophosphite ions on a Ni surface for electroless deposition, both experimental measurements and theoretical calculations were performed.

The elementary steps of thiourea and hypophosphite ions in acidic/alkaline electroless Ni deposition baths were elucidated; characterization was performed by Raman spectroscopy and DFT calculations. By using Raman spectroscopy and comparing the resultant spectra with the DFT calculated results, the co-adsorption of thiourea and hypophosphite ions on the Ni surface was confirmed. Moreover, the complicated behavior of thiourea in acidic/alkaline baths was investigated by characterizing the thiourea and hypophosphite ions on a Ni surface in acidic/alkaline baths using Raman spectroscopy and DFT.

From the Raman and DFT results, a mechanism for the acceleration and suppression effects of thiourea on the oxidation of hypophosphite ions in electroless Ni deposition is proposed; these results are beneficial for understanding and establishing novel and highly controlled electroless plating processes and can be used for various industrial applications. Moreover, Ni surface also shows good SERS enhancement by comparing with the SERS effect of Ag.

In our future work, thiourea and hypophosphite ions on various metal surfaces and at various pH values will be characterized from both experimental and theoretical perspectives.

References

[1] J. S. Sallo, J. Kivel, and F. C. Albers, *J. Electrochem. Soc.*, 110, 890 (1963).
[2] J. Kivel, and J. S. Sallo, *J. Electrochem. Soc.*, 112, 1201 (1965).
[3] K. L. Lin, and J. W. Hwang, *Mater. Chem. Phys.*, 76, 204 (2002).
[4] F. J. Nuzzi, *Plating and Surface Finishing*, Jan, 51 (1983).
[5] M. Paunovic, and R. Arndt, *J. Electrochem. Soc.*, 130, 794 (1983).
[6] J. Li, and P. A. Kohl, *J. Electrochem. Soc.*, 149, C631 (2002).
[7] F. Hanna, Z. A. Hamid, and A. A. Aal, *Mater. Lett.*, 58, 104 (2003).
[8] C. H. de Minjer, and A. Brenner, *Plating*, 44, 1297 (1957).
[9] S. E. Beacom, and B. J. Riley, *Nucleonics*, 18, 82 (1960).
[10] M. Kunimoto, K. Endo, H. Nakai, and T. Homma, *Electrochim. Acta*, 100, 311 (2013).
[11] M. Yanagisawa, M. Shimamoto, T. Nakanishi, M. Saito, and T. Osaka, *Electrochem. Soc. Trans.*, 16, 397 (2008).
[12] A. Campion, and P. Kambhampati, *Chem. Soc. Rev.*, 27, 241 (1998).
[13] M. Moskovits, *J. Raman Spectrosc.*, 36, 485 (2005).
[14] L. Öhrström, *C. R. Chim.*, 8, 1374 (2005).
[15] T. Homma, H. Nakai, M. Onishi, and T. Osaka, *J. Phys. Chem. B*, 103, 1774 (1999).
[16] T. Homma, I. Komatsu, A. Tamaki, H. Nakai, and T. Osaka, *Electrochim. Acta*, 47, 47 (2001).
[17] M. Kunimoto, H. Nakai, and T. Homma, *J. Electrochem. Soc.*, 158, D626 (2011).
[18] A. D. Becke, *J. Chem. Phys.*, 98, 5648 (1993).
[19] C. Lee, W. Yang, and R. G. Parr, *Phys. Rev. B*, 37, 785 (1988).
[20] M. J. Frisch, G. W. Trucks, H. B. Schlegel, G. E. Scuseria, M. A. Robb, J. R. Cheeseman, G. Scalmani, V. Barone, B. Mennucci, G. A. Petersson, H. Nakatsuji, M. Caricato, X. Li, H. P. Hratchian, A. F. Izmaylov, J. Bloino, G. Zheng, J. L. Sonnenberg, M. Hada, M. Ehara, K. Toyota, R. Fukuda, J. Hasegawa, M. Ishida, T. Nakajima, Y. Honda, O. Kitao, H. Nakai, T. Vreven, J. A. Montgomery, Jr., J. E. Peralta, F. Ogliaro, M. Bearpark, J. J. Heyd, E. Brothers, K. N. Kudin, V. N. Staroverov, R. Kobayashi, J. Normand, K. Raghavachari, A. Rendell, J. C. Burant, S. S. Iyengar, J. Tomasi, M. Cossi, N. Rega, J. M. Millam, M. Klene, J. E. Knox, J. B. Cross, V. Bakken, C. Adamo, J. Jaramillo, R. Gomperts, R. E. Stratmann, O. Yazyev, A. J. Austin, R. Cammi, C. Pomelli, J. W. Ochterski, R. L. Martin, K. Morokuma, V. G. Zakrzewski, G. A. Voth, P.

Salvador, J. J. Dannenberg, S. Dapprich, A. D. Daniels, Ö. Farkas, J. B. Foresman, J. V. Ortiz, J. Cioslowski, and D. J. Fox, Gaussian, Inc., Wallingford, CT (2009).
[21] W. J. Hehre, L. Random, P. V. R. Schleyer, and J. A. Pople, *Ab Initio Molecular Orbital Theory*, p.1-548, John Willey & Sons, New York (1986).
[22] E. Cances, B. Mennucci, and J. Tomasi, *J. Chem. Phy.*, 107, 3032 (1997).

Chapter 5:
General Conclusions

To establish finer electroless deposition systems, the reaction mechanism of the process is necessary to be elucidated. The objective of this study is to propose the systematic reaction mechanism of the reductants on metal surfaces in electroless deposition.

In order to achieve this objective, the reaction behaviors of reductants on metal surfaces were analyzed in detail, using experimental and theoretical procedures. The experimental methodology is applicable for characterizing reductants adsorption on metal surfaces with high-selectivity component at right angle down to sub-monolayer level using a surface enhanced Raman antenna, which can define the place and structure of adsorbed reductants just only at 1-2 nm from the antenna surface. The theoretical methodology can provide molecular level, basic level information for understanding the mechanism according to the chemical characteristics.

As reductants, hypophosphite ion, hydrazine, and formaldehyde were studied, for they have common characteristics to the other reductants and have been widely applied in electroless deposition. Thus, the reaction mechanisms of these reductants are strongly needed to be understood from the molecular level viewpoint, based on their own chemical characteristics.

As a primary factor, which determines the reaction behaviors of the reductants, the characterization of reductants adsorption on metal surfaces was focused to be analyzed.

To elucidate the characterization, Raman peaks of adsorbed reductants on Ag and Cu were provided by using the surface enhanced Raman antenna and comparison with DFT results. Furthermore, the most stable configurations of adsorbed reductants on the Cu surface were given by DFT calculation. From these experimental and calculated results, author also demonstrated the interaction mechanism of adsorbed hydrazine and hypophosphite ions on the Cu surface.

As important environmental factors, which secondarily influence the reaction behaviors of reductants, the effects of the additive were focused to be analyzed.

To elucidate the acceleration and suppression mechanisms of thiourea, as a sulfur containing additive, on electroless Ni deposition process, the characterization of thiourea and hypophosphite ions on a Ni surface in acidic/alkaline baths was analyzed.

From the discussion described in Chapters 2, the characterization of reductants

adsorption on metal surfaces using surface enhanced Raman antenna is analyzed as follows:

By using the plasmon antenna and comparison with DFT results, Raman peaks of adsorbed reductants on Ag and Cu were provided, which can be defined as Ag/Cu-reductants bonding. Furthermore, the characteristic peaks in the Raman spectra were in good agreement with DFT results. From the experimental and calculated results, author demonstrated that this method had a possibility to define the structure of adsorbed reductants just only on the plasmon antenna. Moreover, the di-σ-bonded conformation of adsorbed formaldehyde on the Cu surface was given by DFT calculation as the most stable configuration. These adsorption behaviors of reductants on metal surfaces have important influence on the reaction of reductants in electroless deposition.

From the discussion described in Chapter 3, the interaction mechanism of reductants on a Cu surface is elucidated as follows.

Experimental results showed that Raman peaks of hydrazine and hypophosphite ions adsorbed on a Cu surface were provided. From these results and comparison with DFT results, author demonstrated the interaction mechanism of adsorbed hydrazine and hypophosphite ions on the Cu surface. The hydrogen atoms (H1 and H2) of hydrazine were positively charged when hypophosphite ion had its two oxygen atoms interact hydrazine with H1 and H2 on the Cu surface. Meanwhile, the oxygen atoms of hypophosphite ion were negatively charged when the interaction happened. Therefore, it is expected that the hydrogen atoms of hydrazine interact with the oxygen atoms of hypophosphite ion. Further the conformation of the interaction between hydrazine and hypophosphite ion on Cu predicted by DFT.

From the discussion described in Chapter 4, the acceleration and suppression mechanisms of thiourea on the oxidation reaction of hypophosphite ions on a Ni surface are elucidated as follows.

The elementary steps of thiourea and hypophosphite ions in acidic/alkaline electroless Ni deposition baths were elucidated; characterization was performed by Raman spectroscopy and DFT calculations. In the acidic baths, the HSO_4^- ions inhibit the co-adsorption of thiourea and hypophosphite ions and increase the length of the

induction period of the deposition process. Therefore, this study proposes that although thiourea provides an accelerating effect by promoting the adsorption of hypophosphite ions in an acidic bath, it cannot overcome the inhibiting effect of HSO_4^-; and HSO_4^- is chemically inert but has a geometric influence on the electroless deposition process.

In the alkaline baths, the adsorption of thiourea can poison the Ni surface because of high coverage of the Ni surface with thiourea in high-pH baths; this coverage could impair the adsorption of OH^- ions, which usually attack the hypophosphite ions on the metal surface to promote the hypophosphite reaction. Because the accelerating effect of thiourea is not expected to be as strong as that of OH^-, the suppression of OH^- adsorption by thiourea results in a slower deposition rate.

Although each mechanism shown above is just one of the factors determining the reactivity of the process, such viewpoints must provide further insights for establishing new electroless plating processes.

List of Achievements

List of Achievements

1. Original Articles

"Analysis of hydrazine on a Cu surface with nanoscale resolution using surface enhanced Raman spectroscopy"
Bin Jiang, Takanari Ouchi, Naofumi Shimano, Akira Otomo, Masahiro Kunimoto, Masahiro Yanagisawa, Takayuki Homma.
Electrochim. Acta., 100, 317 (2013).

"Raman and DFT study of the reaction of hydrazine and hypophosphite on a Cu surface in the electroless deposition process"
Bin Jiang, Siggi Wodarz, Masahiro Kunimoto, Masahiro Yanagisawa, Takayuki Homma.
Electrochemistry., 81, 1 (2013).

"Effect of thiourea on oxidation of hypophophsphite ions on Ni surface investigated by Raman spectroscopy and DFT calculation"
Bin Jiang, Masahiro Kunimoto, Masahiro Yanagisawa, Takayuki Homma.
J. Electrochem. Soc., 160, D366 (2013).

2. International Conferences

"Observation of Reductants on Copper surface in Electroless Deposition Process with Nano-scale Resolution using Surface Enhanced Raman Spectroscopy"
Bin Jiang, Naofumi Shimano, Takanari Ouchi, Masahiro Yanagisawa, Takayuki Homma.
International symposiums on Renewable Energy & Materials Tailoring at Kyoto university, Kyoto, Japan, 18-19 Sept. (2011).

"Raman and DFT study of Reductant Adsorption on Metal Surfaces in Electroless Deposition Process"
Bin Jiang, Masahiro Kunimoto, Masahiro Yanagisawa, Takayuki Homma.
The PRiME 2012 joint international (222nd) meeting of the Electrochemical Societies, Hawaii Convention Center and the Hilton Hawaiian Village, Honolulu, Hawaii, USA. 7-12 Oct., (2012).

Acknowledgement

Acknowledgement

The present dissertation is the collection of the studies, which have been carried out under the direction of Professor Dr. Takayuki Homma (Department of Applied Chemistry in Waseda University, Japan). I am deeply grateful to Professor Dr. Takayuki Homma for his kindly supervision, invaluable advices, helpful discussion, careful reviewing of the manuscript, and continuous encouragement on my works during the term of September 2010-September 2013. I have learned not only scientific knowledge and techniques but also many attitudes and spirits as a researcher from him. I would like to express my deep appreciation to Professor Dr. Tetsuya Osaka (Department of Applied Chemistry in Waseda University, Japan) for his intellectual advices and continuous encouragement on my research. I wish to express my heartfelt thanks to Professor Dr. Masahiro Yanagisawa (Nanotechnology Research Center in Waseda University, Japan) for his kindly supports and technical advices on my Raman research projects. I deeply appreciate to Professor Dr. Kazuyuki Kuroda (Department of Applied Chemistry in Waseda University, Japan), Professor Dr. Yoshiyuki Sugahara (Department of Applied Chemistry in Waseda University, Japan), and Associate Professor Dr. Toshiyuki Momma (Department of Applied Chemistry in Waseda University, Japan) for reviewing my thesis, and for their valuable suggestions and advices.

I also wish to express my appreciation to Professor Dr. Yasuhiro Fukunaka (Waseda University), Professor Dr. Yosi Shacham-Diamand (Tel Aviv University), Professor Dr. Giovanni Zangari (University of Virginia), Professor Dr. Firedrich Prinz (Stanford University), and Dr. Mikiko Saito (Waseda University) for their excellent discussions and insightful comments. I have learned the many things about research from them.

I express the special thanks to my senior colleagues in Ph.D course, Dr. Takanari Ouchi, Dr. Masahiro Kunimoto, Dr. Chiaki Kobayashi for their constructive comments and discussions through the experiments. I also would like to sincerely thank my colleagues in my research group, Mr. Naofumi Shimano, Mr. Akira Otomo, Mr. Siggi Wodarz, Mr. Kenji Seki, and thank my colleagues, Mr. Cheng-ping Lin, Mr. Tomoyuki Yamamoto. Gratitude is offered to all my colleagues in the laboratory for their experimental assistant, discussions, and kind friendship. Many of you have made me feel at home and sometimes work hard.

I am grateful to staffs of the laboratory and Nanotechnology Research Center, Waseda University for their support for my research.

Finally, I express greatest thanks to my parents, Konghai Jiang and Xiuqin Yin, for deep affection, continuous encouraging, financial and mental supports for completing this thesis.

October 2013

Bin Jiang